*Journal of Engineering Science* *Vol. XXVIII, no. 1 (2021), pp. 23 - 30*
*Fascicle* *Industrial Engineering* *ISSN 2587-3474*
*Topic* *Materials Science and New Technologies* *eISSN 2587-3482*

**https://doi.org/10.52326/jes.utm.2021.28(1).01**
**UDC 621.357.8:546.824-31**

# $TiO_2$ NANOTUBES FOR PHOTOCATALYTIC DEGRADATION OF METHYLENE BLUE

Vladimir Ciobanu*, ORCID ID: 0000-0002-4588-2866,
Irina Plesco, ORCID ID: 0000-0001-9878-2757

*National Center for Materials Study and Testing, Technical University of Moldova, 168, Stefan cel Mare av., Chisinau, Moldova*
*Corresponding author: Vladimir Ciobanu, *vladimir.ciobanu@cnstm.utm.md*

Received: 12. 08. 2020
Accepted: 02. 18. 2021

**Abstract.** Titanium dioxide remains one of the most studied semiconductor for photocatalytic applications due to its low cost production, reduced toxicity, ability to break down the organic pollutants and possibility to achieve complete mineralization. In this work, we report on results of the photocatalytic activity of titanium dioxide nanotubes fabricated by electrochemical anodization technique in an electrolyte solution containing a mixture of hydrofluoric acid, ethylene glycol and phosphoric acid. The morphology and crystallinity of the obtained nanotubes were investigated by means of electron microscopy and it was found that nanotubes have a constant outer diameter of 200 nm and an internal conical shape where the diameter gradually decreases from 120 nm at the wide end to 50 nm at the narrow end. The transmission electron microscopy investigation defined two different phases of titanium dioxide obtained after annealing of amorphous $TiO_2$ in air at 650 °C and 850 °C. Photocatalytic activity of the samples have been evaluated in methylene blue solution in the presence of dispersed nanotubes under visible and UV irradiation by means of UV/Vis spectroscopy. Anatase phase $TiO_2$ shows the best performance degrading 85 % of dye in 25 min under UV illumination, while rutile phase with anatase inclusions shows the best results with a 50 % decay of dye concentration in 25 min under visible light illumination.

**Keywords:** *Methylene Blue degradation, electrochemical anodization, photocatalysis, $TiO_2$ nanotubes, $TiO_2$ plasma etching.*

## Introduction

Among the metal oxide semiconductors, titanium dioxide (titania, $TiO_2$) nanomaterials have attracted much attention in the last decades. $TiO_2$ is considered a semiconductor with high potential applications due to its advantageous optical and electronic properties, structural and chemical stability, non-toxicity and photocatalytic activity. These properties make titania an excellent material for solar energy conversion [1], applications in dye functionalized solar cells [2, 3], biomedicine [4, 5], microengines [6] and in other fields [7, 8]. Comparing with other forms of $TiO_2$, unidimensional nanostructures like nanotubes are the most suitable structures for solar energy conversion and

photocatalysis due to inherent high scattering of light and related optical absorption and high surface to volume ratio. Different techniques were applied by researchers to increase the material performances like doping, combination with other materials or inducing structural changes. For instance, doping with non-metal elements has demonstrated a decrease of material bandgap and its possibility for optical applications in the visible range. The anodic oxidation technique is one of the most effective way to fabricate titania nanotubes due to its simplicity, self-ordering and low cost process [9]. This technique has the disadvantage because one end of nanotubes at interface with the Ti foil is closed. Therefore, the nanotube membranes have limitation for some applications and an additional opening process is necessary.

Water pollution has become a serious concern nowadays. Pollution can cause many diseases to human body such as cancers, tumors or skin irritation [10]. Different techniques for water purification were investigated in order to remove the dyes from wastewaters such as chemical precipitation [11], reverse osmosis [12], electrochemical oxidation [13], chemical coagulation-flocculation and bio-oxidation [14] as well as membrane filtration [15]. In recent years, the photocatalytic degradation of organic pollutants from residual waters has attracted much attention. Semiconducting oxide photocatalysts have an enormous potential for air and water treatment of organic contaminants. There are many studies on semiconducting materials for photocatalysis such as $TiO_2$ [16], ZnS [17], CdS [18], $Fe_2O_3$ [19], ZnO [20], GaN/ZnO compound [21]. Among these materials, $TiO_2$ is the most studied because of its ability to break down the organic pollutants and possibility to achieve complete mineralization. Due to its low-cost production, reduced toxicity, high reactivity and hydrophobicity, $TiO_2$ remains close to an ideal catalyst. In this work, we demonstrate the fabrication of titania nanotubes with both ends opened for photocatalytic degradation of Methylene Blue (MB) in water-based solution. The MB was selected as the dye for the experiments because it represents one of the most stable pollutant [22]. The anatase and anatase-rutile mixture phases of $TiO_2$ nanotubes were investigated.

## Methods

### Preparation of $TiO_2$ nanotubes

$TiO_2$ nanotubes were fabricated using electrochemical anodization of Ti foils purchased from Sigma-Aldrich with the thickness of 0.25 mm and purity >99,7%. Before anodization, the Ti foil was cleaned in acetone in an ultrasonic bath, rinsed with distilled water and dried under nitrogen flow. An electrolyte consisting of ethylene glycol (99.8%), hydrofluoric acid (48 wt%) and $H_3PO_3$ (85 wt%) was used. The anodization was realized in a two-electrode system with a Pt mesh as counter electrode. The electrolyte temperature was maintained at 25 °C during the anodization process. The applied voltage was increased gradually to 120 V, with a step of 1 V/sec and then kept constant for 1 h. After anodization, the samples were cleaned in acetone and DI water and then the formed oxide was mechanically separated from the Ti foil. The constituent nanotubes of membranes have the bottom ends closed because of the formation of a barrier oxide layer at the interface with the Ti foil. In order to open the bottom ends of the nanotubes, a Plasma Etching process was applied. The process took place in a PlasmaLab System 100-ICP Deep Reactive Ion Etching System in a mixture of Ar and $SF_6$ gases at ratio 5:1 for 5 min.

The obtained $TiO_2$ nanotubes were annealed at different temperatures in order to modify their crystallinity. The samples were treated at 650 °C and 850 °C in air in order to

obtain anatase and anatase - rutile phases, respectively. In order to separate individual nanotubes in the solution, the membrane consisting of nanotubes was sonicated for 30 sec.

**Photocatalytic Tests**

The organic contaminant solution was prepared by using 10 μM MB solution diluted in deionized water (DI). 20 mg of $TiO_2$ nanotubes of anatase and anatase - rutile mixture phases were added to 50 ml contaminant solution in a transparent glass beaker and kept under stirring conditions at 600 rpm using a magnetic stirrer. The mixture was irradiated from the top using a 100 W Blak Ray Hg lamp with the main intensity peak at 365 nm and a 150 W Halogen lamp with power density of 100 $mW \bullet cm^{-2}$ for investigation of MB degradation in UV and visible range, respectively. During the experiment, 3 ml solution was collected each 10 min and analyzed at UV/Vis spectrometer. The experiment on photocatalytic degradation continued until the solution becomes colorless, the minimum time being 80 min. The collected solution was centrifuged at 20,000 rpm for 15 min in order to sediment the micro/nanoparticles and then the liquid is transferred into a cuvette for UV/Vis spectroscopy. The absorption spectra were collected in the region 450 – 750 nm.

**Characterization Techniques**

The morphology and structural investigations of $TiO_2$ nanotubes were realized using electron microscopy (SEM Zeiss Gemini Ultra55 Plus, TEM JEOL JEM-2100). To monitor the degradation of MB, the optical absorption spectra were recorded with Perkin Elmer Lambda 750 UV/Vis spectrometer.

**Results and Discussions**

**Morphology study**

$TiO_2$ nanotubes have been fabricated by electrochemical anodization technique of Ti sheets. By using this method, it is possible to obtain huge amounts of nanotubes on a small surface of material. The images from the Figure 1 illustrates the top, cross section view and the bottom part of the $TiO_2$ nanotubes membrane detached from the Ti substrate before and after dry etching step.

The results of the morphology characterization of samples clearly demonstrate the tubular shape along both faces of the membrane, with a constant outer diameter of 200 nm and a variable inner diameter, which gradually decreases from 120 nm at the wide end to 50 nm at the narrow end. The length of the nanotubes can be easily tuned from tens of nm to hundreds of μm by adjusting the anodization conditions.

**TEM Structural Study**

It was reported previously that titania anatase-rutile phase transformation starts at approximately 600 °C [23,24]. Hence, to obtain anatase phase nanotubes the initial amorphous sample was treated at 650 °C, while treatment at temperature as high as 850 °C was applied to obtain anatase - rutile phase sample.

The results of TEM (Transmission Electron Microscopy) investigations presented in Figure 2 suggest that both $TiO_2$ nanotube samples, calcinated at 650 °C and 850 °C, are polycrystalline.

Polycrystalline electron diffraction (ED) patterns were analyzed by Rotational Average method which calculates a medium intensity of the electron reflection at certain distance from the ED central spot. To all the meaningful reflections were attributed corresponding crystal planes, referred as the *d*-values of the intensity peaks.

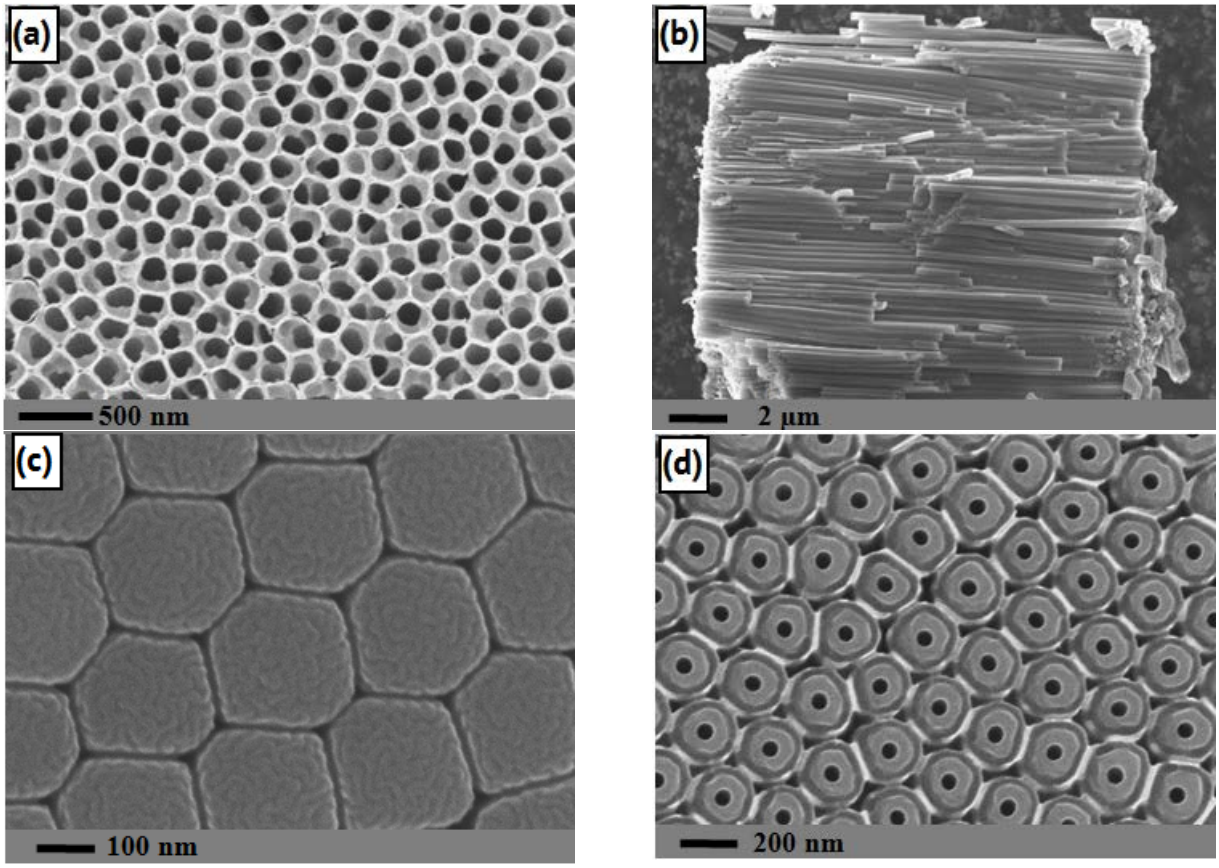


**Figure 1.** SEM images of $TiO_2$ membrane: (a) top part, (b) side view, (c) bottom part before dry etching step, (d) bottom part after dry etching showing opened nanotubes.

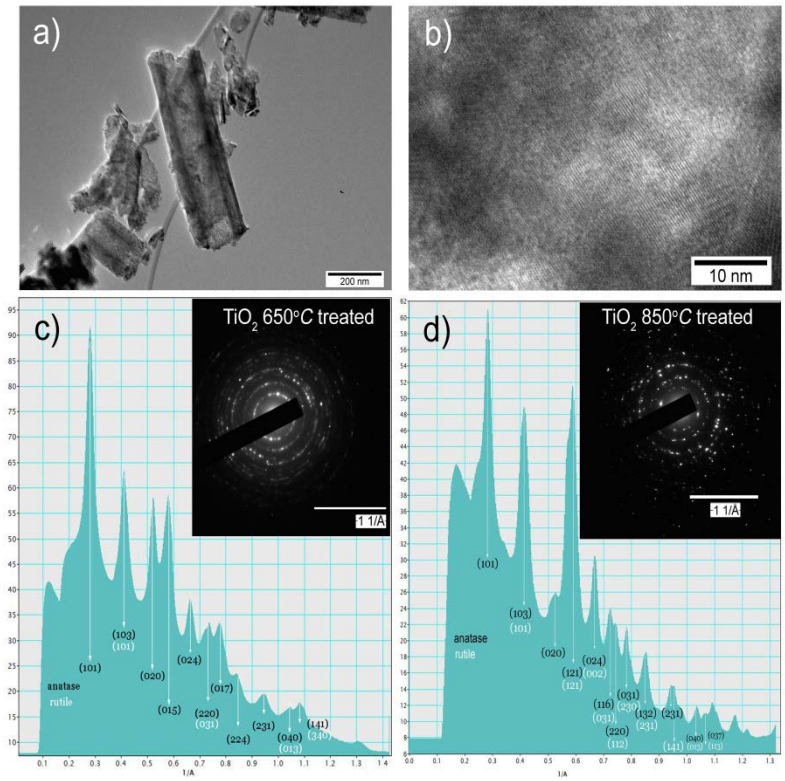


**Figure 2.** TEM analysis of $TiO_2$ nanotubes: (a) an overview image of nanotubes; (b) high resolution image of nanotube wall; selected area electron diffractogram and rotational average diagram of $TiO_2$ nanotubes treated at (c) 650 °C, and (d) 850 °C.

Almost all observed reflections can be attributed to rutile and anatase phases. The results correlate well with the data reported in previous publications in which the concentration of phases is changing at applied calcination regimes [25]. Some ambiguity in phase distinction between anatase *I4/amd* and rutile *P42/mnm* phases of titania comes from the fact that they both are of tetragonal space group and big part of their *d*-values coincides. Both crystal structures consist of $TiO_6$ octahedra, sharing four edges in anatase and two in rutile [26 – 29]. Polyhedral models of $TiO_2$ simulated in Diamond (Crystal Impact) software are presented in Figure 3.

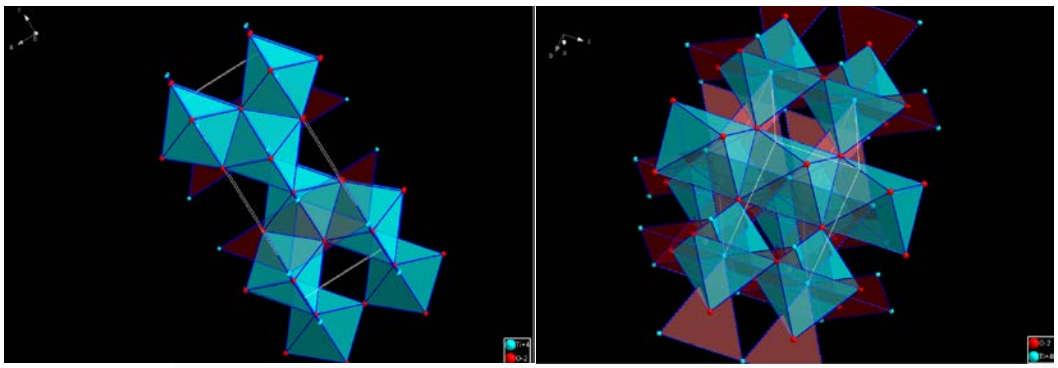

**Figure 3.** Three-dimensional representation of $TiO_6$ octahedra arrangement in anatase and rutile crystalline phases.

**MB Photodegradation**

Two types of titania nanotubes were investigated for photocatalytic degradation of MB. The first sample was subjected to thermal treatment in air at 650 °C and represented the anatase phase, while the sample treated at 850 °C represented a mixture of anatase and rutile phases of $TiO_2$. Depending on the annealing temperatures, the bandgap of $TiO_2$ is changing from 3.2 eV for anatase to 3.0 eV for rutile phase. Because of the band-to-band transitions identified in the UV region at 375 - 410 nm and deep defects in the material [30], it can be used as a photocatalytic material in both UV and visible regions. According to ref. 6, the opened $TiO_2$ nanotubes will increase the photocatalytic activity compared to one side closed nanotubes, the chemical reactions in this case take place on the inner and outer side of the nanotube surface. The formation of oxygen bubbles as a result of chemical reactions will result in motion of nanotubes in the liquid, the permanent liquid exchange inside the nanotubes will favor the occurrence of the reactions. Mixed-phase photocatalysts with rutile–anatase compositions have been reported to exhibit enhanced photoactivity relative to single-phase titania [28, 31 – 33]. Comparing to stable rutile phase, anatase modification has wider bandgap and lower recombination rate facilitating the efficient photocatalytic reactions [29]. At the same time higher surface free energy of rutile enhances its hydrophilicity [34, 35] . It is also expected that in case of residual anatase phase remaining in titania transformed into rutile at 850 °C similarly to the mixture of two types of particles the electron transfer between two phases may enhance the efficiency of photo-oxidative reactions [28, 36].

The photodegradation process of MB using $TiO_2$ nanotubes under visible and UV light is illustrated in Figure 4, where the concentration $C_t$ (%) of remained MB is measured every 10 min during 80 min. The initial concentration of 10 μM of MB and pure water were took as 100 % and 0 % and it is used for elaboration of calibration curve.

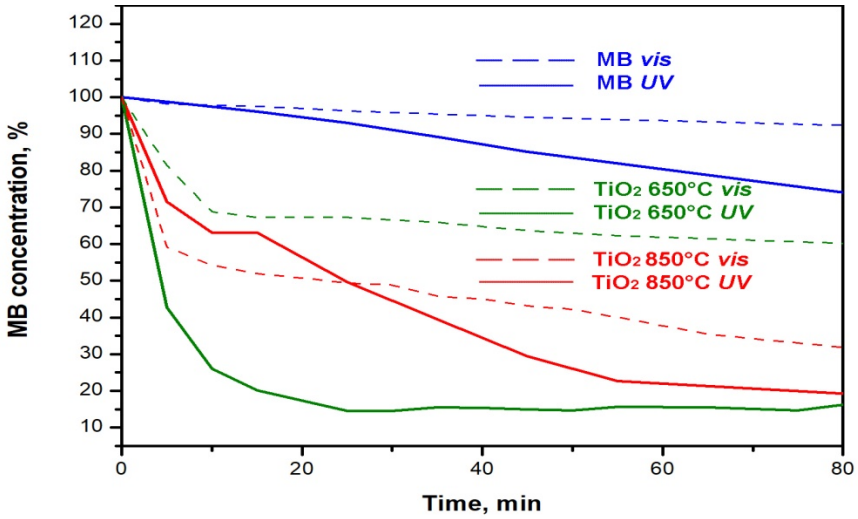


**Figure 4.** MB concentration decay in time in presence of 20 mg of $TiO_2$ nanotubes.

The dye concentration in the analyzed solution was calculated from Beer-Lambert law (Eq(1)):

$$A=\varepsilon lc \quad (1)$$

where ***A*** is the measured absorption value,

***ε*** - absorptivity of the solution at certain wavelength ***(λ)***,

***l*** - optical pathway during the measurement expressed in cm,

***c*** - solution concentration.

The ***ε*** value was calculated by a calibration absorption plot measured for 100 % concentrated MB solution at 664 nm.

Photocatalytic degradation under visible light was found to be the most efficient for $TiO_2$ with higher concentration of the rutile phase, degrading the dye till ~ 30 % concentration compared to the mixed phase of $TiO_2$ degrading the MB to 60 % during 80 min. Better photocatalytic activity of $TiO_2$ nanotubes under visible light irradiation is related to the high density of electronic defects as observed in the PL spectrum [30]. Under UV illumination, best photodegradation of MB is performed by $TiO_2$ anatase phase with 15 % dye remaining in water after only 25 min compared to 50 % for the sample with more concentration of rutile phase.

## Conclusions

It was found that both $TiO_2$ nanotubes annealed at 650 °C and 850 °C can degrade MB under UV and visible light irradiation. According to TEM analysis, the $TiO_2$ tends to transform from anatase to rutile phase with increasing the annealing temperature. The higher photocatalytic activity in the visible range was observed on samples treated at 850 °C where the rutile phase predominates, however the sample annealed at 650 °C exhibits higher photocatalytic activity under UV illumination. Because of its bandgap near visible range and the possibility to modulate it with different techniques, the $TiO_2$ nanotubes have a great potential to be used in industry for water treatment.

**Acknowledgments.** The authors acknowledge the funding from European Commission under the Grant #810652 "NanoMedTwin" and from the Ministry of Education, Culture and Research of the Republic of Moldova under the Grant #20.80009.50007.20.

**References**


1. Asghar M.I., Miettunen K., Halme J., Vahermaa P., Toivola M., Aitola K., Lund P. Review of stability for advanced dye solar cells. In: *Energy and Environmental Science*, 2010, 3(4), pp:418–426.
2. Zhu K., Neale N.R., Miedaner A., Frank A.J. Enhanced Charge-Collection Efficiencies and Light Scattering in Dye-Sensitized Solar Cells Using Oriented TiO2 Nanotubes Arrays. In: *Nano Letters*, 2007, 45(1), pp:10623–10631.
3. Qu Y., Zhou W., Pan K., Tian C., Ren Z., Dong Y., Fu H. Hierarchical anatase TiO2 porous nanopillars with high crystallinity and controlled length: An effective candidate for dye-sensitized solar-cells. In: *Physical Chemistry Chemical Physics*, 2010, 12(32), pp:9205–9212.
4. Grosjean R., Delacroix S., Gouget G., Beaunier P., Ersen O., Ihiawakrim D., Kurakevych O., Portehault D. Progress in TiO2 nanotube coatings for biomedical applications: A review. In: *Journal of Materials Chemistry B*, 2018, 13(23), pp:1862–1886.
5. Shrestha N.K., Macak J.M., Schmidt-Stein F., Hahn R., Mierke C.T., Fabry B., Schmuki P. Magnetically guided titania nanotubes for site-selective photocatalysis and drug release. In: *Angewandte Chemie - International Edition*, 2009, 48(5), pp:969–972.
6. Enachi M., Guix M., Postolache V., Ciobanu V., Fomin V.M., Schmidt O.G., Tiginyanu I. Light-Induced Motion of Microengines Based on Microarrays of TiO2 Nanotubes. In: *Small*, 2016, 12(39), pp:5497–5505.
7. Li Z., Zhang H., Zheng W., Wang W., Huang H., Wang C., MacDiarmid A.G., Wei Y. Highly sensitive and stable humidity nanosensors based on LiCl doped TiO2 electrospun nanofibers. In: *Journal of the American Chemical Society*, 2008, 130(15), pp:5036–5037.
8. Jiang Z., Yang F., Luo N., Chu B.T.T., Sun D., Shi H., Xiao T., Edwards P.P. Solvothermal synthesis of N-doped TiO2 nanotubes for visible-light-responsive photocatalysis. In: *Chemical Communications*, 2008, 1(47), pp:6372–6374.
9. Enachi M., Guix M., Braniste T., Postolache V., Ciobanu V., Ursaki V., Schmidt O.G., Tiginyanu I. Photocatalytic properties of TiO2 nanotubes doped with Ag, Au and Pt or covered by Ag, Au and Pt nanodots. In: *Surface Engineering and Applied Electrochemistry*, 2015, 51(1), pp:3–8.
10. Vakili M., Rafatullah M., Salamatinia B., Abdullah A.Z., Ibrahim M.H., Tan K.B., Gholami Z., Amouzgar P. Application of chitosan and its derivatives as adsorbents for dye removal from water and wastewater: A review. In: *Carbohydrate Polymers*, 2014, 113, pp:115–130.
11. Pan Y., Wang J., Sun C., Liu X., Zhang H. Fabrication of highly hydrophobic organic-inorganic hybrid magnetic polysulfone microcapsules: A lab-scale feasibility study for removal of oil and organic dyes from environmental aqueous samples. In: *Journal of Hazardous Materials*, 2016, 309, pp:65–76.
12. Zheng L., Wang X., Wang X. Reuse of reverse osmosis concentrate in textile and dyeing industry by combined process of persulfate oxidation and lime-soda softening. In: *Journal of Cleaner Production*, 2015, 108, pp:525–533.
13. Chatzisymeon E., Xekoukoulotakis N.P., Coz A., Kalogerakis N., Mantzavinos D. Electrochemical treatment of textile dyes and dyehouse effluents. In: *Journal of Hazardous Materials*, 2006, 137(2), pp:998–1007.
14. Manekar P., Patkar G., Aswale P., Mahure M., Nandy T. Detoxifying of high strength textile effluent through chemical and bio-oxidation processes. In: *Bioresource Technology*, 2014, 157, pp:44–51.
15. Guo J., Zhang Q., Cai Z., Zhao K. Preparation and dye filtration property of electrospun polyhydroxybutyrate–calcium alginate/carbon nanotubes composite nanofibrous filtration membrane. In: *Separation and Purification Technology*, 2016, 161, pp:69–79.
16. Nakata K., Fujishima A. TiO 2 photocatalysis: Design and applications. In: *Journal of Photochemistry and Photobiology C: Photochemistry Reviews*, 2012, 13(3), pp:169–189.
17. Lee G.J., Wu J.J. Recent developments in ZnS photocatalysts from synthesis to photocatalytic applications — A review. In: *Powder Technology*, 2017, 318, pp:8–22.
18. Cheng L., Xiang Q., Liao Y., Zhang H. CdS-Based photocatalysts. In: *Energy and Environmental Science*, 2018, 11(6), pp:1362–1391.
19. Mishra M., Chun D.M. α-Fe2O3 as a photocatalytic material: A review. In: *Applied Catalysis A: General*, 2015, 498, pp:126–141.
20. Widiyandari H., Ketut Umiati N.A., Dwi Herdianti R. Synthesis and photocatalytic property of Zinc Oxide (ZnO) fine particle using flame spray pyrolysis method. In: *Journal of Physics: Conference Series*, 2018, 1025(1).
21. Wolff N., Ciobanu V., Enachi M., Kamp M., Braniste T., Duppel V., Shree S., Raevschi S., Medina-Sánchez M., Adelung R., Schmidt O.G., Kienle L., Tiginyanu I. Advanced Hybrid GaN/ZnO Nanoarchitectured Microtubes

for Fluorescent Micromotors Driven by UV Light. In: *Small*, 2020, 16(2), pp:1–10.
22. Hou C., Hu B., Zhu J. Photocatalytic degradation of methylene blue over TiO2 pretreated with varying concentrations of NaOH. In: *Catalysts*, 2018, 8(12).
23. Ghosh T.B., Dhabal S., Datta A.K. On crystallite size dependence of phase stability of nanocrystalline TiO2. In: *Journal of Applied Physics*, 2003, 94(7), pp:4577–4582.
24. Li G., Li L., Boerio-Goates J., Woodfield B.F. High purity anatase TiO2 nanocrystals: Near room-temperature synthesis, grain growth kinetics, and surface hydration chemistry. In: *Journal of the American Chemical Society*, 2005, 127(24), pp:8659–8666.
25. Enachi M., Lupan O., Braniste T., Sarua A., Chow L., Mishra Y.K., Gedamu D., Adelung R., Tiginyanu I. Integration of individual TiO2 nanotube on the chip : Nanodevice for hydrogen sensing pss. In: *Physica Status Solidi - Rapid Research Letters*, 2015, 174(3), pp:171–174.
26. Hadjiivanov K.I., Klissurski D.G. Surface chemistry of titania (anatase) and titania-supported catalysts. In: *Chemical Society Reviews*, 1996, 25(1), pp:61–69.
27. Beltrán A., Gracia L., Andrés J. Density functional theory study of the brookite surfaces and phase transitions between natural titania polymorphs. In: *Journal of Physical Chemistry B*, 2006, 110(46), pp:23417–23423.
28. Hanaor D.A.H., Sorrell C.C. Review of the anatase to rutile phase transformation. In: *Journal of Materials Science*, 2011, 46(4), pp:855–874.
29. Muscat J., Swamy V., Harrison N.M. First-principles calculations of the phase stability of TiO2. In: *Physical Review B - Condensed Matter and Materials Physics*, 2002, 65(22), pp:2241121–22411215.
30. Pallotti D.K., Passoni L., Maddalena P., Di Fonzo F., Lettieri S. Photoluminescence Mechanisms in Anatase and Rutile TiO2. In: *Journal of Physical Chemistry C*, 2017, 121(16), pp:9011–9021.
31. Huang S.Y., Schlichthörl G., Nozik A.J., Grätzel M., Frank A.J. Charge recombination in dye-sensitized nanocrystalline TiO2 solar cells. In: *Journal of Physical Chemistry B*, 1997, 101(14), pp:2576–2582.
32. Bacsa R., Kiwi J. Effect of rutile phase on the photocatalytic properties of nanocrystalline titania during the degradation of p-coumaric acid. In: *Applied Catalysis B: Environmental*, 1998, 16(1), pp:19–29.
33. Bickley R.I., Gonzalez-Carreno T., Lees J.S., Palmisano L., Tilley R.J.D. A structural investigation of titanium dioxide photocatalysts. In: *Journal of Solid State Chemistry*, 1991, 92(1), pp:178–190.
34. Banfield J.F., Zhang H. Thermodynamic analysis of phase stability of nanocrystalline titania. In: *Journal of Materials Chemistry*, 1998, 8(9), pp:2073–2076.
35. Rupp F., Scheideier L., Olshanska N., De Wild M., Wieland M., Geis-Gerstorfer J. Enhancing surface free energy and hydrophilicity through chemical modification of microstructured titanium implant surfaces. In: *Journal of Biomedical Materials Research - Part A*, 2006, 76(2), pp:323–334.
36. Ohno T., Tokieda K., Higashida S., Matsumura M. Synergism between rutile and anatase TiO2 particles in photocatalytic oxidation of naphthalene. In: *Applied Catalysis A: General*, 2003, 244(2), pp:383–391.

*Journal of Engineering Science* *Vol. XXVIII, no. 1 (2021), pp. 31 - 37*
*Fascicle* *Industrial Engineering* *ISSN 2587-3474*
*Topic* *Materials Science and New Technologies* *eISSN 2587-3482*

**https://doi.org/10.52326/jes.utm.2021.28(1).02**
**UDC 621.565.8**

# 2D MODEL NUMERIC AMR, MODELLING AND SIMULATION OF MAGNETOCALORIC EFFECT

Dorin Botoc*, ORCID: 0000-0001-9561-9460

*"Gheorghe Asachi" Technical University of Iasi, Boulevard Profesor Dimitrie Mangeron 65, Iași 700259, Romania*
*Corresponding author: Dorin Botoc, *dorin.botoc@tuiasi.ro*

Received: 01. 19. 2021
Accepted: 02. 22. 2021

**Abstract.** In this article, the study of gadolinium material is focused on determining the constants and properties of the material, the analysis of substructures and the orientation of dipole moments. Research into material aspects provides important information on atomic-level sub-phenomena in the field of the main magnetocaloric phenomena for the magnetic refrigeration regenerator (AMR). The experimental study is mainly based on testing the magneto-caloric material with different magnetization equipment, developed to measure more precise and fine details, magnetic refrigerator, AMR prototype development and the like. The method used uses differential equations. For both cases, where the loads are relatively simple and for more complex cases, the method can be easily applied.

**Keywords:** *magnetic refrigeration, AMR, regenerable energy.*

## Background and Introduction

There is a considerable amount of literature available in which researchers have highlighted the benefits of the usage of magnetocaloric materials for the refrigeration processes and the potential of the magnetic materials has been demonstrated as an efficient energy saving materials. Gd et al studied in detail about the transduction of energy in ferromagnetic and ferroic materials, moreover the energy transduction in different types of materials such as piezo-electric, electromagnetic, and Magnetostrictive materials have been discussed in details and relevant advantages and disadvantages were also mentioned [1]. In Europe and America, huge amount of energy is wasted on the refrigeration and air conditioning, by adopting an energy efficient approach such as magnetocaloric refrigeration or magnetic refrigeration, a huge amount of energy can be saved [2]. The main reason for increased interest in the magnetic refrigeration is due to the environmentally friendly operation, highly energy efficient, and absence of requirement for the usage of harmful gases which cause ozone depletion and other effects such as greenhouse which contribute to the global warming.

The efforts are being made for the development of the refrigerator which can work at room temperature. There have been various successful attempts on the trial or experimental level, such as the individual products developed by General electric and Haier. The properties which are usable for the refrigeration effect are due to extraordinary

response of these materials to external magnetic fields, the exhibition of such properties occur close to Curie temperature, it is the temperature at which the basic self-possessed magnetic properties are diminished, and the material temperature is dependent upon the application of the magnetic field. The effect mentioned previously has been in use since 1920, for the examination of the magnetic structure and properties of iron and other related elements. The magnetocaloric effect was first discovered by the E. Warburg in 1881, who was a German physicist. The study tends to report the important developments and highlight the major breakthrough which have led to the acquirement of toady's knowledge and understanding about the magnetocaloric effect. Faraday's discovery that time variation of magnetic flux results in the induction of electric currents. Joule's understanding cleared the important concepts related to the electric currents and associated heat energy, and it was declared that heat energy released due to flow of electromagnetically induced current is equivalent to the heat energy produced due to the electric current produced by any other source, moreover, it was also inferred that rapid magnetization and demagnetization results in the heating of the magnetic material due to heat energy released as a result of current flow. Thomson inferred from the concepts of thermodynamics that temperature dependent property of magnetization of any material will represent or exhibit these properties related parameters in the form increase or decrease in temperature.

The accurate quantifiable measurement of magnetocalorific effect of iron was possible after a long time since the discovery of phenomena [3]. As there were issues related to high temperature which made the measurement of the related parameters challenging. The heat based electric motor was presented and produced by Tesla, Edison, and Stefan. Weiss and Langevin contributed separately the considerable knowledge and understanding about the temperature ranges, magnetization, and hysteresis. The initiation of the low temperature studies which had ultimately led to the realization and theoretical formulation of refrigeration was independently reported by Debye and Giauque that adiabtically demagnetized paramagnetic salts results in the attainment of low temperatures, Giauque and MacDougall showed the very low temperature achievements by the salts [4]. All the work reported above resulted in the development of foundation for the concepts building and actual understanding of magnetism, temperature, and material properties. Pecharsky et al. reported that the magnetic dipole moments of Gd can be put in order at room temperature (294 K), and the researchers highlighted that the continuous magnetic refrigeration was experimentally shown by the Collins and Zimmerman, they tested magnetic refrigerators operating at very low temperature ranges [5]. Zimm and DeGregoria explained the basic mechanism of Active magnetic regenerator cycle. Kitanovski et al. highlighted that the there is need and necessity to develop new thermodynamic cycles which can explain the magnetic refrigeration phenomena accurately and comprehensively and, the authors reported many publications about the Brayton and Ericsson's cycle associativity with the magnetic refrigeration, moreover, active magnetic regenerators with various thermodynamic cycles was analyzed, and numerical simulation of AMR was also performed using finite element method. The AMR operating on the Brayton cycle resulted in the production of highest cooling power capability, while AMR operating on the Ericsson cycle is the most efficient one [6], they also mathematically explained the numerical aspects of AMR simulation. Wolf et al provided quantum-based explanation of the magnetocaloric effect and proposed the increment or increase in the change in the entropy with respect to change in the magnetic field close to magnetically achieved

quantum-critical point by the accurate and precise measurement of calorimetric effect [7]. Noume et al. used comsol of simulation of magnetocaloric effect for the designing of the magnetic regeneration cycle for the electric vehicles. As the electric vehicle operates on the battery, therefore, the energy would be derived from the battery, in the simulation performed, the fluid flow (mainly laminar),heat transfer in solids and fluids was used, and the velocity, temperature, and heat transfer coefficient was mainly studied [8].

**Boundary condition, mesh**

The primary equation which is used for the fluid flow is the Navier-Stokes equation, moreover, energy equation along with the heat transfer equations were mainly used [9]. Gobi and Sahu used COMSOL to perform the exploratory study of the magnetocaloric effect on three different materials, these materials were Gadolinium and two other different alloys for the evaluation of the final temperature of the magnetic material, the Gadolinium showed the adiabatic temperature difference of 12 K which was the highest among the studied material [10]. An application was developed having a graphical user interface (GUI), so that the user can input different variables, and visualize the contours of temperature and other variables. The mathematical based study is more equation oriented, in which mathematical techniques are employed to explain the physics of phenomena, and these study methods are valuable in terms of quantification of the variables and developing actual mathematical relations.

**Results and disscution**

The boundary condition of magnetic field is the Ampere's law which was applied on the regenerator, and the magnetization condition was defined. The magnetization model was applied, and the material was declared as solid, value of the magnetization defined was 222000 A/m in x and y directions, and the values of electrical conductivities and relative permittivity were derived from the material. Magnetic insulation was also applied at the relevant boundaries.

The heat transfer in solids and fluids have boundary conditions of identification of the fluidic domain and solid domain, and the temperature was defined which was initial temperature of 293.15 Kelvin. The heat rate of 100 Watt was applied as the heat source at the regenerator. Similarly, the boundary conditions of the fluid ere applied defining inlet, outlet and wall. The normal inflow velocity of 5 m/s was applied at the input, and the zero-velocity boundary condition was defined at the outlet. The proposed multi-physics option which the solver has provided consist of electromagnetic heating and non-isothermal flow conditions. The walls have been modeled with no slip boundary conditions.

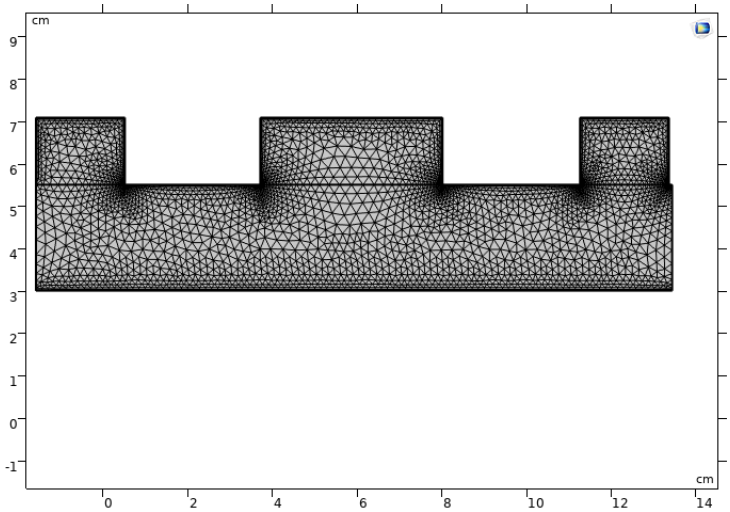


**Figure 1**. Comsol 2D model used for the simulation has been shown along with the mesh.

The physics-controlled mesh was used for the simulation.

Fig. 1 show the meshed domain, the mesh is very fine at the boundaries and edges.
The mesh is very fine at the boundaries and edges. The contributor of the mesh are magnetic fields, heat transfer in solids and fluids, laminar flow, electromagnetic heating, and non-isothermal flows.The stationary study was selected along with the PARSIDO solvers.

**Modelling and simulation**

The process modelling and simulation was performed in COMSOL multi-physics. The model was drawn in 2D and was inspired by the research performed by the Noume et al. 2D model was drawn in the Comsol model builder geometry tab. The model assumes to have symmetry.

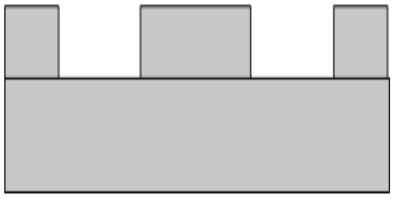

**Figure 2**. Geometrical representation of the model.

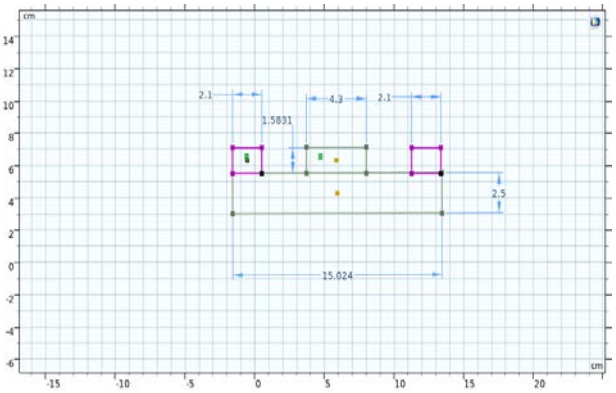


**Figure 3.** Comsol 2D AMR model used for the simulation of magnetocaloric effect along with the dimensions of various bodies used.

The length of the fluidic channel is 15.024 cm, while the height of the fluidic channel was kept as 2.5 cm. the magnetic regenerator has been placed at the center of the channel, and the width and height of the magnetic regenerator was kept as 4.3 cm and 1.5 cm respectively. The right-side square box was modeled as hot heat exchanger and the left side box was modelled as cold heat exchanger. The width and height of both the heat exchanger are 1.5 and 2.1 cm respectively. Figure 2 shows the complete dimensions of the model.

The materials were also selected according to the simulations performed by Noume et al.. The magnetic regenerator placed in the center was allotted the material Gadolinium, the fluid used in the simulation is water, and the plates used to model the heat exchanger is composed of copper. The material properties off copper used in the simulation along with comsol operators are shown below [11 - 13].

The physics selected for the simulations are the main determinants of the solution and boundary conditions. The models which were used in the simulation are, Magnetic fields, Heat transfer in solids, heat transfer in fluids, and Laminar flow for the fluidic solvers. All these physics have been coupled together to find a numerical solution of the magnetocaloric effect problem. COMSOL multi-physics excellently couples the physics to formulate a multi-physics problem, and the user friendly interface allows the user to add multiple studies within one window. The proposed multi-physics based on different physics selected are also shown in the multi-physics tab, and the option is provided to apply it on different domains and boundaries. All the previously defined steps allow the user to

comprehensively define the problem [14 - 15]. Magnetic flux density norm along with temperature plot have been obtained. Fig.4 shows the magnetic flux density norm streamlines. Figure 5 also show the Magnetic flux density plot. The magnetization has produced the magnetic field.

The values of the temperature has been almost the same that were obtained by the Noume et al. in their simulations. The temperature rise due to magneto caloric effect is similar in magnitude that has been reported in the literature. It must be mentioned that the stationary study has been performed in order to simulate the process.

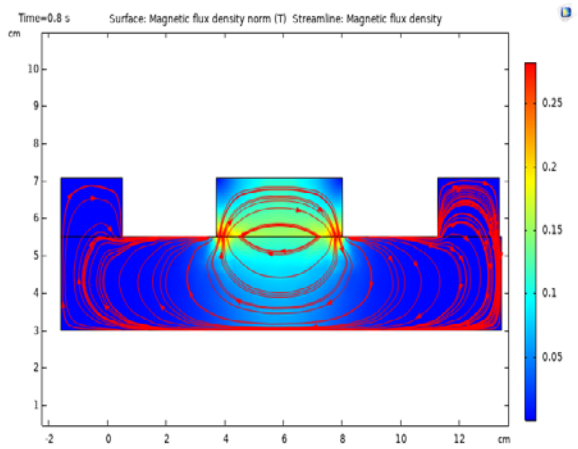


**Figure 4.** Magnetic flux density norm shown in the figure. The magnetization can be viewed from the streamlines.

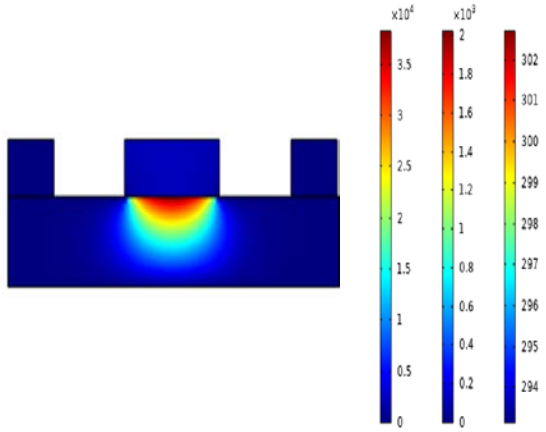


**Figure 5.** Temperature profile AMR.

Successful simulations have been performed by using the simplified model techniques and methods. For more realistic analysis transient approach should be adopted. The laminar flow approach has also been adopted in order to reduce the complexity of the solution procedure, otherwise the flow may be considered turbulent due to heat transfer and fluid flow in the current scenario. The material which was chosen for the study was widely used in the research of magnetocaloric materials.

There are other alloys which are members of lanthanide period have also been studied by the researchers in order to explore the potential for the refrigeration in the magnatocaloric materials. The tolerance set for the stationary solver was 0.001 default. MUMPS solver along with the PARSIDO solver was also used. The results have been evolved with the start of the flow. Figure 6 shows the contours of the magnetic flux density when the flow conditions were applied, for this case the magnetization was elevated to 450000A/m.

Figure 7 shows the total heat flux magnitude. The heat energy dissipation can be viewed by examining the surface plot presented below.

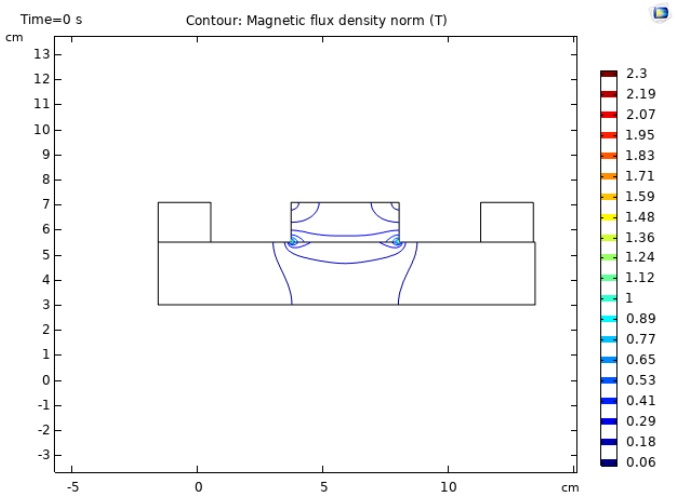


**Figure 6.** Magnetic flux density upon the application of the fluid flow conditions.

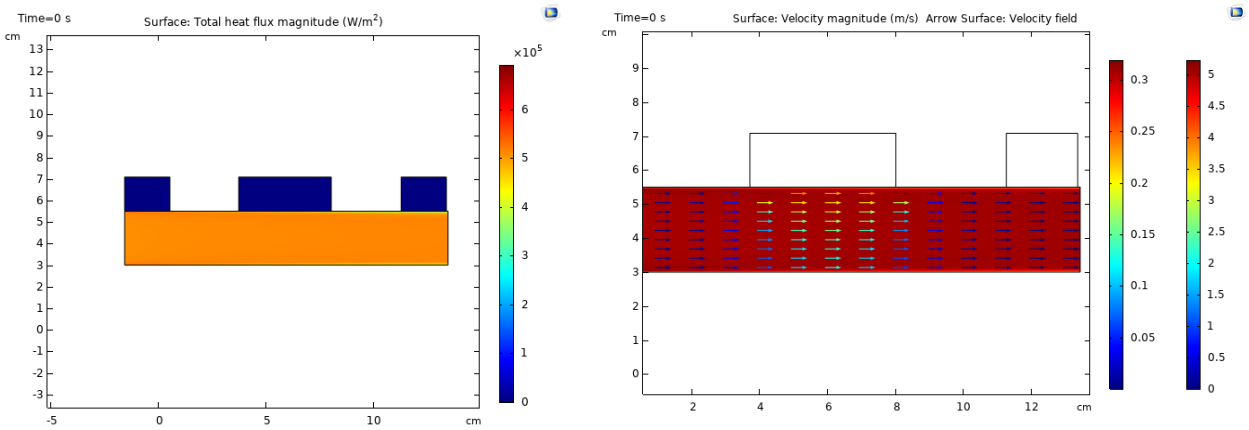


a) b)

**Figure 7.** a) Total heat flux magnitude plot, b) combined arrow and surface velocity plot just after the start of the flow.

The flow conditions which have been assumed for the analysis are very much simplified. The very simple yet comprehensive case studied combines the equations from the magnetic field, the heat transfer equations considering the effects of convection and conduction, and the flow equations which are continuity, momentum, and energy balance equations.

**Conclusions and perspectives**

In this study finite element analysis technique would be adopted in order to perform simulation material of magnetocaloric effect and parametric material study on the alloys. Finite element analysis is a numerical technique, in which the computational domain or body of interest is discretized into smaller discrete elements (mesh), and the relevant equations are solved for each mesh element or node. In this way the accurate and complete behavior of the object under defined loading conditions is attained. There are three methods normally used for the solution of a real world problem, these methods are, experimental, exact method (analytical) and numerical method. Experimental method provides accurate and actual solution of the problem, if the experiment is properly designed. However, for some cases it is difficult to design the experimental setup, moreover this method is expensive in the case when parameters have to be varied or the intension is to perform parametric study. The analytical method is based on the exact mathematical solution of the problem. This method uses the differential equations, for the simple cases in which loadings is simple, or for over simplified cases, the method can be applied easily.

**References**

1. A. Kitanovski, "Energy Applications of Magnetocaloric Materials", *Advanced Energy Materials*, vol. 10, no. 10, p. 1903741, 2020.
2. P. Shirron, "Applications of the magnetocaloric effect in single-stage, multi-stage and continuous adiabatic demagnetization refrigerators", *Cryogenics*, vol. 62, pp. 130-139, 2014
3. V. Franco, J. Blázquez, J. Ipus, J. Law, L. Moreno-Ramírez and A. Conde, "Magnetocaloric effect: From materials research to refrigeration devices", *Progress in Materials Science*, vol. 93, pp. 112-232, 2018
4. V. Pecharsky and K. Gschneidner, Jr., "Giant Magnetocaloric Effect in Gd5(Si2Ge2)", *Physical Review Letters*, vol. 78, no. 23, pp. 4494-4497, 1997
5. Eriksen D, Engelbrecht K, Bahl C, Bjørk R. "Active magnetic regenerator refrigeration with rotary multi-bed technology." *Department of Energy Conversion and Storage, Technical University of Denmark*, 2016. 146 p

6. N. Mezaal, K. Osintsev and T. Zhirgalova, "Review of magnetic refrigeration system as alternative to conventional refrigeration system", *IOP Conference Series: Earth and Environmental Science*, vol. 87, p. 032024, 2017
7. S. Kulkarni, and A. Mashalkar, "Study of Magnetic Refrigeration", *International Journal for Research in Engineering Application & Management (IJREAM)*, no. -, 2018
8. W. Gao et al., "Energy transduction ferroic materials", *Materials Today*, vol. 21, no. 7, pp. 771-784, 2018
9. A. Smith, "Who discovered the magnetocaloric effect?", *The European Physical Journal H*, vol. 38, no. 4, pp. 507-517, 2013
10. V. Pecharsky and K. Gschneidner Jr, "Magnetocaloric effect and magnetic refrigeration", *Journal of Magnetism and Magnetic Materials*, vol. 200, no. 1-3, pp. 44-56, 1999
11. A. Kitanovski, U. Plaznik, J. Tušek and A. Poredoš, "New thermodynamic cycles for magnetic refrigeration", *International Journal of Refrigeration*, vol. 37, pp. 28-35, 2014
12. B. Wolf et al., "Magnetocaloric effect and magnetic cooling near a field-induced quantum-critical point", *Proceedings of the National Academy of Sciences*, vol. 108, no. 17, pp. 6862-6866, 2011
13. A. Noume, M. Risser and C. Vasile, "Modeling of a Magnetocaloric System for Electric Vehicles", in *Comsol Conferrence*, Rotterdam, 2013
14. S. Gombi and D. Sahu, "Exploration of selected room temperature magneto caloric materials using COMSOL multiphysics", *IOP Conference Series: Materials Science and Engineering*, vol. 577, p. 012160, 2019
15. C. Hsieh, Y. Su, C. Lee, P. Cheng and K. Leou, "Modeling of Graded Active Magnetic Regenerator for Room-Temperature, Energy-Efficient Refrigeration", *IEEE Transactions on Magnetics*, vol. 50, no. 1, pp. 1-4, 2014

*Journal of Engineering Science* *Vol. XXVIII, no. 1 (2021), pp. 38 - 46*
*Fascicle* *Industrial Engineering* *ISSN 2587-3474*
*Topic* *Applied Engineering Sciences and Management* *eISSN 2587-3482*

**https://doi.org/10.52326/jes.utm.2021.28(1).03**
**UDC 004.89:004.932**

# CENTRAL AND LOGARITHMIC CENTRAL IMAGE CHORD TRANSFORMATIONS FOR INVARIANT OBJECT RECOGNITION

Veaceslav Perju[1]*, ORCID 0000-0002-7755-4277,
Vladislav Cojuhari[2], ORCID 0000-0001-7540-2184

[1]*Agency for Military Science and Memory*
*47, Tighina Str., Chisinau, MD2001, Republic of Moldova*
[2]*Ministry of Internal Affairs*
*75, Stefan cel Mare Bld, Chisinau, MD2012, Republic of Moldova*
*Corresponding author: Veaceslav Perju, *vlperju@yahoo.com*

Received: 11. 28. 2020
Accepted: 01. 19. 2021

**Abstract.** Pattern descriptors invariant to rotation, scaling, and translation represents an important direction in the elaboration of the real time object recognition systems. In this article, the new kinds of object descriptors based on chord transformation are presented. There are described new methods of image presentation - Central and Logarithmic Central Image Chord Transformations (CICT and LCICT). It is shown that the CICToperation makes it possible to achieve invariance to object rotation. In the case of implementation of the LCICT transformation, invariance to changes in the rotation and scale of the object is achieved. The possibilities of implementing the CICTand LCICToperations are discussed. The algorithms of these operations for contour images are presented. The possibilities of integrated implementation of CICT and LCICT operations are considered. A generalized CICT operation for a full (halftone) image is defined. The structures of the coherent optical processors that implement operations of basic and integral image chord transformations are presented.

**Keywords**: *image, chord, transformation, recognition, processor*.

## Introduction

Invariant Object Recognition (IOR) is of great importance for many civil and military applications and supposes the identification and classification of the object in real-time, regardless of spatial position, angular orientation, etc.

Different directions and approaches exist in IOR, such as using the support vector machines [1], deep learning techniques [2], neural networks [3], image moments feathers [4, 5], correlation techniques [6, 7], etc.

A pattern descriptors invariant to rotation, scaling, translation (RST) represent an important direction in IOR. In article [8] the RST invariance is obtained by applying the Fourier–Mellin transform on the radial and angular coordinates of the pattern's Radon image. In article [9] a novel descriptor is proposed based on the ring-projection and dual-tree complex wavelets which permit the transformation of the pattern from a 2-D image to

a 1-D signal. In article [10] the Hough transform realization is proposed in an incoherent optical processor.

The described above approaches in IOR need substantial computational expenditures which in many cases do not permit the realization of real-time. Also, numerical accuracy does not correspond to the standards.

One of the perspective directions in object recognition is based on the chord functions using due to their properties of invariance to the object position, rotation, or scaling changes. In the article [11] a hybrid optical-digital system for chord functions calculation is described. In article [12] an optical processor that realizes a generalized chord transformation is presented. The wedge-ring detector samples of autocorrelation are shown to be the histograms of the chord distributions. In article [13] a logarithmic chord transformation of the images (LHTI) is proposed. Structures of an optical-electronic processor for LHTI realization and of a system for object recognition are described.

In this article, the results of the development of the invariant object recognition based on the new kinds of the chord transformation are presented. Section 2 describes new methods of image transformations - Central and Logarithmic Central Image Chord Transformation (CICT and LCICT).

It is shown that the CICToperation makes it possible to achieve invariance to object rotation. In the case of implementation of the LCICTtransformation, invariance to changes in the rotation and scale of the object is achieved. In section 3 the possibilities of implementing the CICT and LCICT operations are discussed. The algorithms of these operations for contour images are presented.

The possibilities of integrated implementation of CICT and LCICT operations are considered. A generalized CICT operation for a full (halftone) image is defined. The structure of a coherent optical processor that implements operations of integral image chord transformation is presented.

**1. Central and logarithmic central image chord transformations**

Let P(x,y) is an initial object (Figure 1.a) and $P_b(x,y)$ is the function of the object's image, which is described by the binary external contour, $P_b(x,y)=\{0,1\}$, and $(x_c,y_c)$ – coordinates of the center (Figure 1.b). For every pair of points $(x_i,y_i)$ and $(x_k,y_k)$ is constructed a chord $A_iB_k$ passing through the point $(x_c,y_c)$, is determined the angle $\psi_{ik}$ between chord and X-axis, and chord's length $R_{ik}$ as:

$$\psi_{ik} = arctg[(y_k - y_i)/(x_k - x_i)] \quad (1)$$

$$R_{ik} = \sqrt{(x_k - x_i)^2 + (y_k - y_i)^2} \quad (2)$$

In this case, the object's image can be characterized by the function $H(\psi_{ik},R_{ik})$, which describes all possible chords drawn through the point $(x_c,y_c)$. Transformation, through which was obtained the function $H(\psi_{ik},R_{ik})$ will be named the Central Image Chord Transformation (CIHT):

$$P_b(x,y) \rightarrow T\{P_b(x,y)\}=H(\psi_{ik},R_{ik})=H(x_1,y_1)=P_b(x_1,y_1), \quad (3)$$

where T{...} – the operation of CIHT,

$$x_1=\psi_{ik},\ y_1=R_{ik}. \quad (4)$$

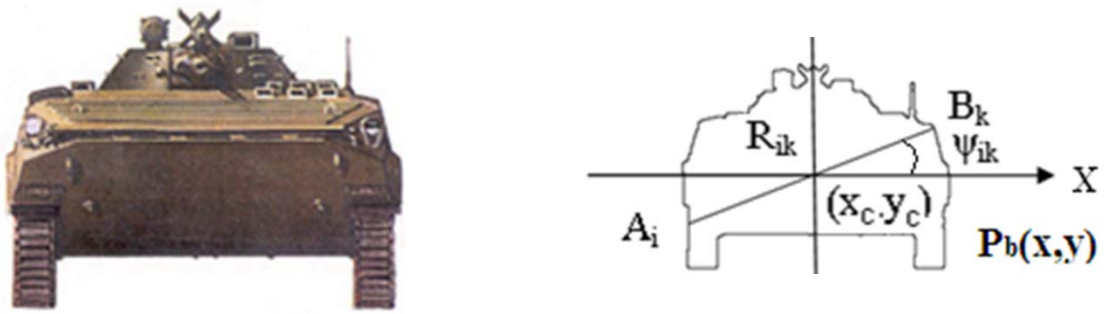


a) b)

**Figure 1.** Initial (a) and countered (b) objects.

Let's introduce the definition of Logarithmic Central Image Chord Transformation ( LCICT). This transformation is realizing by taking the logarithm of the parameter $R_{ik}$ of the function $H(\psi_{ik},R_{ik})$:

$$LT\{H(\psi_{ik},R_{ik})\}=LH(\psi_{ik},\ln R_{ik})=LH(\psi_{ik},w_{ik})=P_b(x_2,y_2) \quad (5)$$

where LT{...} – the operation of LCICT,

$$x_2=\psi_{ik},\ y_2=w_{ik}=\ln R_{ik} \quad (6)$$

In Figure 2 are presented the transformations CICT(a) and LCICT(b). It is evident, that the rotation of the initial image will shift the function R(ψ) along the axis ψ, i.e. the CICToperation allows to achieve invariance to the rotation of the object. In the case of the LCICTtransformation, the object scale change will shift the function lnR(ψ) along the axis LnR, i.e. this transformation allows to achieve the invariance to the scale change.

### 3. Possibilities of the image chord transformation's realization

Let's consider the possibilities of the CICT and LCICT operations realization. Let the input image contain an object P(x',y') located in the area of interest's center with coordinates $(x_c,y_c)$. The function P(x',y') is converted to a binary image or represented by its external binary contour:

$$P(x',y') \rightarrow P_b(x,y), \quad (7)$$

where $P_b(x,y)=\{0,1\}$.

Then, for an angle ψ varying within 0-180°, the chords are constructed, passing through the point $(x_c,y_c)$, their lengths $R_{ik}$ are determined, and the functions $H(\psi_{ik},R_{ik})=P_b(x_1,y_1)$, $LH(\psi_{ik},w_{ik})=P_b(x_2,y_2)$ are formed. The described operations of CICTand LCICTcan be realized in the software or in digital signal processors, as well as in the specialized optical processors.

#### *3.1. Optical processor for image chord transformation*

The processor contains (Figure 3) a coherent radiation source 1, an image input module 2, a matrix of threshold optrons 3, a photodetector 4, and a controller 5. The image input module 2 is an electro-optical spatial light modulator (SLM) that operates in the light transmission mode. The matrix of threshold optrons 3 performs the image binarization operation. Photodetector 4 realizing radial (output A) and logarithmic radial (output B) image scanning. Controller 5 synchronizes the operation of processor units, data storage, and communication with external devices.

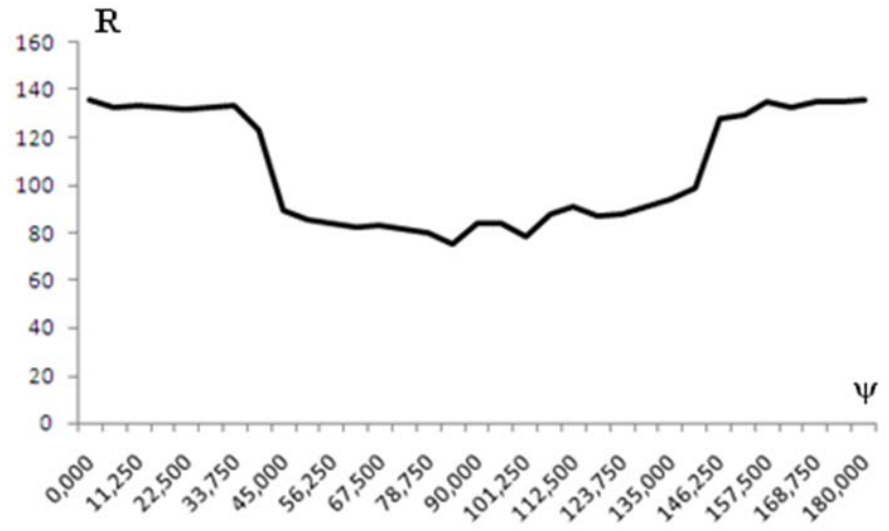


a)

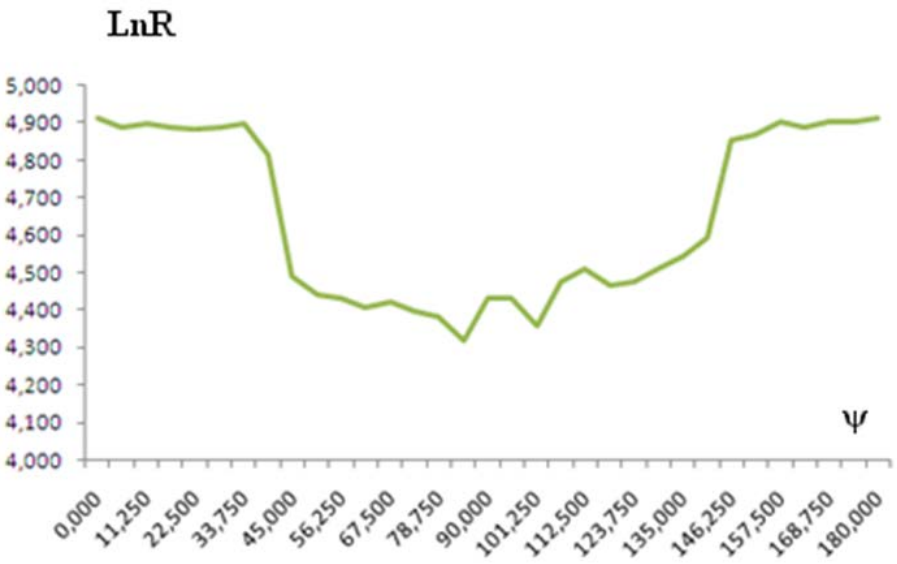


b)

**Figure 2.** Transformations CICT(a), and LCICT(b).

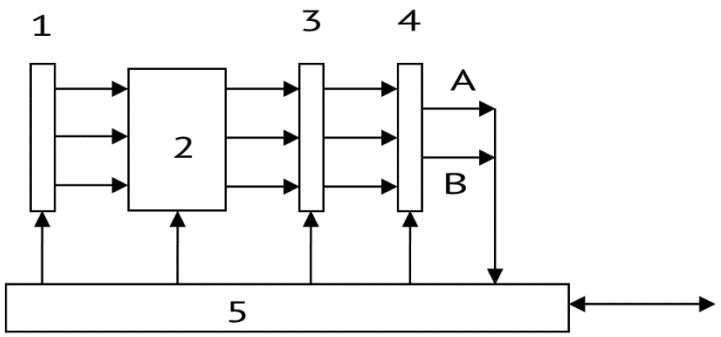


**Figure 3.** Optical processor for image chord transformation.

The processor functions as follows: centered image of the object P(x',y') is recorded on a SLM 2. Then switch on the radiation source 1, the light beam from the output of which passes through the SLM 2, is modulated by the intensity function P(x',y') and flows through the matrix of optrons 3. As a result, the function P(x',y') is binarized: P(x',y') → $P_b$(x,y) and

then goes to the photodetector matrix 4, at the outputs A and B of which the transformations CICT and LCICT are formed respectively. The corresponding signal values are entered into controller 5.

### *3.2. Integral realization of CICTand LCICToperations*

The integral realization of chord transformations CICT and LCICT assumes the following. Because the values of the function $P_b(x,y)$ in boundary points of the object are defined as $P_b(x,y)=1$, the chord will exist between the two image points if they are a boundary, i.e.

$$G(x_i, y_i, \psi_{ik}, R_{ik}) = P_b(x_i, y_i)P_b[x_i + R_{ik}\cos\psi_{ik}, y_i + R_{ik}\sin\psi_{ik}] = 1 \tag{8}$$

At various values of the points' combinations on the external contour of the object, the operation CICTwill be determined as follows:

$$\begin{aligned} &H(\psi_{ik}, R_{ik}) = \iint G(x_i, y_i, \psi_{ik}, R_{ik})dxdy = \\ &\iint P_b(x_i, y_i)P_b[x_i + R_{ik}\cos\psi_{ik}, y_i + R_{ik}\sin\psi_{ik}]dxdy \\ &= \iint P_b(x_i, y_i)P_b[x_i + \xi_{ik}, y_i + \eta_{ik}]dxdy = H(\xi_{ik}, \eta_{ik}) = P_b(x,y) * P_b(x,y) \end{aligned} \tag{9}$$

where $\xi_{ik} = R_{ik}\cos\psi_{ik}, \eta_{ik} = R_{ik}\sin\psi_{ik}$

Thus, the CICToperation can be implemented by calculating the autocorrelation function of the contour image $P_b(x,y)$. For a full (halftone) image P(x,y), the generalized CICT operation will be defined as:

$$H(\psi, R) = H(\xi, \eta) = \iint P(x,y)P[x+\xi, y+\eta]dxdy = P(x,y) * P(x,y) \tag{10}$$

Let's define the generalized LCICToperation as:

$$LH(\psi, W) = CT\{H(\xi, \eta)\} = H[\xi', \eta'] \tag{11}$$

where CT{...} is the coordinate transformation operation,

$$\xi' = \text{arctg}(\eta/\xi),\ \eta' = [\ln(\xi^2 + \eta^2)]/2 \tag{12}$$

Let's show that the generalized LCICT operation is invariant to shift, change in the angular orientation and scale of the image. Let the input image be described by the function:

$$P(x', y') = P[x + e_3, y + e_4, e_1, e_2),$$

where $e_1, e_2$ - change of scale, the angular orientation of the object, respectively; $e_3, e_4$ - parameters of the object's displacement. The calculation of the autocorrelation functions leads to the elimination of the influence of parameters $e_3, e_4$. Really,

$$\begin{aligned} &H(\xi, \eta) = \iint P(x', y')P(x' + \xi, y' + \eta]dx'dy' = \\ &= FT^{-1}\{FT[P(x', y')]FT^*[FTP(x', y')]\} = \\ &= FT^{-1}\{\exp[j(ue_3 + ve_4)]P(u', v')\exp[-j(ue_3 + ve_4)P^*(u', v')\} = \\ &= FT^{-1}\{P(u', v')P^*(u', v')\} = H(\xi_1', \eta_1'), \end{aligned} \tag{13}$$

where FT, FT$^{-1}$, FT* are the direct, inverse, and complex conjugate Fourier transform, respectively. Values $\xi_1^{'}, \eta_1^{'}$ are functions of parameters $e_1, e_2$: $\xi_1^{'} = F_1(e_1, e_2), \eta_1^{'} = F_2(e_1, e_2)$.

Image transformation, made by (13) allows separating the influence of the scale e1 and rotation e2 parameters of the object and reducing them to equivalent shifts:

$$H^{'}(\psi, W) = CT\{H^{'}(\xi_1^{'}, \eta_1^{'})\} = H_o\{\xi + \xi_o(e_2), \eta + \eta_o(e_1)\}, \tag{14}$$

where $\xi_o(e_2)$ $\eta_o(e_1)$ are constant.

Thus, as a result of the LCICT operation, invariance to shifts, changes in the scale, and angular orientation of the object are achieved. This will allow reducing significantly the volume of computing costs in the subsequent stages of digital processing.

In Figure 4 is shown the structure of a coherent optical processor that implements operations of integral image chord transformation. The processor contains a coherent radiation source 1, an optical image input module 2, electro-optical SLMs 3 and 4, a Fourier lens 5, a photodetector 6, and a controller 7. The SLM 3 is used for recording the input image.

The SLM 4 is used for displaying the functions Φ(ξ, n) at the stage of optical realization of image transformation to logarithmic polar (15) or polar (16) coordinate system:

$$\Phi_{lp}(\xi, \eta) = \begin{cases} \Phi_{+}(\xi, \eta) = (\xi / 2)\ln(\xi^2 + \eta^2) + \xi] & at \quad \xi < 0 \\ \Phi_{-}(\xi, \eta) = \Phi_{+}(\xi, \eta) - (2\pi^2 / \lambda f_L)\eta & at \quad \xi > 0 \end{cases} \tag{15}$$

$$\Phi_{p}(\xi, \eta) = \begin{cases} \Phi_{+}(\xi, \eta) = \xi(\xi^2 + \eta^2) + \xi] & at \quad \xi < 0 \\ \Phi_{-}(\xi, \eta) = \Phi_{+}(\xi, \eta) - (2\pi^2 / \lambda f_L)\eta & at \quad \xi > 0 \end{cases} \tag{16}$$

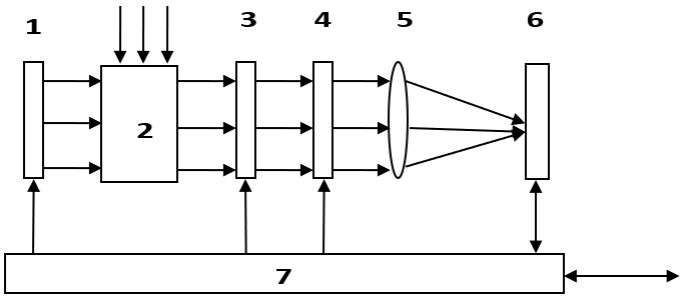


**Figure 4.** Optical processor for integral image chord transformation.

In expressions (15), (16) $\lambda$ – the wavelength of the radiation source 1; $f_L$ – the focal length of the Fourier lens 5. For the function Φ(ξ,n), recorded on SLM 4 and described by the expression (15) or (16), the processor will implement the LCICT or CICT operation, respectively. Module 2 has two optical inputs and one optical output. The photodetector 6 is designed to scan the optical Fourier transform formed by lens 5 and subsequent data input into the controller 7.

The processor function in the next mode. In the initial state, the input image P(x', y') is recorded on the SLM 3, and the SLM 4 is transparent. Then the source of radiation 1 is switched on, the collimated light beam from the output of which goes through module 2,

SLM 3, is modulated by the image function P(x',y') and then passing through the SLM 4. Lens 5 performs a two-dimensional Fourier transform of the image P(x',y'):

$$FT\{P(x^{'},y^{'})\}=\exp[j(u^{'}e_3+v^{'}e_4)]P(u^{'},v^{'}), \tag{17}$$

where $u^{'}=F_3(e_1,e_2),v^{'}=F_4(e_1,e_2)$.

The optical distribution (17) is reflected in the photodetector 6 as a Fourier spectrum:

$$\begin{aligned}P_s(u^{'},v^{'})&=\left|FT\{P(x^{'},y^{'})\}\right|^2=FT\{P(x^{'},y^{'})\}FT^{*}\{P(x^{'},y^{'})\}=\\&=\exp[j(u^{'}e_3+v^{'}e_4)]P(u^{'},v^{'})\exp[-j(u^{'}e_3+v^{'}e_4)*P(u^{'},v^{'})=\\&=P(u^{'},v^{'})P^{*}(u^{'},v^{'}).\end{aligned} \tag{18}$$

Next, the distribution (18) is scanned by the photodetector 6 and recorded on the SLM 3 through the controller 7. Using the lens 5, the Fourier transform of the function (18) is performed, as a result of which will be obtained an optical distribution in the plane of the photodetector 6, described as follows:

$$\begin{aligned}&FT\{P(u^{'},v^{'})P^{*}(u^{'},v^{'})\}.=FT\{FT[P(x^{'}_1,y^{'}_1)]\}FT\{FT^{*}[P(x^{'}_1,y^{'}_1)]\}=\\&=FT\{FT[P(x^{'}_1,y^{'}_1)]\}*FT\{FT[P(-x^{'}_1,-y^{'}_1)]\}=P(x^{'}_1,y^{'}_1)*P(x^{'}_1,y^{'}_1)\end{aligned} \tag{19}$$

where * is the correlation operation, $x^{'}_1=F_3(e_1,e_2),y^{'}_1=F_4(e_1,e_2)$.

The distribution (19) represents an autocorrelation function of the input image:

$$\left|P(\xi^{'},\eta^{'})\right|^2=\left|P(x^{'}_1,y^{'}_1)*P(x^{'}_1,y^{'}_1)\right|^2. \tag{20}$$

As a result, the influence of parameters $e_3,e_4$ was eliminated. The optical distribution described by the function (20) is scanned by the photodetector 6 and written to the SLM 3 via the controller 7. By this time, on the SLM 4, the function is written by the expression (15) or (16), which allows multiplying this function with the function from the SLM 3. As a result, at the output of SLM 4, the optical distribution will be characterized by the function: $P(\xi,\eta)=\left|P(\xi^{'},\eta^{'})\right|\exp[j\Phi(\xi,\eta)]$. After the Fourier transform realized using lens 5, an optical distribution will be formed in the plane of the photodetector 6:

$$FT\{\left|P(\xi,\eta)\right|\exp[j\Phi(\xi,\eta)]\}=H(\psi,G), \tag{21}$$

where G= $w=[\ln[(\xi^{'})^2+(\eta^{'})^2]]/2,\psi=arctg(\xi/\eta)$ in the case of $\Phi(\xi,\eta)=\Phi_{lp}(\xi,\eta)$, and G=R= $[(\xi^{'})^2+(\eta^{'})^2]^{1/2},\psi=arctg(\xi/\eta)$ in the case of $\Phi(\xi,\eta)=\Phi_p(\xi,\eta)$.

After the function H(ψ, G) scanning by the photodetector 6 in columns and rows, the functions H(ψ), H(G) will be formed, carrying information about the features of the input image:

$$H_i(\psi)=\int_0^{L_y}H(\psi,G)l_r dl_r, \tag{22}$$

$$H_j(G) = \int_0^{L_h} H(\psi, G) l_h dl_h \tag{23}$$

where $L_v, L_h$ are the lengths of the horizontal and vertical electrodes.

From expressions (22) and (23) it follows that the function $H(\psi)$ does not depend on G, i.e. is invariant to change the input image scale; the function H(G) is invariant to change the angular orientation of the image. At the output of the photodetector 6, $2n$ signals are generated, which is equivalent to representing the image by a vector **v** of length $DP = 2n$. Thus, the processor output generates a set of electrical signals that characterize the features of the input image.

**4. Conclusions**

Two new types of image transformations are proposed - the Central and Logarithmic Central Image Chord Transformations- CICT and LCICT.

Algorithms for implementing CICT and LCICT operations based on calculating the center of the object, selecting its external binary contour, and constructing chords through the center of this object are presented.

The possibilities of CICT and LCICT operations implementation using software and hardware are considered. The structure of a coherent optical processor for image chord transformation is developed. The possibility of realizing integral operations of CICT and LCICT is presented for contoured and complete images based on the calculation of the autocorrelation function of the object image, which is very promising using parallel optical processors.

It is shown that the CICT operation allows achieving invariance to the displacement and rotation of the object, and the LCICT operation to the displacement, rotation, and scale of the object, which will allow applying high-speed algorithms and techniques at the stage of object classification, significantly reducing the volume of computational operations and to implement a real-time mode in image analysis.

In the future, there will be elaborated the multiprocessor systems for invariant object recognition using proposed operations of image chord transformations CICT and LCICT.

**References**

1. Jin Lin, Qinzhang Yu, Guibin Chen. Infrared ship target detection based on the combination of Bayesian theory and SVM. Proc. SPIE. 11429, MIPPR 2019: Automatic Target Recognition and Navigation.
2. Yi Wu, Chuangang Xu, Ting Li, Keming Yao, Bing Han. A deep learning-based attribute adaptive infrared maritime ship target detection method. Proc. SPIE 11563, Infrared Device and Infrared Technology. (2020) https://doi.org/ 10.1117/ 12.2579752.
3. Garcia-Salgado Beatriz, Ponomaryov Volodymyr, REYES-REYES, Rogelio. Parallel artificial neural networks using wavelet-based features for classification of remote-sensing hyperspectral images. Proc. SPIE 11401, Real-Time Image Processing and Deep Learning (2020), doi: 10.1117/12.2556296.
4. Spiliotis Iraklis, Karampasis Nikolaos Boutalis Yiannis. Fast computation of Hahn moments on gray images using block representation. Journal of Electronic Imaging ,Vol. 29, Issue 1 (Feb 2020).
5. Danyu Sun, Jiangming kan, Songnan Chen. Color-based moment invariants under changing illumination. Journal of Electronic Imaging, Vol. 29, Issue 2 (2020).
6. Akbar Naeem, Tehsin Sara, Rehman Haseebur, Rehman Saad, Young Rupert. Hardware design of correlation filters for target detection. Proc. SPIE 10995, Pattern Recognition and Tracking XXX, (2019); doi: 10.1117/12.2519497.

7. Gardezi A., Malik U., Rehman S., Young R., Birch P., Chatwin C. Enhanced target recognition employing spatial correlation filters and affine scale invariant feature transform. Proc. SPIE 10995, Pattern Recognition and Tracking XXX, (2019); doi: 10.1117/12.2520555.
8. Hoang Thai, Tabbone Salvatore. Invariant pattern recognition using the RFM descriptor. Pattern Recognition, Vol.45, Issue 1, January 2012, Pages 271-284.
9. Guang-Yi Chen, Wen-Fang Xie. Invariant pattern recognition using ring-projection and dual-tree complex wavelets. Proc of ICWAPR International Conference on Wavelet Analysis and Pattern Recognition, 2011, Pages: 182 – 186.
10. Fernández Ariel. Optical architectures for pattern recognition with the generalized Hough transform. Proc. SPIE. 11351, Unconventional Optical Imaging II.
11. Nichol D. Hybrid optical digital computation of global chord functions. Optics Communications, Volume 43, Issue 3, 1 October 1982, Pages 168-170.
12. Casasent D., Chang W. Generalized chord transformation for distortion – invariant optical pattern recognition. Applied Optics, 1983, Vol.21, nr., P.2087-2094.
13. Perju V., Gurau A., Saranciuc D. The optical-electronic pattern recognition system based on the image's logarithmic chord transformation method. In: Optical Pattern Recognition VIII - David P. Casasent, Tien-Hsin Chao, Eds. / Proc SPIE Vol.3073, pp.332-342 (1997). ISBN 9780819424884.

*Journal of Engineering Science* *Vol. XXVIII, no. 1 (2021), pp. 47 - 60*
*Fascicle* *Industrial Engineering* *ISSN 2587-3474*
*Topic* *Applied Engineering Sciences and Management* *eISSN 2587-3482*

**https://doi.org/10.52326/jes.utm.2021.28(1).04**
**UDC 303.7:004.942**

# TOTAL FAVORING IN PROPORTIONAL APPORTIONMENTS

Ion Bolun*, ORCID ID: 0000-0003-1961-7310

*Technical University of Moldova, Stefan cel Mare bd., 168, Chisinau, Moldova*
*Corresponding author: Ion Bolun, *ion.bolun@isa.utm.md*

Received: 01. 28. 2021
Accepted: 02. 21. 2021

**Abstract.** The notion of "*total favoring*" of large or of small beneficiaries in proportional apportionments of entities is defined as a particular case of favoring. It is proven that the number of known conditions of total favoring of beneficiaries in an apportionment (APP) can be considerably reduced. Thus, the volume of calculations to be performed for the respective computer simulation was reduced. In order to quantitatively estimate the total favoring of beneficiaries by APP methods, three indicators were used: the percentage of apportionments, in which large beneficiaries are totally favored; the percentage of apportionments, in which small beneficiaries are totally favored; the percentage of total favoring of large or of small beneficiaries, depending on the APP method applied. A total of five APP methods are being researched: Hamilton (Hare), Sainte-Laguë (Webster), d'Hondt (Jefferson), Huntington-Hill and Adapted Sainte-Laguë. Based on results of computer simulation, the total favoring of beneficiaries by these five APP methods was estimated, including comparatively. For example, it has been identified that the d'Hondt method does not always totally favors beneficiaries to a greater extent than the Huntington-Hill method. At the same time, the Adapted Sainte-Laguë method always totally favors small beneficiaries less compared to the Huntington-Hill method.

**Keywords:** *apportionment method, apportionment problem, comparative analysis, computer simulation, favoring of beneficiaries, quantitative estimate.*

**Rezumat.** Este definită noțiunea de „*favorizare totală*" a beneficiarilor mari sau a celor mici în repartizări proporționale de entități, ca un caz particular de favorizare. Este dovedit că numărul condițiilor cunoscute de favorizare totală a beneficiarilor într-o repartizare (APP) poate fi redus considerabil. Astfel, a fost redus și volumul calculelor de efectuat pentru simularea informatică respectivă. Pentru a estima cantitativ favorizarea totală a beneficiarilor de către metodele APP, s-au folosit trei indicatori: procentajul repartizărilor, în care sunt total favorizați beneficiarii mari; procentajul repartizărilor, în care sunt total favorizați beneficiarii mici; procentajul favorizării totale a beneficiarilor mari sau a celor mici, în funcție de metoda APP aplicată. În total sunt cercetate cinci metode APP: Hamilton (Hare), Sainte-Laguë (Webster), d'Hondt (Jefferson), Huntington-Hill și Sainte-Laguë Adaptată. Pe baza rezultatelor simulării informatice, a fost estimată, inclusiv comparativ, favorizarea totală a beneficiarilor de aceste cinci metode APP. De exemplu, s-a identificat

că nu întotdeauna metoda d'Hondt favorizează total beneficiarii într-o măsură mai mare, decât metoda Huntington-Hill. În același timp, metoda Sainte-Laguë Adaptată întotdeauna favorizează total beneficiarii mici mai puțin, comparativ cu cea Huntington-Hill.

**Cuvinte cheie:** *analiză comparativă, estimare cantitativă, favorizarea beneficiarilor, metodă de repartizare, problemă de repartizare, simulare informatică.*

## 1. Introduction

It is often necessary to distribute a given number *M* of discrete entities of the same kind among *n* beneficiaries, in proportion to a numerical characteristic assigned to each of them $V_i$, $\mathrm{i} = \overline{1,\mathrm{n}}$. This is known as proportional apportionment (APP) problem [1 - 3]. The integer character of this problem usually causes a certain disproportion of the apportionment $x_i$, $i = \overline{1,n}$ [1, 4-6], some beneficiaries being favored at the expense of others. Favoring of beneficiaries leads to the increase of disproportionality and vice versa [6]. Therefore, reducing the favoring in question is one of the basic requirements when is choosing the APP method to be applied under concrete situations (free of bias condition [1, 3]).

As it is well known, the d'Hondt method favors large beneficiaries (with larger $V_i$ value) [1, 4, 6], and Huntington-Hill method favors the small ones (with smaller $V_i$ value) [4, 6]. But which of the two favors beneficiaries to a larger extent? Preferences, in this sense, between methods, can help. Par example, in [7], five APP methods are placed „in the order as they are known to favor larger parties over smaller parties". However, the best way is to estimate this property quantitatively. One approach in this aim is proposed in [8]. Another, a specific one, based on the definition of (total) favoring of large or of small beneficiaries by an apportionment method done in [1], is examined in this paper. Estimates of the frequency of total favoring in apportionments for the widely used Hamilton (Hare), Sainte-Laguë (Webster), d'Hondt (Jefferson), Huntington-Hill and Adapted Sainte-Laguë methods are obtained by computer simulation.

## 2. Essence of favoring of beneficiaries in apportionments

The essence of favoring of beneficiaries in apportionments is described in different papers, including the [4, 9, 10] ones. In [6] they are distinguished three notions of favoring of beneficiaries by an APP method:

a) favoring of a beneficiary in an apportionment;
b) favoring of large or of small beneficiaries in an apportionment;
c) favoring of large or of small beneficiaries overall by an apportionment method.

It is considered that a beneficiary *i* is favored if a larger number $x_i$ of entities is distributed to him than would be due according to the $V_i$ value, more precisely if $x_i > MV_i/V$, where $M = x_1 + x_2 + \ldots + x_n$ and $V = V_1 + V_2 + \ldots + V_n$. Of course, the lack of favoring is possible only if the equalities $\lfloor MV_i/V \rfloor = MV_i/V$, $i = \overline{1,n}$ take place; here $\lfloor z \rfloor$ means the integer part of the real number z. In practice, such equalities rarely occur and that is why some beneficiaries are favored and others, respectively, are disfavored.

In a formalized form, the first, probably, definition of favoring of large or of small beneficiaries in apportionments is done in [1].

**Definition 2** (according to [1, p. 125]). An apportionment method favors large parties if

$$\frac{\sum_{i\in L} x_i}{\sum_{i\in L} V_i} > \frac{\sum_{j\in S} x_j}{\sum_{j\in S} V_j} \quad (1)$$

and it favors small parties if

$$\frac{\sum_{i\in L} x_i}{\sum_{i\in L} V_i} < \frac{\sum_{j\in S} x_j}{\sum_{j\in S} V_j}, \quad (2)$$

where $L$ and $S$ are subsets of {1, 2, ..., $n$} such that $x_i > x_j$ whenever $i \in L$ and $j \in S$ [3].

If, when applying an APP method to any of possible initial data, requirement (1) or, respectively, requirement (2) always occurs, then it can be considered that this method "overall favors" large or, respectively, small beneficiaries (parties). But there are no known such methods that would be used in practice. In such a situation the Definition 2 can be used to identify the favoring of large or of small beneficiaries in particular apportionments.

At the same time, it is considered that d'Hondt method favors large beneficiaries, in sense that more frequently it favors large beneficiaries that it favors the small ones, and Huntington-Hill method favors small beneficiaries, in sense that more frequently it favors small beneficiaries that it favors the large ones in apportionments. Moreover, in one and the same apportionment may be favored some large beneficiaries and some small beneficiaries. The approach proposed in [8] can identify, if such an apportionment favors predominantly large or predominantly small beneficiaries. That's why in this paper the apportionments compliant with requirement (1) are considered "total favoring" large beneficiaries, and the ones compliant with requirement (2) are considered "totally favoring" small beneficiaries. These are particular cases of the "favoring" of beneficiaries – large (predominantly) or small (predominantly) in sense of [8].

Finally, to determine if an APP method totally favors (overall) large beneficiaries or it totally favors (overall) small beneficiaries, it is needed to have apportionments on infinity (sufficient large number) of cases of initial data. If the frequency of total favoring of large beneficiaries is larger than the frequency of total favoring of small beneficiaries, then it is considered that the APP method totally favors (overall) large beneficiaries and vice versa.

## 3. Number of restrictions to check the total favoring in apportionments

The frequency of total favoring of large (small) beneficiaries, on a sufficient large number of cases of initial data, can be determined by computer simulation. To do this, it is important to know how many of different inequalities (1) or, in case of favoring of small beneficiaries, of the (2) ones there are.

Without diminishing the universality of the approach, below it is considered that the $n$ beneficiaries are ordered in non-ascending order of $V_i$, $i = \overline{1,n}$, that is $V_1 > V_2 > V_3 > \ldots > V_n$. In proportional apportionments, if $V_i > V_j$ then $x_i \geqslant x_j$. Let's consider the apportionments for which $x_1 > x_2 > x_3 > \ldots > x_n$. For such an apportionment and $|L| + |S| = n$, there are $n - 1$ variants of different pairs of subsets $L$ and $S$: $L_1 = \{1\}$, $S_1 = \{2, 3, \ldots, n\}$; $L_2 = \{1, 2\}$, $S_2 = \{3, 4, \ldots, n\}$; ...; $L_{n-1} = \{1, 2, 3, \ldots, n-1\}$, $S_{n-1} = \{n\}$. However, if all cases, for which $|L| + |S| \leqslant n$, $L \neq \varnothing$, $S \neq \varnothing$, to be taken into account, then the number $K_n$ of variants of different pairs of subsets $L$ and $S$ is considerably larger than $n - 1$.

*Statement 1*. In general case, the number $K_n$ of variants of different pairs of subsets $L$ and $S$ of {1, 2, ..., $n$}, such that $x_i > x_j$ whenever $i \in L$ and $j \in S$, is determined according to recurrent formula

$$K_n = 2K_{n-1} - K_{n-2} + 2^{n-1} - 1, \; n \geqslant 2, \quad (3)$$

where $K_0 = K_1 = 0$.

Indeed, one has $K_2 = 1$, because the only possible variant is $L = \{1\}$ and $S = \{2\}$. From the other hand, according to (3) takes place $K_2 = 2 \times 0 - 0 + 2^{2-1} - 1 = 1$.▼

Also, $K_3 = 5$, because:

1) for $L = \{1\}$ there are three ($C_2^1 + C_2^2 = 2^2 - 1$) possible variants of $S$, that is {2}, {3} and {2, 3};
2) for $L = \{1, 2\}$ there is one ($C_1^1$) possible variant of $S$, that is {3};
3) for $L = \{2\}$ there is one ($C_1^1$) possible variant of $S$ (as for $K_2$), that is {3}.

From the other hand, according to (3) one has $K_3 = 2 \times 1 - 0 + 2^{3-1} - 1 = 5$.▼

When $n = 4$, takes place $K_4 = 16$, because:

1) for $L = \{1\}$ there are 7 ($C_3^1 + C_3^2 + C_3^3 = 2^3 - 1$) possible variants of $S$, that is {2}, {3}, {4}, {2, 3}, {2, 4}, {3, 4} and {3, 4, 5};
2) for $L = \{1, 2\}$ there are three ($C_2^1 + C_2^2$) possible variant of $S$ (as in case (1) of $K_3$), that is {3}, {4} and {3, 4};
3) for $L = \{1, 2, 3\}$ there is one ($C_1^1$) possible variant of $S$ (as in case (2) of $K_3$), that is {4};
4) for $L = \{2\}$ there are three ($C_2^1 + C_2^2$) possible variants of $S$ (as in case (1) of $K_3$), that is {3}, {4} and {3, 4}.
5) for $L = \{2, 3\}$ there is one ($C_1^1$) possible variant of $S$ (as in case (2) of $K_3$), that is {4};
6) for $L = \{3\}$ there is one ($C_1^1$) possible variant of $S$ (as in case (3) of $K_3$), that is {4}.

So, in cases (2)-(3) and, separately, in cases (4)-(5) of $K_4$, there are the same number of possible variants of $S$ as in cases (1)-(2) of $K_3$. Therefore one has $K_4 = 2^3 - 1 + 2K_3 - K_2 = 7 + 2 \times 5 - 1 = 16$. The same result can be obtained also in the following way. Evidently, in cases of $K_4$, in which subset $L$ begins with beneficiaries from 2 to $3 = n - 1$, there are a summary number of possible variants of $S$ equal to $K_3$. Thus, the value of $K_4$ is larger than that of $K_3$ by the summary number of possible variants of $S$ for cases in which subset $L$ begins with beneficiary 1, that is for cases of subsets {1}, {1, 2} and {1, 2, 3}. For the subset {1} of $K_4$, there are $2^{n-1} - 1 = 2^{3-1} - 1$ possible variants of $S$, and for subsets {1, 2} and {1, 2, 3} of $K_4$ the summary number of possible variants of $S$ is equal to those for subsets {1} and {1, 2} of $K_3$, that is to $K_3 - K_2$. ▼

Similarly, when $n = j$ beneficiaries:

1) for $L = \{1\}$ there are ($C_{j-1}^1 + C_{j-1}^2 + \cdots + C_{j-1}^{j-1} = 2^{j-1} - 1$) possible variants of $S$;
2) in cases, in which subset $L$ begins with beneficiaries from 2 to $j - 1$, there are a summary number of possible variants of $S$ equal to $K_{j-1}$;
3) for subsets {1,2}, {1, 2, 3}, …, {1, 2, …, $j$} of $K_j$, the summary number of possible variants of subset $S$ is equal to those for subsets {1}, {1, 2}, …, {1, 2, …, $j - 1$} of $K_{j-1}$, that is to $K_{j-1} - K_{j-2}$.

Thus, one obtains $K_n = 2^{n-1} - 1 + K_{n-1} + (K_{n-1} - K_{n-2}) = 2K_{n-1} - K_{n-2} + 2^{n-1} - 1$. ■

Data of Table 1 show that $K_n$ value increases rapidly with the increase of $n$, becoming more than 2 mil at $n = 20$ beneficiaries.

*Table 1*

**Some values of $K_n$**

| $n$ | $K_n$ | $n$ | $K_n$ | $n$ | $K_n$ | $n$ | $K_n$ |
|---|---|---|---|---|---|---|---|
| 2 | 1 | 4 | 16 | 7 | 219 | 15 | 65399 |
| 3 | 5 | 5 | 42 | 10 | 1981 | 20 | 2096920 |

For approximate calculations, instead of recurrent formula (3) can be used the following one

$$K_n \approx 2 \times 10^{3n/10},\ n = 7 \div 68,$$

where the absolute value of the relative error doesn't exceed 15%. The relative error is positive decreasing from 14.97% to 0.96% at $n = 7 \div 10$ and negative decreasing from –0.66% to –14.89% at $n = 11 \div 68$.

**4. Redefining the notion of total favoring in apportionments**

The $K_n$ value determined according to (3) can be considerable, especially at large values of $n$. Thus, for computer simulation, it is important to reduce the number of requirements (1) and (2). A solution is done by Statement 2.

*Statement 2*. In case of $x_1 > x_2 > x_3 > \ldots > x_n$, the necessary and sufficient conditions for compliance with all $K_n$ inequalities (1) are the $n - 1$ ones

$$\frac{x_1}{V_1} > \frac{x_2}{V_2} > \cdots > \frac{x_n}{V_n}, \tag{4}$$

and with all the $K_n$ restrictions (2) are the $n - 1$ ones

$$\frac{x_1}{V_1} < \frac{x_2}{V_2} < \cdots < \frac{x_n}{V_n}. \tag{5}$$

Indeed, the necessity of conditions (4) is evident. They belong to the $K_n$ ones and cover all $n(n-1)/2$ variants of pairs $\{L, S\}$ for $|L| = |S| = 1$. At the same time, they establish only $n - 1$ relations for the total of $n$ beneficiaries – the minimal possible number. A similar situation is with the necessity of conditions (5). ▼

Regarding the sufficiency of inequalities (4), let's begin with proving the following inequalities

$$\frac{x_1+x_2}{V_1+V_2} > \frac{x_3}{V_3},\ \ \frac{x_1}{V_1} > \frac{x_2+x_3}{V_2+V_3},\ \ \frac{x_1+x_2}{V_1+V_2} > \frac{x_3+x_4}{V_3+V_4}, \tag{6), (7), (8}$$

Because of $\frac{x_2}{V_2} > \frac{x_3}{V_3}$, for it to take place (6), it is sufficient to prove that

$$\frac{x_1+x_2}{V_1+V_2} > \frac{x_2}{V_2}. \tag{9}$$

Let's consider the equality

$$\frac{x_1+y}{V_1+V_2} = \frac{x_2}{V_2}. \tag{10}$$

From (10) one has $y = (x_2V_1 + x_2V_2 - x_1V_2)/V_2 = x_2V_1/V_2 + x_2 - x_1$. If $x_2 > y$, then based on (9), (10) and $\frac{x_2}{V_2} > \frac{x_3}{V_3}$ the inequality (9) occurs, too. So, if takes place $x_2 > x_2V_1/V_2 + x_2 - x_1$, that is if $x_1/V_1 > x_2/V_2$, then the inequality (9) occurs. But the inequality $x_1/V_1 > x_2/V_2$ takes place, then (9) occurs and therefore (6) occurs, too. Evidently, based on same considerations, take place

$$\frac{x_i+x_j}{V_i+V_j} > \frac{x_r}{V_r}, i = \overline{1, r-2}, j = \overline{i+1, r-1}, r = \overline{3, n}. \tag{11}$$

Also, by induction it is easy to show that occur

$$\frac{\sum_{i \in L} x_i}{\sum_{i \in L} V_i} > \frac{x_r}{V_r}, \tag{12}$$

where $L$ is any subset of {1, 2, ..., $j$}, $j = \overline{1, r-1}$ and $r = \overline{2, n}$. Indeed, noting $x_{1,2} = x_1 + x_2$ and $V_{1,2} = V_1 + V_2$ (one new conventional beneficiary in place of two former ones) and based on (6) one has $x_{1,2}/V_{1,2} > x_3/V_3$ and, following same steps when proving (6), one obtain $\frac{x_{1,2}+x_3}{V_{1,2}+V_3} > \frac{x_r}{V_r}$, $r = \overline{4, n}$, that is $\frac{x_1+x_2+x_3}{V_1+V_2+V_3} > \frac{x_r}{V_r}$, $r = \overline{4, n}$. The same way it is easy to show that take place $\frac{x_i+x_j+x_k}{V_i+V_j+V_k} > \frac{x_r}{V_r}$, $i = \overline{1, r-3}$, $j = \overline{i+1, r-2}$, $k = \overline{j+1, r-1}$, $r = \overline{4, n}$; and so on it occur (12).▾

Now, similarly to reasoning when proving relation (6), because of $\frac{x_1}{V_1} > \frac{x_2}{V_2}$, for it to take place (7), it is sufficient to show that

$$\frac{x_2}{V_2} > \frac{x_2+x_3}{V_2+V_3}. \tag{13}$$

Let's consider the equality

$$\frac{x_2}{V_2} = \frac{z+x_3}{V_2+V_3}. \tag{14}$$

From (14) one has $z = (x_2V_2 + x_2V_3 - x_3V_2)/V_2 = x_2V_3/V_2 + x_2 - x_3$. If $x_2 < z$ then, based on (13), (14) and $\frac{x_1}{V_1} > \frac{x_2}{V_2}$, the inequality (13) occurs, too. So, if takes place $x_2 < x_2V_3/V_2 + x_2 - x_3$, that is if $x_3/V_3 < x_2/V_2$, then the inequality (13) occurs. But the inequality $x_3/V_3 < x_2/V_2$ takes place, then (13) occurs and therefore relation (7) occurs, too.

Similarly to considerations when obtaining (12), it is easy to show that occurs

$$\frac{x_j}{V_j} > \frac{\sum_{i\in S} x_i}{\sum_{i\in S} V_i}, \tag{15}$$

where $j = \overline{1, n-1}$ and $S$ is any subset of {$j$ + 1, 2, ..., $n$}. Indeed, noting $x_{2,3} = x_2 + x_3$ and $V_{2,3} = V_2 + V_3$, based on (7) one has $x_1/V_1 > x_{2,3}/V_{2,3}$ and, following same steps when proving (7) and (12), one obtain $\frac{x_r}{V_r} > \frac{x_{i,j}+x_k}{V_{i,j}+V_k}$, that is $\frac{x_r}{V_r} > \frac{x_i+x_j+x_k}{V_i+V_j+V_k}$ $r = \overline{1, n-3}$, $i = \overline{r+1, n-2}$, $j = \overline{i+1, r-1}$, $k = \overline{j+1, r}$ and so on it occur (15).▾

Finally, with refer to relation (8), based on (9) and (13) one has $\frac{x_1+x_2}{V_1+V_2} > \frac{x_2}{V_2} > \frac{x_2+x_3}{V_2+V_3}$, that is, $\frac{x_1+x_2}{V_1+V_2} > \frac{x_2+x_3}{V_2+V_3}$. In the same way, one has $\frac{x_2+x_3}{V_2+V_3} > \frac{x_3+x_4}{V_3+V_4}$. So, take place $\frac{x_1+x_2}{V_1+V_2} > \frac{x_2+x_3}{V_2+V_3} > \frac{x_3+x_4}{V_3+V_4}$, that is, relation (8) occurs. Generalizing, based on same considerations, occur

$$\frac{x_i+x_j}{V_i+V_j} > \frac{x_r+x_k}{V_r+V_k}, i = \overline{1, n-3}, j = \overline{i+1, n-2}, r = \overline{j+1, n-1}, k = \overline{r+1, n}. \tag{16}$$

Also, based on (4) and (15) one has $x_{1,2}/V_{1,2} > x_3/V_3 > (x_4 + x_5)/(V_4 + V_5)$ and taking into account (16) occurs $\frac{x_{1,2}+x_3}{V_{1,2}+V_3} > \frac{x_4+x_5}{V_4+V_5}$, that is $\frac{x_1+x_2+x_3}{V_1+V_2+V_3} > \frac{x_4+x_5}{V_4+V_5}$. Similarly it is easy to show that relation $\frac{x_1+x_2}{V_1+V_2} > \frac{x_3+x_4+x_5}{V_3+V_4+V_5}$ takes place. Generalizing, based on same considerations and also taking into account relations (12) and (15), occur

$$\frac{\sum_{i\in L} x_i}{\sum_{i\in L} V_i} > \frac{\sum_{j\in S} x_j}{\sum_{j\in S} V_j}, \tag{17}$$

where $L$ is any subset of {1, 2, ..., $r$} and $S$ is any subset of {$r$ + 1, 2, ..., $n$}. Relations (17) are equivalent to the (1) ones for the case of $x_1 > x_2 > x_3 > ... > x_n$. ▾

Similarly as proving the sufficiency of conditions (4) compliance with all $K_n$ inequalities (17), that is with the (1) ones, can be proved the sufficiency of conditions (5) compliance with all $K_n$ inequalities (18)

$$\frac{\sum_{i\in L} x_i}{\sum_{i\in L} v_i} < \frac{\sum_{j\in S} x_j}{\sum_{j\in S} v_j}, \tag{18}$$

where $L$ is any subset of {1, 2, ..., $r$} and $S$ is any subset of {$r$ + 1, 2, ..., $n$}, that is with the (2) ones for the case of $x_1 > x_2 > x_3 > ... > x_n$.■

Based on Statement 2, can be simpler redefined the Definition 2 regarding the total favoring of large/small beneficiaries in an apportionment.

**Definition 3.** In an apportionment, large beneficiaries are totally favored if

$$\frac{x_i}{v_i} > \frac{x_j}{v_j} \tag{19}$$

and small beneficiaries are totally favored if

$$\frac{x_i}{v_i} < \frac{x_j}{v_j} \tag{20}$$

whenever $x_i > x_j$, where $i$ and $j$ take values from the {1, 2, 3, ..., $n$} ones.

Based on Definition 3, can be defined the total favoring of large or of small beneficiaries by an apportionment method overall, on an infinity of apportionments. Evidently, the probability $p_L$ of total favoring of large beneficiaries in an apportionment is determined as

$$p_L = \lim_{N\to\infty} \frac{N_L}{N},$$

where $N$ is the total number of apportionments, and $N_L$ is the number of apportionments compliant with requirements (19). Similarly, the probability $p_S$ of total favoring of small beneficiaries in an apportionment is determined as

$$p_S = \lim_{N\to\infty} \frac{N_S}{N},$$

where $N_S$ is the number of apportionments compliant with requirements (20). At the same time, indicator $p_L$ alone does not determine the total favoring of large beneficiaries by apportionment methods, just as indicator $p_S$ alone does not determine the total favoring of small beneficiaries by apportionment methods. It is well known that, in a particular apportionment, used methods can favor both some large and some small beneficiaries. This is why, when talking about the total favoring of beneficiaries by apportionment methods, it is needed to take into account both indicators: $p_L$ and $p_S$.

**Definition 4.** An apportionment method totally favors large beneficiaries if $p_L > p_S$, totally favors small beneficiaries if $p_L < p_S$ and it is neutral if $p_L = p_S$.

**Definition 5.** The grade of an apportionment method total favoring of large beneficiaries can be determined as $f_L = p_L - p_S$ and that of total favoring of small beneficiaries – as $f_S = p_S - p_L$.

## 5. Total favoring the beneficiaries by apportionment methods

Evidently, the compliance with requirements (19), or the (20) ones, for all $n$ beneficiaries of an apportionment, especially when $n$ is large, is rare. For example, it is sufficient only in one of the $n - 1$ cases to take place $V_j < V_i x_j / x_i$ and requirements (19) are not compliant. To determine, by computer simulation, the apportionment methods total favoring of large or of small beneficiaries, in sense of Definitions 4 and 5, the SIMAP application has been elaborated and respective calculations have been made. The initial data used in calculations are: $M$ = 6, 11, 21, 51, 101, 201, 501; $n$ = 2, 3, 4, 5, 7, 10, 15; $n \leqslant M - 1$; $V = 10^8$; uniform distribution of values $V_i$, $i = \overline{1,n}$; sample size $N = 10^6$. So, one has 45 variants of values for the pair $\{M, n\}$: $4 + 6 + 7 \times 5 = 45$.

Although $N = 10^6$, and not $\infty$, the $P_L \approx 100p_L$, $P_S \approx 100p_S$, $F_L \approx 100f_L$ and $F_S \approx 100f_S$ notations will be used. The values of frequencies $P_L$, $P_S$, $F_L$ and $F_S$ are measured in percentages. So, for example:

- $P_L$(H) is the percentage of apportionments, in which large beneficiaries are totally favored, when applying the Hamilton method;
- $P_S$(HH) is the percentage of apportionments, in which small beneficiaries are totally favored, when applying the Huntington-Hill method;
- $F_L$(d'H) is the percentage of total favoring of large beneficiaries by d'Hondt method, that is the difference between the percentage of apportionments, in which large beneficiaries are totally favored and the one, in which small beneficiaries are totally favored, when applying the d'Hondt method.

Here, it is necessary to mention that, although the Hamilton (H) and Sainte-Laguë (SL) methods are neutral in terms of favoring the beneficiaries [6], that is $F_L$(H) = $F_S$(H) = $F_L$(SL) = $F_S$(SL) = 0, there may still be apportionments, in which large beneficiaries are totally favored, or ones, in which small beneficiaries are totally favored, even applying these methods, but take place $P_L$(H) = $P_S$(H) and $P_L$(SL) = $P_S$(SL). Also, for all apportionment methods at $n$ = 2 and $x_1/V_1 \neq x_2/V_2$, the equality $P_L + P_S = 100\%$ takes place.

### 5.1. Total favoring of beneficiaries by Hamilton method

Because of $P_L$(H) = $P_S$(H), only the percentage of apportionments, in which large beneficiaries are totally favored is examined. The graphs of $P_L$(H) indicators dependence to $M$ and $n$, when using Hamilton method, are shown in Figure 1. One can see that $P_L$(H) little depends on $M$, but is strongly decreasing to $n$. For $11 \leqslant M \leqslant 501$, the $P_L$(H) value (Figure 1 and the results of calculations) belong to the range [17.5%; 18.3%] at $n$ = 3, to the range [3.7%; 5.1%] at $n$ = 4, to the range [0.6%; 1.2%] at $n$ = 5 and is very close to 0% at $n \geqslant 7$. So, along with $n$ = 2, many cases of apportionments with totally favored large (small) beneficiaries are only at $n$ = 3 (17.5÷18.3%) and no so many at $n$ = 4 (3.7÷5.1%).

### 5.2. Total favoring of beneficiaries by Sainte-Laguë method

Because of $P_L$(SL) = $P_S$(SL), only the percentage of apportionments, in which large beneficiaries are totally favored, is examined. The graphs of $P_L$(SL) indicators dependence to $M$ and $n$, when using Sainte-Laguë method, are shown in Figures 2. One can see that $P_L$(SL) little depends on $M$, but it is strongly decreasing to $n$. For $11 \leqslant M \leqslant 501$, the $P_L$(H) value (Figure 2 and the results of calculations) belong to the range [19.1%; 19.5%] at $n$ = 3, to the range [5.0%; 6.3%] at $n$ = 4, to the range [1.1%; 1.8%] at $n$ = 5 and is very close to 0% at $n \geqslant 7$.

### 5.3. Total favoring of beneficiaries by d'Hondt method

The graphs of $P_L$(d'H), $P_S$(d'H) and $F_L$(d'H) indicators dependence to $M$ and $n$, when using d'Hondt method, are shown in Figures 3, 4 and 5, respectively. In all of them, less the case of $M$ = 6, the value of $P_L$(d'H), $P_S$(d'H) and $F_L$(d'H) indicators little depends on $M$, but is strongly decreasing to $n$. In more detail, however, for 11 ⩽ $M$ ⩽ 501, the on $M$ dependence:

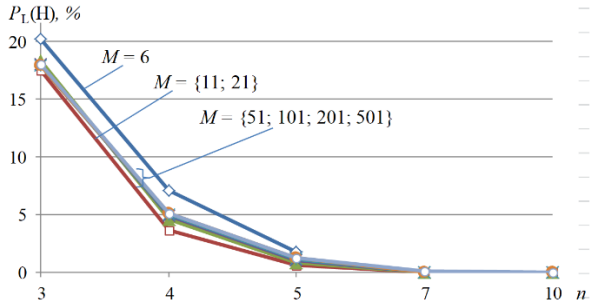


**Figure 1.** The $n$ dependence of the percentage of Hamilton method apportionments, in which the large beneficiaries are favored.

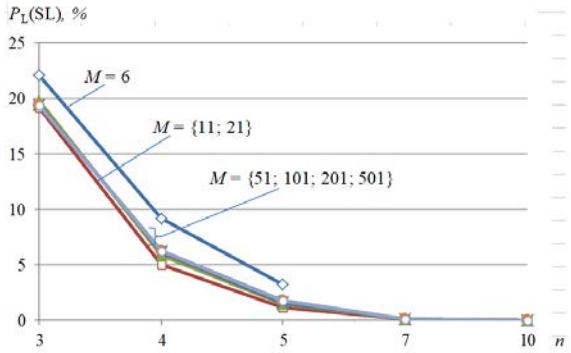


**Figure 2.** The $n$ dependence of the percentage of Sainte-League method apportionments, in which the large beneficiaries are favored.

- of $P_L$(d'H) and $F_L$(d'H) values is decreasing at $n$ = 2 and is increasing at $n$ ⩾ 3;
- of $P_S$(d'H) value, on contrary, is increasing at $n$ = 2 and is decreasing at $n$ ⩾ 3 (except the interval of $M$ = 11÷21 at $n$ = 3, which is increasing);

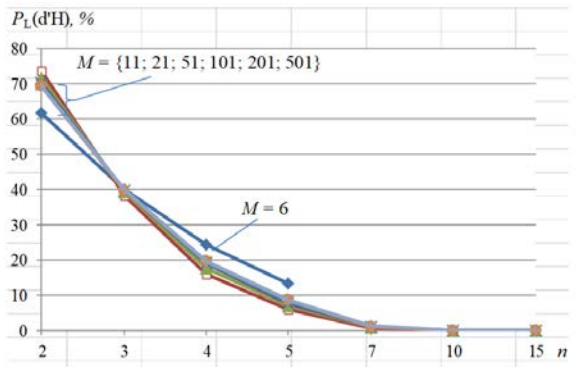


**Figure 3.** The $n$ dependence of the percentage of d'Hondt method apportionments, in which the large beneficiaries are favored.

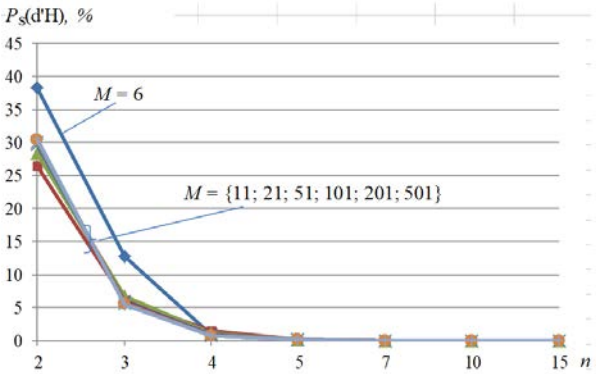


**Figure 4.** The $n$ dependence of the percentage of d'Hondt method apportionments, in which the small beneficiaries are favored.

Thus, for 11 ⩽ $M$ ⩽ 501, the $P_L$(d'H) value (Figure 3 and the results of calculations) belong to the range [69.3%; 73.6%] at $n$ = 2, to the range [38.4%; 39.9%] at $n$ = 3, to the range [16.1%; 19.7%] at $n$ = 4, to the range [5.9%; 8.6%] at $n$ = 5, to the range [0.7%; 1.2%] at $n$ = 7 and is very close to 0% at $n$ ⩾ 10.

For 11 ⩽ $M$ ⩽ 501, the $P_S$(d'H) value (Figure 4 and the results of calculations) belong to the range [26.4%; 30.7%] at $n$ = 2, to the range [5.5%; 6.7%] at $n$ = 3, to the range [0.7%; 1.5%] at $n$ = 4, to the range [0.1%; 0.2%] at $n$ = 5 and is very close to 0% at $n$ ⩾ 7. Also, by comparing data of Figures 3 and 4, one can see that in all examined cases it takes place $P_L$(d'H) > $P_S$(d'H).

Similarly, for 11 ⩽ $M$ ⩽ 501, the $F_L$(d'H) value (Figure 5 and the results of calculations) belong to the range [38.6%; 47.3%] at $n$ = 2, to the range [32.1%; 34.4%] at $n$ = 3, to the range [14.6%; 19.0%] at $n$ = 4, to the range [5.7%; 8.5%] at $n$ = 5, to the range [0.6%; 1.2%] at $n$ = 7 and is very close to 0% at $n$ ⩾ 10. Thus, Figure 5 clearly show that on average the d'Hondt method totally favors large beneficiaries, the percentage of total favoring being considerable at small values of $n$, especially at $n$ ⩽ 5 beneficiaries.

### 5.4. Total favoring of beneficiaries by Huntington-Hill method

The graphs of $P_S$(HH), $P_L$(HH) and $F_S$(HH) indicators dependence to $M$ and $n$, when using Huntington-Hill method, are shown in Figures 6, 7 and 8, respectively.

According to Figures 6 and 7, the on $M$ dependence of the $P_L$(HH) indicator is decreasing and of the $P_S$(HH) indicator is increasing, but the on $n$ dependence are both strongly decreasing. So, for 11 ⩽ $M$ ⩽ 501, the $P_S$(HH) value (Figure 6 and the results of calculations) belong to the range [50.2%; 53.2%] at $n$ = 2, to the range [24.2%; 40.2%] at $n$ = 3, to the range [10.5%; 28.7%] at $n$ = 4, to the range [4.1%; 20.5%] at $n$ = 5, to the range [0.4%; 13.2%] at $n$ = 7, to the range [0.0%; 2.6%] at $n$ = 10, is equal to 0.6% at $M$ = 21, $n$ = 10 and is very close to 0% at {51 ⩽ $M$ ⩽ 501, $n$ ⩾ 10}. For 11 ⩽ $M$ ⩽ 501, the $P_L$(HH) value (Figure 7 and the results of calculations) belong to the range [46.8%; 49.8%] at $n$ = 2, to the range [10.7%; 23.1%] at $n$ = 3, to the range [1.1%; 9.6%] at $n$ = 4, to the range [0.0%; 3.5%] at $n$ = 5, to the range [0.0%; 0.3%] at $n$ = 7 and is very close to 0% at $n$ ⩾ 10.

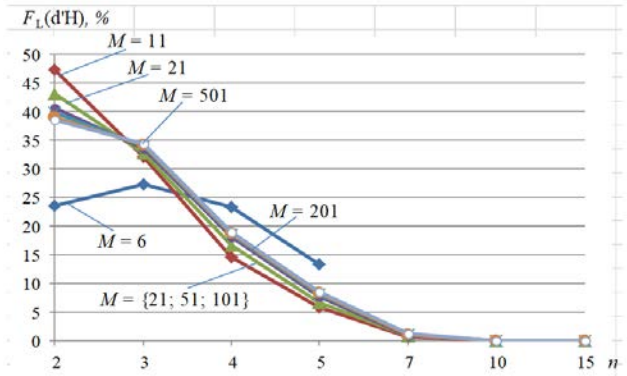


**Figure 5.** The $n$ dependence of the d'Hondt method total favoring of large beneficiaries in apportionments.

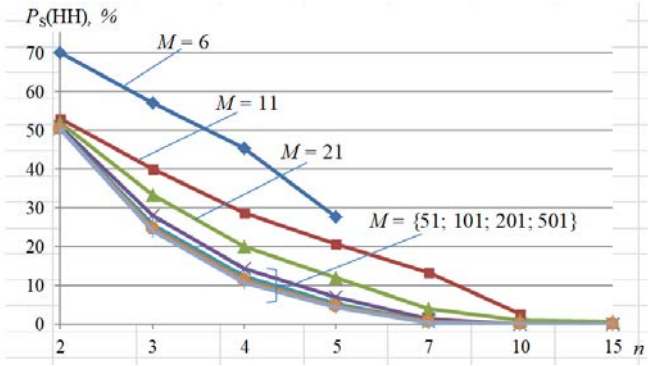


**Figure 6.** The $n$ dependence of the percentage of Huntington-Hill method apportionments, in which the small beneficiaries are favored.

An another situation is regarding the graphs of $F_S$(HH) indicator dependence to $M$ and $n$, when using the Huntington-Hill method.

According to Figure 8, the on $M$ dependence of the $F_S$(HH) is decreasing, but the on $n$ dependence of it is increasing in the range from $n$ = 2 to $n$= 3 and is decreasing for $n$ ⩾ 3.

So, for 11 ⩽ $M$ ⩽ 501, the $F_L$(HH) value (Figure 8 and the results of calculations) belong to the range [0.5%; 6.4%] at $n$ = 2, to the range [1.0%; 29.4%] at $n$ = 3, to the range [1.0%; 27.6%] at $n$ = 4, to the range [0.6%; 20.5%] at $n$ = 5, to the range [0.1%; 13.2%] at $n$ = 7; it is equal to 2,6 at {$M$ = 11, $n$ = 10}, to 0.9% at {$M$ = 21, $n$ = 10}, to 0.6% at {$M$ = 21, $n$ = 15} and is very close to 0% at {51 ⩽ $M$ ⩽ 501, $n$ ⩾ 10}.

Thus, Figure 8 clearly show that on average the Huntington-Hill method totally favors small beneficiaries, the percentage of total favoring being considerable at small values of $n$, especially at $3 \leqslant n \leqslant 5$.

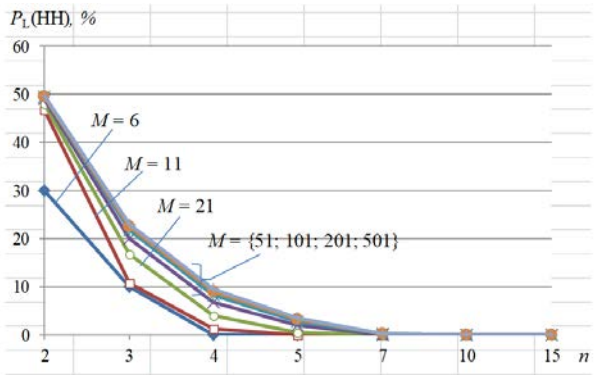


**Figure 7.** The $n$ dependence of the percentage of Huntington-Hill method apportionments, in which the large beneficiaries are favored.

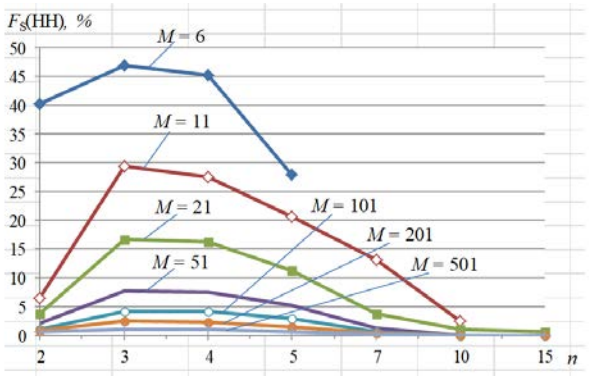


**Figure 8.** The $n$ dependence of the Huntington-Hill method total favoring of small beneficiaries in apportionments.

### 5.5. Total favoring of beneficiaries by Adapted Sainte-Laguë method

The graphs of $F_S$(ASL) indicator dependence to $M$ and $n$, when using Adapted Sainte-Laguë (ASL) method, are shown in Figure 9. If to not take into account the case of $M$ = 6, the on $M$ dependence of $F_S$(HH) is decreasing, but the on $n$ dependence of it is increasing in the range from $n$ = 2 to $n$ = 3 and is decreasing for $n \geqslant 3$.

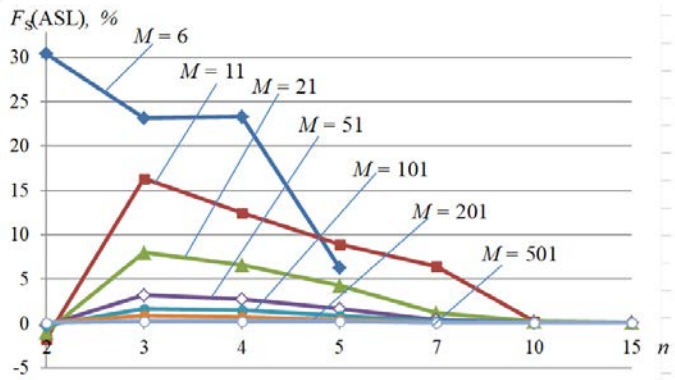


**Figure 9.** The $n$ dependence of the Adapted Sainte-Laguë method total favoring of small beneficiaries in apportionments.

So, for $11 \leqslant M \leqslant 501$, the $F_L$(d'H) value (Figure 9 and the results of calculations) belong to the range [0.3%; 16.3%] at $n$ = 3, to the range [0.3%; 12.5%] at $n$ = 4, to the range [0.2%; 8.9%] at $n$ = 5, to the range [0.0%; 6.4%] at $n$ = 7; it is equal to 0,2 at {$M$ = 11, $n$ = 10}, to 0.3% at {$M$ = 21, $n$ = 10}, to 0.1% at {$M$ = 21, $n$ = 15} and is very close to 0% at {$51 \leqslant M \leqslant 501$, $n \geqslant 10$}.

## 6. Comparative analyses of apportionment methods

As expected, for all examined APP methods, the on $n$ dependence of $P_L(\cdot)$ and $P_S(\cdot)$ indicators are strongly decreasing (see Figures 1 - 4, 6 and 7), while those of $F_L$(d'H) and $F_S$(HH) and $F_S$(ASL) (see Figures 5, 8 and 9) are different – they are increasing for some segments and decreasing for the others. Comparing Figures 1 and 2, one can see the strong similarity of the character of dependences on $M$ and $n$ of indicators $P_L$(H) and $P_L$(SL).

Also, the results of calculations show that occur relations:

1) $P_L(H) = P_S(H) < P_L(SL) = P_S(SL)$;
2) $P_L(d'H) > \max\{P_S(d'H), P_L(H), P_S(H), P_L(SL), P_S(SL), P_L(ASL), P_L(HH)\}$;
3) $P_S(HH) > \max\{P_S(d'H), P_L(H), P_S(H), P_L(SL), P_S(SL), P_S(ASL), P_L(ASL), P_L(HH)\}$;

4) $P_S$(HH) < $P_S$(ASL), at $n$ = 2 and, also, at {$M$ = [6÷11]; $n$ = 3};

5) $P_S$(HH) > $P_S$(ASL), at $n$ = ⩾ 4.

Of course, relations among $F_L$(d'H), $F_S$(HH) and $F_S$(ASL) indicators are the most important. The on $M$ and $n$ dependence of differences $F_L$(d'H) – $F_S$(HH), $F_L$(d'H) – $F_S$(ASL) and $F_S$(HH) – $F_S$(ASL) are shown in Figures 10, 11 and 12, respectively.

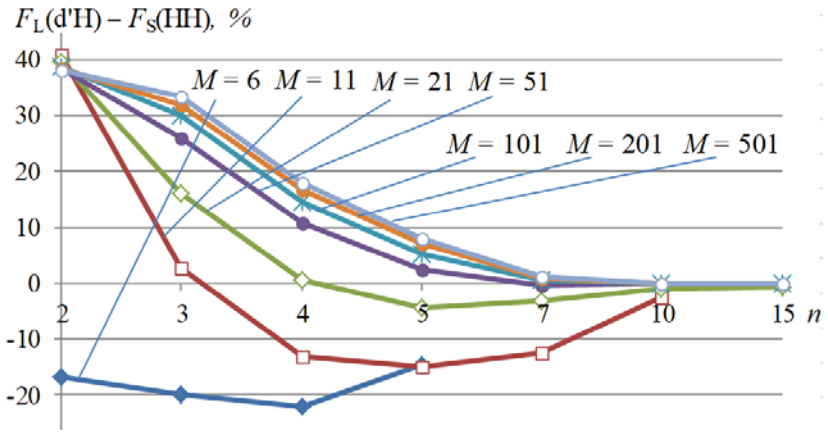


**Figure 10.** The difference $F_L$(d'H)-$F_S$(HH) dependence to $n$.

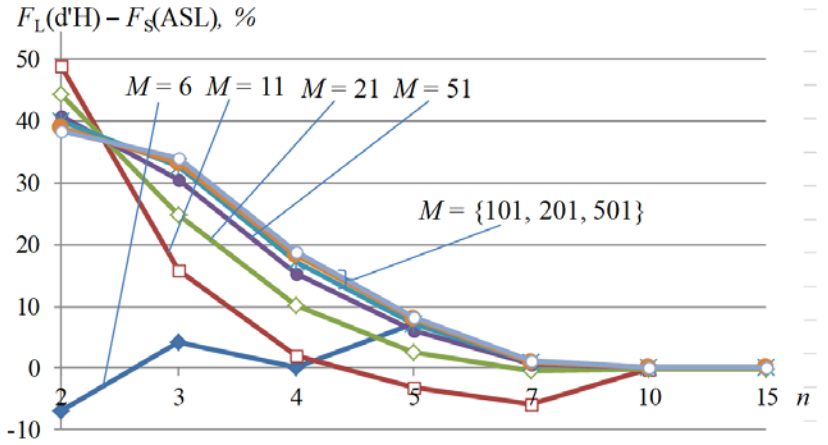


**Figure 11.** The difference $F_L$(d'H)-$F_S$(ASL) dependence to $n$.

Although it is considered that d'Hondt method favors large beneficiaries strongly, and Huntington-Hill method favors small beneficiaries slightly, with refer to total favoring of beneficiaries, in many cases relation $F_L$(d'H) < $F_S$(HH) occur (Figure 10), especially at small values of $M$. Moreover, there are cases when relation $F_L$(d'H) < $F_S$(ASL) takes place, too (Figure 11).

However, mostly, relations $F_L$(d'H) > $F_S$(HH) and $F_L$(d'H) > $F_S$(ASL) occur. At the same time, there are

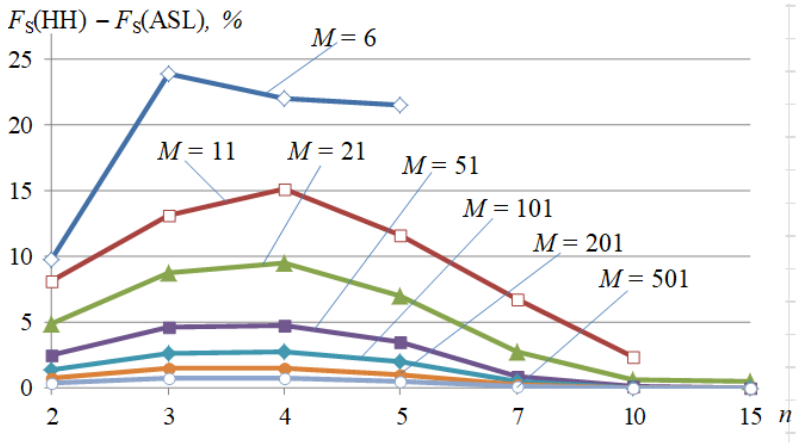


**Figure 12.** The difference $F_S$(HH)-$F_S$(ASL) dependence to $n$.

no alternatives for the difference $F_S$(HH) – $F_S$(ASL) – it is always positive, that is $F_S$(HH) > $F_S$(ASL) (see Figure 12). Thus, Adapted Sainte-Laguë method rarer, than the Huntington-Hill one, implies the total favoring of beneficiaries – of the small ones.

**7. Conclusions**

The conditions of favoring large or small beneficiaries (parties) by an apportionment method defined in [1] (Definition 2) are very strong. There are no known such methods that would be used in practice. But these conditions can be used to identify the favoring of large or of small beneficiaries in particular apportionments. At the same time, in one and the same apportionment may be favored some large beneficiaries and some small ones and, however, predominantly to be favored large or, on the contrary, small beneficiaries. Therefore it is proposed to use two different notions: "favoring" of large or of small beneficiaries and "total favoring" of large or of small beneficiaries, the second one being a particular case of the first. The compliance of an apportionment with conditions (1) or with the (2) ones is referred to "total favoring" of large or, respectively, of small beneficiaries. The larger notion of favoring of large or of small beneficiaries is used when in an apportionment are predominantly favored large or, on the contrary, small beneficiaries in sense of [8].

There has been obtained the formula for determining the number $K_n$ of conditions (1) or (2) for computer simulation. But this number is growing very fast with the growth of the number $n$ of beneficiaries, exceeding 2 mil at $n$ = 20. Fortunately, it was possible to overcome this situation. Thus, the volume of needed calculus for computer simulation was considerably reduced.

In order to estimate quantitatively the total favoring of beneficiaries, three indicators were used: (a) the percentage $P_L(\cdot)$ of apportionments, in which large beneficiaries are totally favored; (b) the percentage $P_S(\cdot)$ of apportionments, in which small beneficiaries are totally favored; (c) the percentage of total favoring of large $F_L(\cdot)$ or of small $F_S(\cdot)$ beneficiaries, depending on the APP method applied. A total of five APP methods are being researched: Hamilton, Sainte-Laguë, d'Hondt, Huntington-Hill and Adapted Sainte-Laguë. The initial data used in calculations are: $M$ = 6, 11, 21, 51, 101, 201, 501; $n$ = 2, 3, 4, 5, 7, 10, 15; $n \leqslant M - 1$; $V = 10^8$; uniform distribution of values $V_i$, $i = \overline{1,n}$; sample size $N = 10^6$.

As expected, for all five methods the on $n$ dependence of indicators $P_L(\cdot)$ and $P_S(\cdot)$ is strongly decreasing, becoming approx. 0 at $n \geqslant 7 \div 10$. With refer to the on $n$ dependence of indicators $F_L$(d'H), $F_S$(HH) and $F_S$(ASL) it is increasing for some of $n$ = 2÷3 segments and is decreasing for the others.

Also, take place the relations:

1) $P_L$(H) = $P_S$(H) < $P_L$(SL) = $P_S$(SL);
2) $P_L$(d'H) > max{$P_S$(d'H), $P_L$(H), $P_S$(H), $P_L$(SL), $P_S$(SL), $P_L$(ASL), $P_L$(HH)};
3) $P_S$(HH) > max{$P_S$(d'H), $P_L$(H), $P_S$(H), $P_L$(SL), $P_S$(SL), $P_S$(ASL), $P_L$(ASL), $P_L$(HH)};
4) $P_S$(HH) < $P_S$(ASL), at $n$ = 2 and, also, at {$M$ = [6÷11]; $n$ = 3};
5) $P_S$(HH) > $P_S$(ASL), at $n = \geqslant 4$.

At the same time, in many cases relation $F_L$(d'H) < $F_S$(HH) occurs, especially at small values of $M$, and in some cases relation $F_L$(d'H) < $F_S$(ASL) takes place. However, mostly, relations $F_L$(d'H) > $F_S$(HH) and $F_L$(d'H) > $F_S$(ASL) occur. So, not for all values of the pare {$M$, $n$} Huntington-Hill and Adapted Sainte-Laguë method ensure less total favoring of small

beneficiaries than d'Hondt method totally favors large beneficiaries. But always $F_S$(HH) > $F_S$(ASL), that is Adapted Sainte-Laguë method rarer, than the Huntington-Hill one, implies the total favoring of small beneficiaries.

**References**


1. Balinski M.L., Young H.P. *Fair Representation: Meeting the Ideal of One Man, One Vote*. 2nd ed. Washington, DC: Brookings Institution Press, 2001.
2. Kohler U., Zeh J. Apportionment methods. *The Stata Journal*, 2012, 12(3), pp. 375–392.
3. Niemeyer H.F., Niemeyer A.C. Apportionment Methods. *Math. Social Sci*., Vol. 56, Issue 2 (2008), pp. 240-253. University of Western Australia, arXiv: 1510.07528v1 [math.HO], Oct. 27, 2015, pp. 1-24. (https://arxiv.org/pdf/1510.07528.pdf, accessed 25.07.2020).
4. Gallagher M. Proportionality, Disproportionality and Electoral Systems. *Electoral Studies*, 1991, 10(1), pp. 33-51.
5. Karpov A. Measurement of disproportionality in proportional representation. *Mathematical and Computer Modeling*, 2008, 48, pp. 1421-1438.
6. Bolun I. Favoring multioptional decisions. *Mathematic modeling, optimization and information technologies*. Proc. of int. sc. conf., March 22-25, 2016. Ed. 5, Vol. I. Chisinau: Evrica, ATIC, 2016. – pp. 35-45. [in Romanian]
7. Marshall A., Olkin I. & Pukelsheim F. A majorization comparison of apportionment methods in proportional representation. *Social Choice Welfare* **19,** 885-900 (2002). (https://doi.org/10.1007/s003550200164, accessed 25.07.2020).
8. Bolun I. A criterion for estimating the favoring of beneficiaries in apportionments. *Proceedings of Workshop on Intelligent Informatition Systems WIIS2020*, December 04-05, 2020. Chisinau: IMI, 2020. – pp. 33-41.
9. Tannenbaum P. *Excursions in Modern Mathematics*, Seventh Edition. Pearson, 2008. – 704 p.
10. Sorescu A., Pirvulescu C. and al. *Electoral systems*. Bucharest: Pro Democratia, 2006. – 54 p. [in Romanian].

*Journal of Engineering Science* *Vol. XXVIII, no. 1 (2021), pp. 61 - 66*
*Fascicle* *Electronics and Computer Science* *ISSN 2587-3474*
*Topic* *Microelectronics and Nanotechnologies* *eISSN 2587-3482*

**https://doi.org/10.52326/jes.utm.2021.28(1).05**
**UDC 621.373.826**

# THE INFLUENCES OF THE ASYMMETRIC GAIN SATURATION EFFECT ON THE DYNAMICS OF InGaAsP FABRY-PEROT LASERS

Veronica Dobrovolschi*, ORCID ID: 0000-0001-8361-9340,
Constantin Pirtac, ORCID ID: 0000-0002-7775-237X,
Vasile Tronciu, ORCID ID: 0000-0002-9164-2249

*Technical University of Moldova, 168, Stefan cel Mare Str.,MD-2004, Chisinau, Republic of Moldova*
*Corresponding author: Veronica Dobrovolschi, *veronica.dobrovolschi@fiz.utm.md*

Received: 12. 22. 2020
Accepted: 02. 03. 2021

**Abstract.** This paper reports on the influence of the asymmetric gain saturation on the dynamics of InGaAsP Fabry-Perot lasers. The results are obtained by numerical simulations of multimode rate equations. The gain saturation effects that results in competition phenomena among lasing modes are investigated. A hopping multimode case is examined in detail. With means of the bifurcation analysis the regions with instabilities in the evolution of the mode intensities have been found. The following operation in the plane of two parameters are obtained: stable single mode, stable multimode, bistabile, and multimode hopping. The pulse traces of amplitudes of modes are plotted to illustrate the observed behaviors. Finally, the influence of linewidth enhancement Henry factor on the laser behavior is investigated.

**Keywords:** *Mode hopping, InGaAsP lasers, multimode operation, Henry factor.*

## Introduction

During recent yeas InGaAsP semiconductor lasers received considerable attention due to their applications as coherent sources for optical communications. Under appropriate conditions such lasers exhibit the stable single mode operations. On the other hand, when considering saturation coefficients the laser displays several types of nonlinear effects [1 - 3]. Mode hopping is directly correlated to the noise in the total optical intensity. There are combinations of laser case temperature and injection current that lead to mode hopping and others for which the laser is stable. Recording such noise characteristics of laser diode has implications for controlling and circumventing mode hopping effects [4]. the overall intensity noise dynamics of InGaN edge emitting lasers was reported in [5]. Mode clustering usually observed in InGaN lasers enhances the mode competition and then the laser intensity fluctuation. Variations as large as 20 dB have been observed. The coexistence of longitudinal modes induces mode competition and then unstable bimodal lasing. This mode competition is mediated by the temporal fluctuations of spontaneous emission through the nonlinear cross saturation of the optical gain [5]. Comprehensive investigation of noise characteristics and radiation spectrum with special attention to the

mode-hopping effect of Fabry–Pérot multiple quantum well laser diodes have been carried out [6]. Cross-correlation factor between them have been measured under stable and mode-hopping operation. At the mode-hopping that occurs at particular operation conditions (injection current and temperature) laser diode radiation spectrum is unstable in time [6]. A time-resolved study is presented in [7] of the single-mode and mode-switching dynamics observed in swept source vertical cavity surfing emitting lasers and swept wavelength short external cavity lasers. More complex mode-switching behaviour occurs in the external cavity laser, with the mode-hopping dynamics found to be dominated by the deterministic movement of the spectral filter.

Recently, a comparative analysis of static and dynamic measurements, on the impact of mode hopping on the overall intensity noise dynamics of InGaN edge emitting lasers is reported in [8]. The mode competition is mediated by temporal fluctuations of spontaneous emission through nonlinear cross saturation of the optical gain. In [9] a report on coherent measurements of the ultrafast dynamics, mode competition and frequency selection in a frequency-tuneable laser is presented. The used approach allows to observe hopping between lasing modes on picosecond-timescales. The physics is explained through a full multi-mode, temperature-dependent carrier and photon transport model.

This paper is concerned with investigations of the influence of asymmetric cross saturation gain on the FP laser dynamics. We report the bifurcation analysis with for the case of of multimode operation of InGaAsP semiconductor lasers. In Section 2 we introduce the setup, and an appropriate model to describe it. Section 3 presents a study of the multimode dynamics of laser and control of its operation. Finally, conclusion are given in Section 4.

**Laser structure and equations**

A sketch of the investigated InGaAsP laser is shown in Fig. 1. It consist of an 300 μm active section pumped by an injected current $I$. $R_f$ and $R_b$ are the reflectivity of the air-material front facet and the outer facet of the material cavity, respectively. Front facet reflectivity $R_f$ is 20% and back facet reflectivity $R_b$ is 70%. The width of active region is 0.3 μm, and the thickness is 0.1 μm. We consider the multimode laser operation. We assume that an injected current $I$ is injected into the active region.

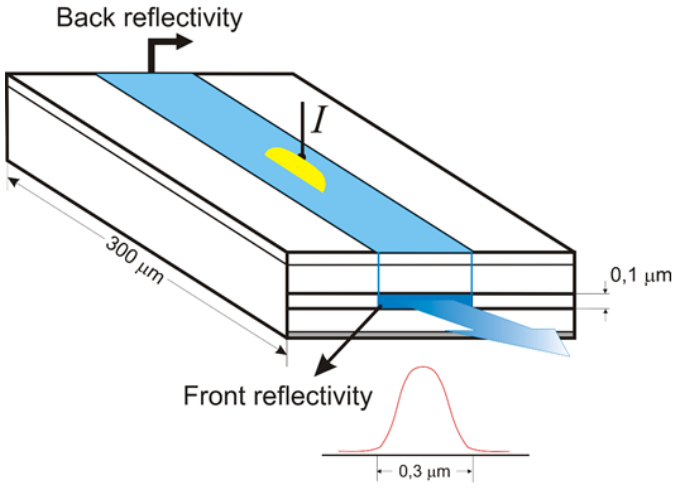


**Figure 1.** Setup of InGaAsP Fabry-Perot lasers.

The laser dynamics is analyzed using multimode rate equations of the photon number $S_p$ and the injected carrier number $N$

$$\frac{dS_p}{dt} = (A_p - BS_p - \sum_q D_{p(q)} S_q - G_{th}) S_p + \frac{a\xi}{V} N \,, \tag{1}$$

$$\frac{dN}{dt} = -\sum_q A_p S_p - \frac{N}{\tau_s} + \frac{I}{e} \,, \tag{2}$$

where *p* is the mode number (*p* = ±1,±2...). We mention that in our calculations we consider 9 modes. The mode *p*=0 with wavelength $\lambda_0$ is the central mode. $A_p$ is liniar gain coefficient with the following form

$$A_p = \frac{a\xi}{V}\left[(N - N_g) - b(\lambda_p - \lambda_0)^2\right] \tag{3}$$

where $N_g$ is the carrier number at the transparency. *V* is the laser volume. *a* is the slope of the local linear gain, and *b* is a coefficient giving the wavelength dispersion of the linear gain. ξ is the field confinement factor of the active region.

In (1) *B* and *D* represents the gain saturation coefficients

$$B = B_0(N - N_g) \qquad \text{and} \qquad D_{p(q)} = \frac{4}{3}B + \frac{H_c(N - N_g)}{\lambda_q - \lambda_p}\ , \tag{4}$$

where, $H_C$ is linewidth enhancement factor [10].

The threshold gain level is given by expression

$$G_{th} = \frac{c}{n_r}\left[k + \frac{1}{2L}\ln\frac{1}{R_f R_b}\right], \tag{5}$$

where $R_f$ and $R_b$ are the front and back facets power reflectivity, respectively. L is the laser length. $n_r$ is the refractive index. κ is the loss coefficient that includes internal and mirrors losses.

The following set of parameters we use in the numerical calculations $a = 2.7\cdot10^{-12}$ $\mathrm{m^3s^{-1}}$, $\xi = 0.2$, $L = 2.77\cdot10^{-4}$ m, $N_g = 2.35\cdot10^{-8}$, $B_0 = 7.2\cdot10^{-5}$, $\tau_s = 2.79\cdot10^{-9}$ s, $\lambda_0 = 785$ nm, $\Delta\lambda = 0.31$ nm.

**Results and discussions**

In this section we discuss the behavior of semiconductor laser shown in Fig. 1 using the equations (1)-(5). Figure 2 illustrates the dependence of photon number *S* on injected current calculated for nine modes after threshold current. For low current the central mode is dominant (see black line in Fig. 2).

An increase of injected current leads to mode hopping and the mode +1 (red line) become dominant. A further increase of injected current results in another hopping to mode +2. The next hoping takes place at current 0.125 mA where the mode +3 is dominant. Finally, for higher currents the mode +4 is dominant.

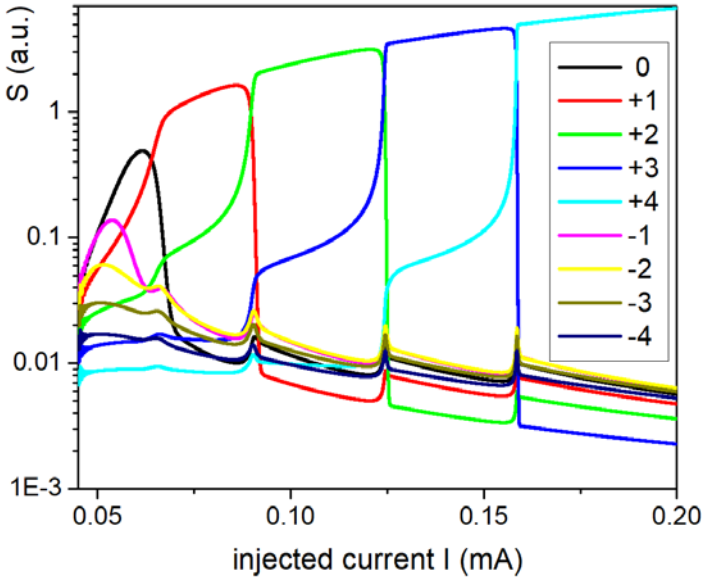


**Figure 2.** Photon number *S* in the dependence of injected current I.

Figure 3 shows time traces of all nine modes for different regions of Figure 2. First we consider the case of currents where the mode +1 is dominant. Figure 3a confirms by pulse traces that certainly this mode is dominant (red line). One can see that in this case the injected current is chosen just after hoping since the mode 0 is located in the near vicinity to mode +1. Figure 3b shows other hoping in time between mode +2 to +3. After 3 ns the mode +3 become dominant and one can see tin this case the single mode operation since the other modes has the lower photon number S. Finally, Figure 3c shows a strong sinle mode operation of mode +4 for high injected currents.

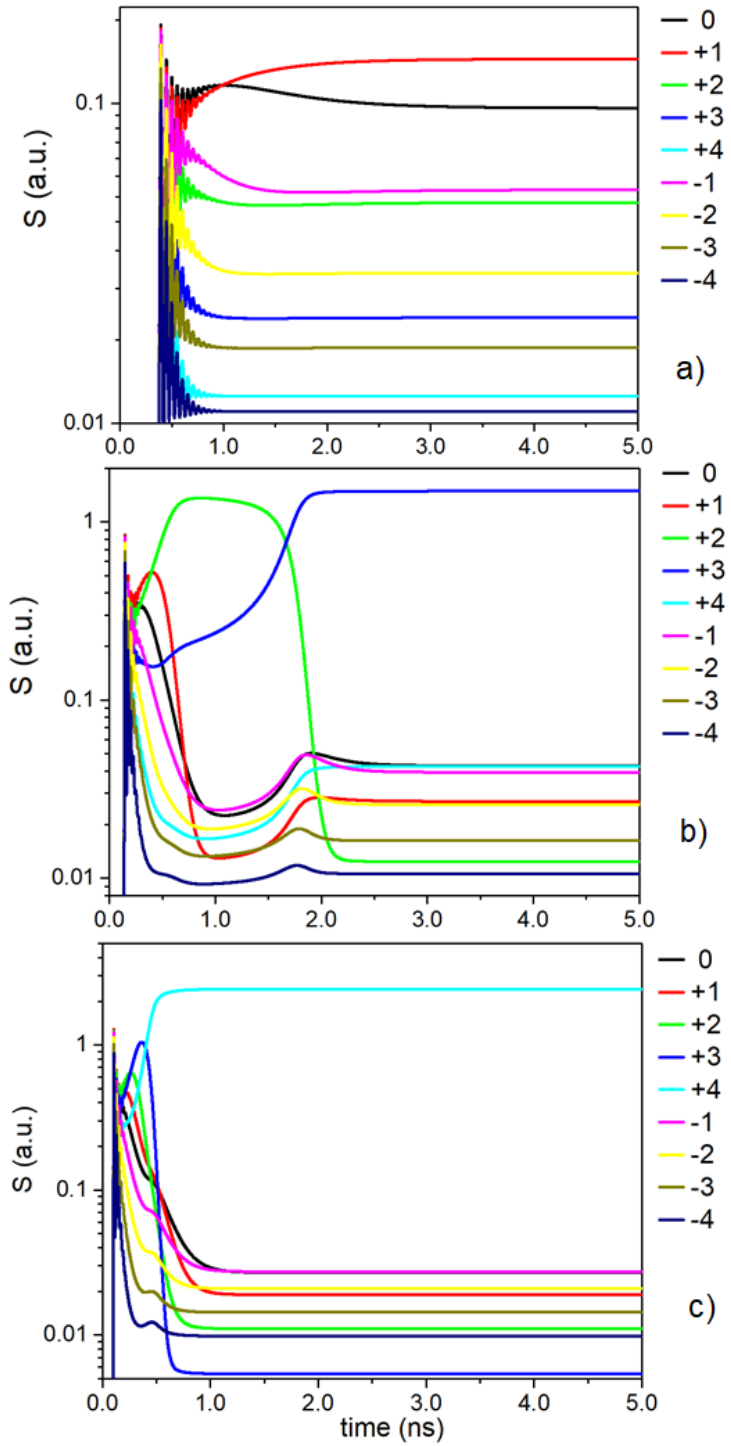


**Figure 3.** The time evolution of total output number *S*.

In what follows we show in Figure 4 the classifications of possible states of laser operations in the plane of two parameters $H_c$-$I/I_{th}$. For small values of parameter *H*c the single mode dominates the operation of laser. When *H*c is increased the bistable phenomena is present in the laser.The bistability is realized between modes +1,+2 and +3. For higher *H*c the laser shows two regions multimode hoping. Finally, for both higher values of injected current and *H*c the single mode of mode +4 is observed. This is confirmed also by Figure 3c.

Figure 5 shows multimode operation of laser that correspond to region of "multimode CW" of Fig. 4. The figure indicates that the modes display a quasiperiodic evolution in time. There is no any dominant modes. We only mention that, the photon number of some modes (0,+1,+2+3) are higher that of others.

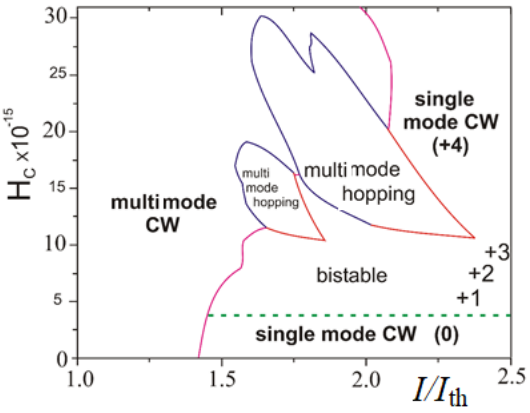


**Figure 4.** Regions of different laser behavior in the plane of two parameters.

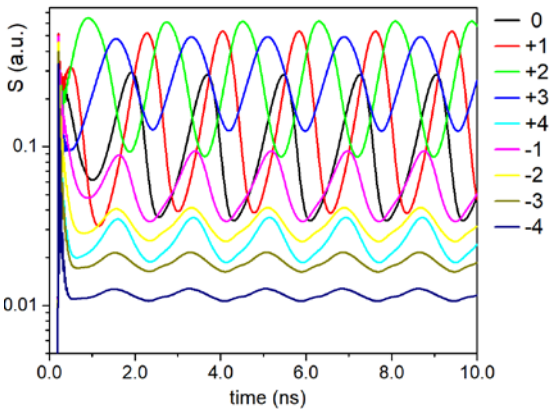


**Figure 5.** Multimode operation.

## Conclusions

We have studied the mode hopping dynamics of multimode InGaAsP Fabry-Perot lasers composed by a single cavity. The laser operation is classified into stable single mode, stable multimode, hopping multimode and bistable. We have shown that the dynamics of such lasers strongly depend on asymmetric cross saturation gain. Operation of InGaAsP lasers at high currents is characterized by rotation of the lasing mode among several long wavelength modes. Finally, we found that the InGaAsP lasers exhibit stable single mode operation under high currents. We believe that our work provides a good basis for future study and, in particular, provides some pointers for more detailed investigations of dynamics of multimode InGaAsP lasers and their control in different applications.

**Acknowledgments.** This work was supported by project **20.80009.5007.08** "Study of optoelectronic structures and thermoelectric devices with high efficiency".

References

1. Yamada M. Theoretical analysis of nonlinear optical phenomena taking into account the beating vibration of the electron density in semiconductor lasers. In: *Journal of Applied Physics,* 66, *1989,* pp. 81–89.
2. Ahmed M., Yamada, M. Influence of instantaneous mode competition on the dynamics of semiconductor lasers. In: *IEEE Journal of quantum electronics*, 38 (6), 2002, pp. 682 – 693.
3. Ahmed M. Numerical characterization of intensity and frequency fluctuations associated with mode hopping and single-mode jittering in semiconductor lasers. In: *Physica D*, 176, 2003, pp. 212–236.
4. Acsente T. Laser diode intensity noise induced by mode hopping. In: *Romanian Reports in Physics*, 59 (1), 2007, pp. 87–92.

5. Congar A., Hussain K., Pareige C., Butte R., Grandjean N., Besnard P., Trbaol S. Impact of mode-hopping noise on *InGaN* edge emitting laser relative intensity noise properties. In: *IEEE Journal of quantum electronics*, 54(1), 2008, pp. 1-7.
6. Pralgauskaite S., Palenskis V., Matukas J., Saulys B. Analysis of mode-hopping effect in Fabry–Pérot multiple-quantum well laser diodes via low frequency noise investigation. In: *Solid-State Electronics*, 79, 2013, pp. 104-110.
7. Butler T.P., Goulding D., Kelleher O, Shaughnessy B., Slepneva S., Hegarty S.P., Huet G. Direct experimental measurement of single-mode and mode-hopping dynamics in frequency swept lasers. In: *Optics Express*, 25 (22), 2017, pp. 27464-27474.
8. Congar A. *et al*., Impact of Mode-Hopping Noise on InGaN Edge Emitting Laser Relative Intensity Noise Properties, *IEEE Journal of Quantum Electronics*, 54 (1), 2018 pp. 1-7. doi: 10.1109/JQE.2017.2774358
9. Kundu I. et al Ultrafast switch-on dynamics of frequency-tuneable semiconductor lasers. *Nature Communication* 9, 2018, p 3076, doi.org/10.1038/s41467-018-05601-x
10. Henry C. Phase noise in injection lasers. In: *Journal lightwave technology*, 4 (3), 1986, pp. 298–311.

*Journal of Engineering Science* *Vol. XXVIII, no. 1 (2021), pp. 67 - 74*
*Fascicle* *Electronics and Computer Science* *ISSN 2587-3474*
*Topic* *Electronics and Communication* *eISSN 2587-3482*

**https://doi.org/10.52326/jes.utm.2021.28(1).06**
**UDC 681.586:004.735]:63**

# A REVIEW OF WIRELESS SENSOR NETWORK POTENTIAL IN NIGERIA AS A TOOL FOR SUSTAINABLE DEVELOPMENT

Ajibola Oyedeji, ORCID: 0000-0002-0180-492X

*Department of Computer Engineering, Olabisi Onabanjo University, Ago-Iwoye, Nigeria*
*Corresponding author: Ajibola Oyedeji, *oyedeji.ajibola@oouagoiwoye.edu.ng*

Received: 10. 19. 2020
Accepted: 01. 22. 2021

**Abstract.** The emerging trend in the world of technology and Information Technology has posed so many opportunities and challenges. Wireless Sensor Network (WSN) is a relatively new and rapidly developing technology due to the advancement and development of the micro-electro-mechanical systems (MEMS) technology. The application areas of wireless sensor and wireless sensor network in the society as tools towards achieving sustainable development range from the health sector through the use of Wireless Body Area Networks (WBANs) to a safer, cleaner and healthier environment. This paper highlights and discusses the potentials of wireless sensor network technology in realizing sustainable development in our society, Nigeria as a case study. WSNs can be employed to improve access to quality health services, increased food production through precision agriculture to a better quality of human resources.

**Keywords:** *sensors, WBAN, sustainable development, precision agriculture.*

## Introduction

Nigeria has one of the largest stocks of human resources with a population of around 180 million people and in spite of the country's vast resources (human and natural), the majority of the citizens are living below the standard according to UNICEF report of 2018. Nigeria is ranked low in the world's living standard report as shown in Figure 1 below. It is therefore imperative and essential to study ways to improve the standard of living and there is a great opportunity to achieve this with the advancement in technology. In spite of the vast landmass and human capital available at its disposal, Nigeria's agricultural sector is well short of meeting the demand of the nation thereby resulting in large importation of cash crops as illustrated in Figure 1 [1].

Achieving sustainable development has become a goal in present-day society especially in a developing country with an emerging economy like Nigeria's. The Sustainable Development Goals (SDGs) document is a universal policy framework which consists of various targeted results that include the following:

Zero hunger
Good health and well-being
Clean water and sanitation
Industry, innovation and infrastructure.

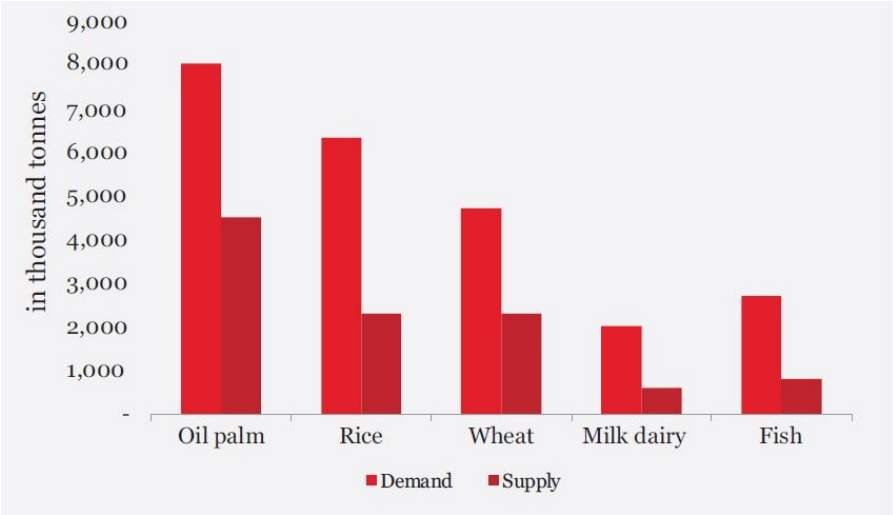


**Figure 1.** Nigeria's demand and supply gap for key agricultural products (2016) [1].

Information Technology (IT) has been at the forefront of driving development from education to public health, agriculture and environmental management. Wireless Sensor Networks (WSNs) possess capabilities to achieve the improved status of life in the world. In a bid to achieve desired results of the SDGs, this work looks into the potentials of WSNs into fulfilling some of the set goals.

Recent development in micro-electro-mechanical systems (MEMS) technology has been the bedrock for the development of minute low-powered, low-cost and low memory sensor nodes that have small transmission range capabilities [2]. These sensor nodes have capabilities for sensing, processing (such as for data aggregation), data storage and for packet transmission across the network to an external powerful computer for further data analysis and storage. The multi-functionality of the sensor nodes has brought about a rapidly emerging and evolving technology called Wireless Sensor Network [3].

WSN includes a large number of the sensor nodes which have been heavily deployed in the desired area or phenomenon for collecting desired data of interest and transmitting the sensed data to the base station as illustrated in Figure 2.

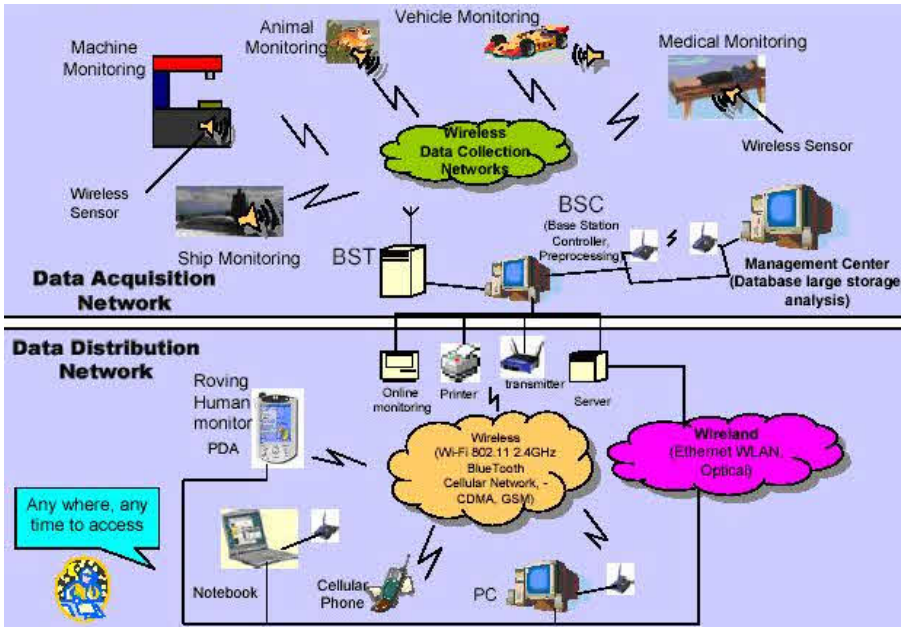


**Figure 2.** Wireless sensor network.

WSN is a self-organizing network that can adapt to network topology changes caused by the death of sensor nodes [4]. The most significant advantages of using WSNs, besides low-cost are related to their self-organizing abilities and versatility of sensors. They are deployed for different applications ranging from weather, industrial process and environmental monitoring to military applications, public health and agriculture [5, 6]. A sensor generally always consists of a transceiver (transmitter and receiver), a processor for basic data aggregation, low-memory unit, and power unit, with optional units such as GPS, mobility.

With Nigeria declared as a developing nation and its technology fast-growing, it is therefore very important and useful to study the state of the WSN technology in Nigeria and its various uncharted potentials. This paper aims to study the various potentials of WSN and ways to apply them to achieve sustainable development in Nigeria.

**Wireless Sensor Network Potentials in Nigeria**

WSNs have capabilities for observing and measuring various physical phenomena in the environment. WSNs can be utilized in Nigeria in diverse areas to improve access to health care, improving food production and processing, the security of life and properties. WSNs are capable of measuring diverse phenomena such as contaminant levels in the water, pollutants in the air, and the flow of water for irrigation. Figure 3 illustrates the various application areas of WSN varying from health care to agriculture, transportation, environmental monitoring and security or surveillance. A wearable WSN for indoor environmental monitoring to measure and monitor the concentration of $CO_2$ was designed in [2].

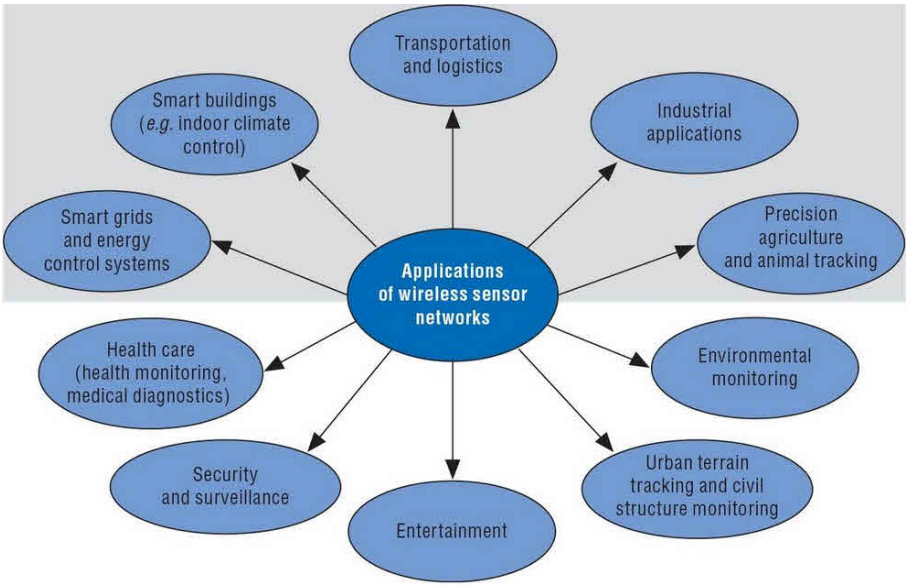


**Figure 3.** Applications of wireless sensor network.

***Health Care***

The health sector is one of the vital sectors to be considered in a developing economy. The health sector in any economy forms the backbone of its growth and development. Nigeria's health sector is epileptic one of the poorest in the world with Nigeria ranked 187 out of 191 countries in world health systems as reported according to the World Health Organization's analysis result of the world's health system in 2017. Factors affecting the overall Nigerian health system performance include: inadequate

health facilities and structures, poor management of human resources, poor motivation and remuneration, inequitable and unsustainable health care financing, skewed economic and political relations, corruption, illiteracy, decreased government spending on health, high user fees, absence of integrated system for disease prevention, surveillance and treatment, inadequate access to healthcare, shortage of essential drugs and supplies and inadequate health care providers [7].

In the health care sector, wireless sensor networks have various application potentials in Nigeria ranging from bedside monitoring to medical diagnostics that can be used to effectively improve the health care delivery. Application of wireless sensor networks in the health sector has made provision of medical services more efficient which in turn has contributed to the development of the countries of use. There is a dire shortage of health workers in Nigeria as a result of economic and social brain drain and has been estimated that the physician to patient ratio stands at about 27: 100,000 is very low in Nigeria and this can be augmented with the use of WSNs which can help reduce the pressure on medical practitioners [8]. WSN can be applied in the health sector for remote monitoring and telemedicine which will, in turn, reduce the pressure and demand on the limited facilities and physicians available.

*Health Monitoring:* WSNs are used to monitor patients in hospitals or at home. The WSNs sensors are used to measure, monitor and record the patient's data such as blood pressure, heart rate, temperature and other vital data. The application of WSNs for patient monitoring offers some advantages over the wired systems like the ease of use, reduced risk of infections, reduced risk of failures, enhanced mobility and lower the cost of delivery [9].
From Figure 4 above, the wireless sensors acquire data from the patient ranging from the heartbeat to the blood pressure and necessary data, this data is then transmitted to the medical server of the hospital where the physician accesses it, assesses and prescribes necessary treatments and monitor how the patient is responding to the treatment administered.

*Wireless Body Area Networks (WBAN):* This is the design of wearable devices using wireless sensors which are wirelessly connected. The WBAN is also used to monitor patients, that is, it is capable of alerting the doctor of any irregularities about the patients like heart attack, high blood pressure and so on. It also helps people by providing healthcare services such as memory enhancement, medical data access, cancer detection, asthma detection, and monitoring blood glucose [4].

*Telemedicine:* With the Nigeria population, with a reasonable percentage of this population living in remote rural areas where

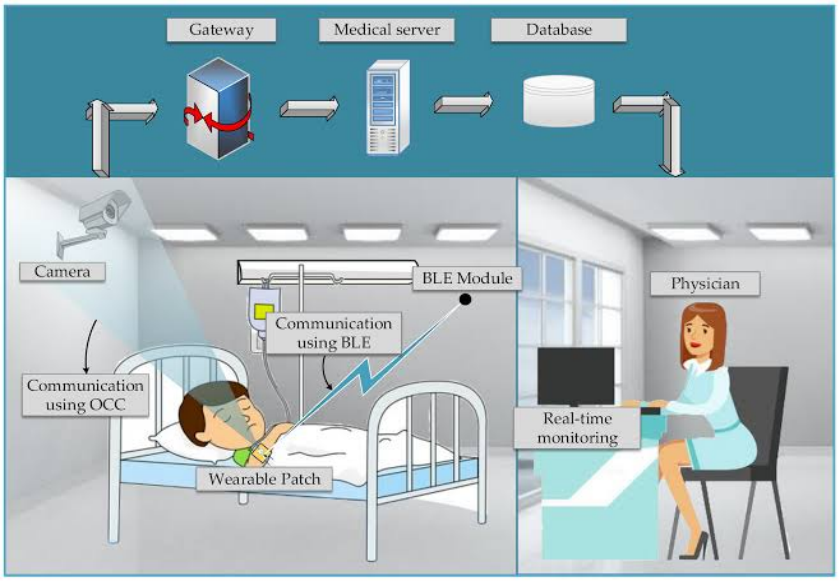


**Figure 4.** Patient monitoring system using WSN.

there is little or no access to basic health care facilities, telemedicine has been proposed as another way of improving the health sector and quality health care delivery. Telemedicine is defined as the delivery of health care and the sharing of medical knowledge over a long distance using telecommunication means [3]. This helps in providing quality health care delivery and education to remote areas and also helps lower the cost of health care which in turn enables sustainable development. A typical telemedicine system is shown in Figure 5 below.

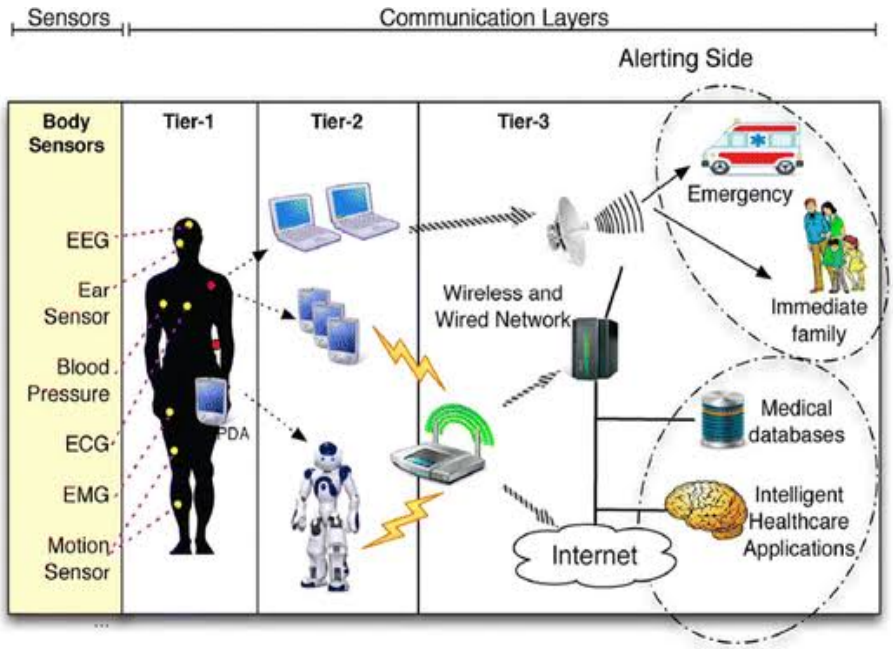


**Figure 5.** Telemedicine system utilizing WSN.

***Agriculture***

With the country faced with the challenges of the falling oil price and the need for diversification, agriculture is a viable alternative to oil. This is because the agricultural sector used to be the major source of revenue to the country through the export of agricultural produce like cocoa before the discovery of oil, even at that, the agricultural sector is said to contribute about 40% to the country's GDP despite its low productivity. Therefore to improve the low productivity in the agricultural sector, modern technologies need to be adopted. Modern technologies like precision farming using WSN has been identified as one of the ways out [10].

Wireless sensor networks have various applications in the agricultural sector, some of which include animal tracking and monitoring system, monitoring the soil condition at different times. With the growing population of the world which has led to an increase in the demand for food and other agricultural produce. To meet the unending demand, various techniques have been proposed to make cultivation and other agricultural practices easier. Some of the techniques proposed are precision agriculture, remote sensor, fire detection, etc. These techniques make use of a wireless sensor network to improve productivity for sustainable development.

Precision Agriculture (PA) is a production system that promotes variable management practices within a field, according to site conditions.

This system is based on new tools and sources of information provided by modern technologies.

These include the global positioning system (GPS), geographic information systems (GIS), yield monitoring devices, soil, plant and pest sensors, remote sensing, and variable-rate technologies for applicators of inputs. Precision agriculture is one of the top ten revolutions in agriculture. Precision agriculture enables farmers to be able to monitor the soil temperature, humidity, etc. and the farmers are provided with an application which can be used to activate different functions like irrigating (drip irrigation) when the soil is dry and others. Precision agriculture is the future of agriculture because of the ease of use [11].

The precision agriculture cycle consists of the following stages as illustrated in Figure 6; measurement of within-field spatially variable soil and crop parameters and monitoring of local weather conditions (data collection), mapping of within-field soil and crop parameters (data collection), mapping of spatially variable rate crop input applications (interpretation), spatially variable rate crop input applications (application).

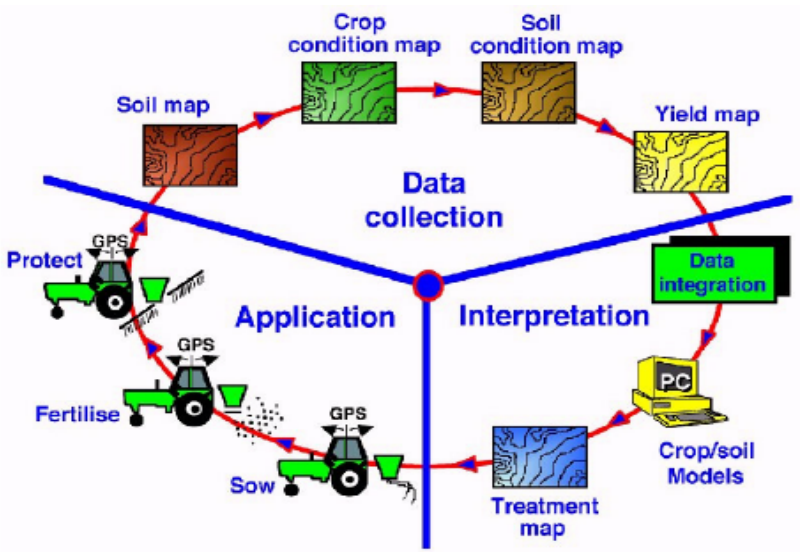


**Figure 6.** Precision agriculture cycle.

The use of precision agricultural practices has resulted in reduced cost of recurrent expenditure as it optimizes the resources been used. There is a considerable ongoing effort in collecting remote sensing data at multiple times to conduct near real-time soil, crop and pest management. PA uses the various measurements gathered to optimize the amount of fertilizer, water, soil nutrients and pesticides and herbicides to be utilized thereby removing their under-application or over-application [12].

***Water Quality Monitoring***

Water is very important to creatures as healthy and clean water is important to man sustaining life because of its numerous applications from cooking, drinking to personal hygiene, etc. Water is also needed in agriculture and industries. The importance of water to man cannot be overemphasized, that is why the provision of clean and healthy water for the populace is of great importance. The statistics of water-borne diseases in Nigeria is worrisome because of the inadequate supply of quality water while some of her citizens who live in remote areas don't even have access to the quality water supply at all. This is as a result of dilapidated water infrastructures and negligence on the side of the government in monitoring the quality of water sold in the country.

As an example of a potential application, consider the incessant incidents of contamination spilling into different rivers in Nigeria, which serve as the main source of drinking water for many people especially in the rural areas. Determining the rate of flow and sometimes the direction of the river requires coordination of multiple sampling points. Sensors periodically taking samples at multiple locations along the river could determine the rate, quantity, and direction of contaminant flow as shown in Figure 7.

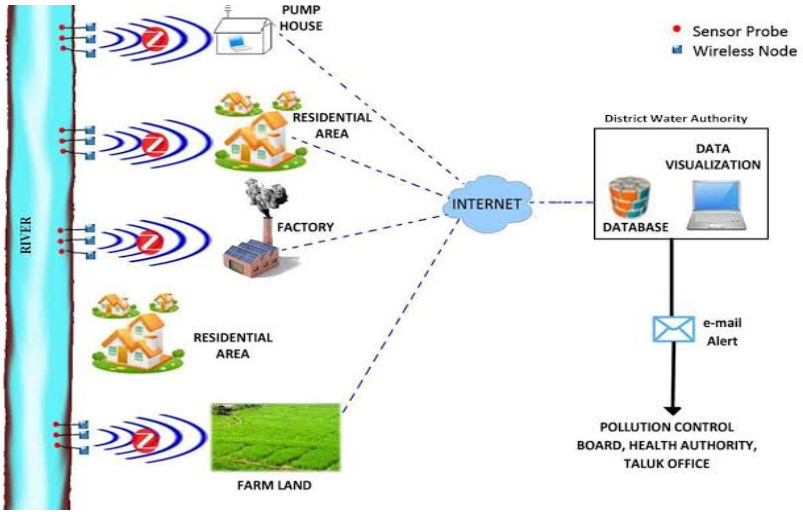


***Figure 7.*** *A typical smart water monitoring system using WSNs*

WSNs can be applied in monitoring the quality of water distributed in the country after setting a standard. The parameters that can be monitored include;

1. The pH level is the measure of the degree of acidity or alkalinity of the water distribution. However, a pH level between 6.0 and 9.0 is recommended for distribution systems.
2. Electrical conductivity: this is the measure of compatibility to pass an electric current. Conductivity is used as an indication of the concentration of conductive ions that normally come from dissolved salts and other inorganic material. The more the dissolved salts present, the higher the conductivity. Drinking water should have a conductivity that ranges between 0 and 2500S/cm.
3. Oxidation-Reduction Potential (ORP): this a measure of how strongly electrons are transferred between component species in a solution. This indicates the ability of water to get rid of its contaminants. A healthy should have a high ORP [13].
4. Turbidity: this indicates the concentration of suspended and colloidal material in water and it is measured in Nephelometric Turbidity Units (NTU). Drinking water should have turbidity that is less than 1 NTU [13].

**Challenges and Proposed Solutions**

A lot of factors have affected the implementation and integration of wireless sensor networks in Nigeria towards achieving sustainable development. The first major challenge is the lack of will-power by the government of Nigeria towards technological development. Politics and poor governance in Nigeria as evident in the mismanagement of public resources allocated to the different sectors and poor technical ability of personnel's placed in charge of the ministries. The second major challenge is the limited information or limited awareness of people to the various potentials and advantages achievable through the utilization of WSNs in Nigeria.

Nigeria has about 54 federal tertiary teaching hospitals but are all in dire need of facility and equipment upgrade. For Nigeria to solve the health challenges especially with the dearth of medical personnel, all the tertiary teaching hospitals should be upgraded and equipped with state of the art telemedicine facilities. The users of these facilities located in the cities who majorly have access to working internet facilities can make use of these WSN facilities for health monitoring and reporting.

The use of technology in agricultural monitoring should be encouraged to increase yield and reduce the overhead cost of applying fertilizers and irrigation systems. The Federal Ministry of agriculture should set up large agricultural estates across the 36 states of the federation. These estates should be equipped with sensors for precision agriculture to measure the soil moisture and with the application of drip irrigation will optimize the moisture need of the individual plants resulting in reduced water wastage especially in arid zones.

To achieve the nation's quest to supply its citizens with clean and potable water, the water corporations across the various states of the federation should be equipped with facilities for remote monitoring of the quality of water delivered to its various subscribers. Data centers should be set up across the states to remotely monitor, analyze, process and store data and information gotten to better serve the millions of customers depending on the corporations for usable water.

**Conclusion**

This study reviews the potentials of Wireless Sensor Networks in achieving sustainable development in a developing country like Nigeria. WSNs can be designed, developed and integrated into critical areas such as the health sector, agricultural sector and in environmental health monitoring to improve the way of life of the citizens of Nigeria.

It is highly recommended that more attention to be given to the implementation of WSN technology in the area of health, agriculture and environmental monitoring especially with the advent of the Internet of Things (IoT). With the right policies and a working framework for the implementation and deployment of WSN, Nigeria can improve its citizens' standard of living and take a giant step towards achieving the Sustainable Development Goals.

**References**

1. Pwc Report. Transforming Nigeria's Agricultural Value Chain. 2017.
2. Antolin D, Medrano N, Calvo B, Perez F. A Wearable Wireless Sensor Network for Indoor Smart Environment Monitoring in Safety Applications. Sensors. 2017;17:365-78.
3. Salamah M, Oyedeji AO. Regional-Based LEACH For Energy Efficiency In WSNs. International Research Journal of Electronics and Computer Engineering. 2016;2:7-13.
4. Cao H, Leung V, Chow C, Chan H. Enabling technologies for wireless body area networks: A survey and outlook. IEEE Communications Magazine 2009;47:84-93.
5. Aponte-Luis J, Gomez-Galan JA, Gomez-Bravo F, Sanchez-Raya M, Alcina-Espigado J, Teixido-Rovira PM. An Efficient Wireless Sensor Network for Industrial Monitoring and Control. Sensors. 2018;18:182-96.
6. Milenkovic A, Otto C, Jovanov E. Wireless sensor networks for personal health monitoring: Issues and an implementation. Computer Communications. 2006;29:2521-33.
7. Emmanuel AN. Challenges of implementing sustainable health care delivery in Nigeria under environmental uncertainty. Journal of Hospital Administration. 2016;3:113-26.
8. Muhammad F, Abdulkareem JH, Chowdhury AA. Major Public Health Problems in Nigeria: A review. South East Asia Journal of Public Health. 2017;7:6-11.
[9. Sadiku MNO, Eze KG, Musa SM. Wireless Sensor Networks for Healthcare. Journal of Scientific and Engineering Research. 2018;5:210-13.
10. Adebayo S, Akinwunmi AO, Aworinde HO, Ogunti EO. Increasing Agricultural Productivity in Nigeria Using Wireless Sensor Network (WSN). African Journal of Computing and ICT. 2015;8:121-28.
11. Seelan SK, Laguette S, Casady GM, Seielstad GA. Remote sensing applications for precision agriculture: A learning community approach. Remote Sensing of Environment. 2003;88:157-69.
12. Mulla DJ. Twenty five years of remote sensing in precision agriculture: Key advances and remaining knowledge gaps. Biosystems Engineering. 2013;114:358-71.
13. Pule M, Yahya A, Chuma J. Wireless sensor networks: A survey on monitoring water quality. Journal of Applied Research and Technology. 2017;15:562-70.

*Journal of Engineering Science* *Vol. XXVIII, no. 1 (2021), pp. 75 - 82*
*Fascicle* *Electronics and Computer Science* *ISSN 2587-3474*
*Topic* *Computers and Information Technology* *eISSN 2587-3482*

**https://doi.org/10.52326/jes.utm.2021.28(1).07**
**UDC 004.056.55:004.421**

# SPECTRAL SPACE AS A METHOD FOR DATA CRYPTO PROTECTION USING THE FAST FOURIER TRANSFORM

Anatoly Balabanov, ORCID ID: 0000-0003-1225-8247,
Vyacheslav Kunev, ORCID ID: 0000-0002-1095-214X,
Victor Colesnic*, ORCID ID: 0000-0001-8675-4062

Technical University of Moldova, 168 Stefan cel Mare bvd., MD-2004 Chisinau, Republic of Moldova
*Corresponding author: Victor Colesnic, *victor.colesnic@ati.utm.md*

Received: 01. 05. 2021
Accepted: 02. 17. 2021

**Abstract.** The article proposes to solve the problem of real-time application (on-line) of asymmetric bit-by-bit (flow or phoneme block, 32-, 64-,..., n-bits block) encryption of the linear and / or non-linear formants of the spectrum lines of Fast Fourier Transform (FFT) as an indirect analogue of a voice message. For this, modernized RSA-m algorithms are used and the spectrum of the voice message in the form of linear formants of number theory, while maintaining the high level of cryptographic resistance inherent of the RSA algorithm. The peculiarity of these algorithms consists in the fact that different lengths of cryptographic keys are used, which are changed with a sufficient frequency, depending on the required level of cryptographic resistance. This feature of the algorithms implements statistically independent encoding of the original message, by encrypting the adequate formants of the original message, i.e. a process characterized by a reduction (compression) of the amount of initial information and its redundancy, as well as an increase of its entropy (the average amount of information per character, phoneme or discrete (n-bit output from the ADC), because in a compressed context, statistically frequent sounds, letters, words, phonemes and even discrete, will be absent, which will significantly complicate the decryption (cryptanalysis) of the message.

**Keywords:** *cryptographic systems, online encryption, RSA modernization, RSA-m algorithms, formant analysis, cryptographic resistance.*

## Introduction

Any signals are - from the point of view of Fourier - an infinite sum of sinusoids of different amplitudes, frequencies and phases, which means, according to his famous Theorem - just some sequence of discrete (spectral lines) in the spectral space. And any text (or media data), as you know, can also be represented in a binary digital space - as a protocol, known in advance, some sequence of ones and zeros in the time (frequency) domain, i.e. also as a possible binary representation of any information, including (why not!) spectrum of some random signal consisting of 1 and 0!

The term "space" should not discourage the cryptographer, since reality and abstraction from it are natural in mathematics. However, the physical perception of these operations cannot always be adequately assessed immediately. The algorithmic and mathematical procedures, methods and operations described below relate to the field of mathematical and logical-algorithmic space in the field of cryptographic transformations and protection of confidential and / or stored information transmitted bit by bit or in batches, for use in computing and information systems, in local corporate networks, in radio communication systems, information and control complexes, in systems of mass mobile (cellular) telephony, confidential telephone digital communication of state, commercial, security and signaling enterprises and financial structures, as well as in devices such as the "global messenger" for encryption of binary information.

The listed devices must contain on the transmitting and receiving sides a speech converting devices (SCD) connected via a USB port or a wireless Bluetooth port, Wi-Fi, WiMax and the like to a radio, mobile and telephone communication device (smartphone, iPhone, tablet, etc. other existing or possible similar devices in the future) or to any other radio transmitter, which must contain an encryption unit between the SCD output and a mobile and other radio or telecommunication device, which implements algorithms for closing and protecting information in the online mode.

Today, dozens of patent methods and corresponding devices for cryptographic information protection are known [1 - 11]. These systems are characterized by the complexity of algorithms, operations, rather slow execution and insufficient cryptographic strength when receiving / transmitting online, which becomes especially noticeable in the conditions of post-quantum cryptography. Therefore, in the method described below, one of the tasks to be solved is associated with increasing the cryptographic strength.

An essentially similar method for encrypting binary information and a device based on it are described in [12], which describes a method for cryptographic protection of information in computing and information systems. It is based on encrypting digital, usually 64-bit blocks, using two keys - public and private, and is based on the use of one-way functions and arithmetic of large numbers. This method takes the computational complexity of the problem of factorizing a large number into prime factors (finding the divisors of a large number) in a reasonably short time. The disadvantage of this cryptosystem is the inability to influence the spectral characteristics of the transmitted information in the desired way.

**The tasks and goals set**

The aim of the present invention **is to apply in real time** (on-line) asymmetric bit-by-bit (streaming or block-phoneme, block on 32-, 64-, n-bit) **encryption of the linear and / or non-linear formants of the spectrum lines of Fast Fourier Transform** (FFT) as an indirect analogue of a voice message. For this, modernized RSA-m algorithms [12, 13] are used and **the spectrum of the voice message in the form of linear formants as a mathematical image** [14] (model, convolution), while maintaining the high level of cryptographic resistance inherent in the RSA algorithm. The peculiarity of these algorithms is that short lengths of crypto-keys are used, varying with a sufficiently high frequency, providing a short-term level of protection for conversations (3 - 10 minutes), and with an increase the level of long-term security (up to several months and years), the lengths of crypto keys are additionally changed to values that provide the required level of cryptographic strength.

This feature of the algorithms that implements the process of statistically independent coding of the original message by encrypting its adequate formants, i.e. the process characterized by a decrease (compression) in the volume of initial information and its redundancy, as well as an increase in its entropy (the average amount of information per symbol, phoneme or discrete), because in a compressed context, **statistically frequent sounds, letters, words, phonemes and even discrete will be absent**, **which will significantly complicate the decryption (cryptanalysis) of the message.** Objectives - improving the quality of cryptographic information processing, i.e. speed and stability of various durations of secrecy, increasing the speed of the encryption / decryption procedure by reducing the amount of information in an encrypted M-bit message, as well as expanding the functionality and application areas of the proposed method for protecting binary information.

Based on the rule of A. Kerckhoff (1835-1903): " a cryptographic system should be designed to be secure, even if all its details, except for the key, are publicly known", in the claimed method for encrypting binary information during its transmission over an open channel, not the original information is transmitted, but its image, an adequate model, i.e. some not obvious information about it, known only to the receiving party, or the internal software of the encryption device, based on which the original information can be easily restored. To do this, use, for example, one- or two-dimensional numerical formant [14], whose values change in time depending on the value of the digital representation of the protected information. The formant itself is transmitted encrypted using the RSA-m algorithm or some other, for example, a hybrid algorithm.

**The essence of the encryption method**

The essence of the method for encrypting binary information is to use the properties of the formant [13, 14] and the RM patent No. 4511, where any number can be uniquely represented as three small numbers (**in the case of a linear formant**), significantly smaller in absolute value than the original large number, **or a greater number of them in the case of using a two-dimensional formant.** Time of encryption and decryption of a large number formant, i.e. its parameters, declared by the RSAm algorithms, are much less than the time of encryption and decryption of the original large number, which is, for example, a 32-bit or 64-bit digital block in the classical RSA cryptosystem. The advantage of the formant representation of numbers for encryption is that the base of the formant can be any number, and simple and composite, which significantly increases the number sets for choosing a formant base for encryption (which increases the cryptographic strength of the algorithm) and for hacking it during crypto analysis which complicates this task for the attacker, for example, in the interval 2-3560 there are only 500 primes, i.e. 7 times less than all the numbers in the series.

Prime formants have a number of features [12 - 14] that are important for the RSA algorithm. In the inventive method, either only two parameters of the **nonlinear formant** are encrypted, or already encrypted formants are selected from the ROM according to a given algorithm (depending on the chosen method of protecting information), **and in the case of a two-dimensional formant, only a part of the formant is encrypted, the recovery of which is possible only on the receiving side using the second secret half of the formant, which does not participate in the formation of the encrypted information transmitted over the communication channel.**

For encryption, in the device under consideration, *KN* matrices of size $n \times n$ are created to store the module numbers $N = p'q'$, calculated in accordance with the Fermat algorithm based on the primes $p'$ $and$ $q'$ of RSA encryption and pre-selected pairs of crypto-keys $e_i$ $and$ $d_i$ with different length $\mu(s_i)$ bit, and $\boldsymbol{PF}$ matrix to storage bases $p_i$, cores $k_i$ and remainders $q_i$ of formants corresponding to the open message code and an $n \times n$ R matrix for storing M-bit random bit sequences for encoding encrypted blocks of information.

In the process of broadcasting a conversation through a communication channel figure 1, (radio, mobile phone, Internet, etc.), each discrete at the ADC output (2) with an amplitude $A_d(t_i)$ bits is considered as the address of the location of crypto-keys located in ROM (4) in PF matrices with a volume of $2^{32}$, where crypto-keys are randomly distributed to addresses, i.e. the matrix address does not match the discrete value.

Encryption is performed in two stages:

1) finding the formant parameters - the core $k_i$ and the remainder $q_i$ for the next amplitude $A_d(t_i)$ of the discrete (block phoneme) on the base $p_i$;

2) encryption by the RSAm algorithm of the formant parameters $k_i$ and $q_i$ on modulo $N_i$ with their own individual crypto-key $e_i$. (i-number of the encrypted / decrypted discrete or information block, according to the asymmetric RSA cryptosystem algorithm $e_i d_i (mod N) = 1$).

After each communication session, the key addressing in the ROM is automatically changed according to the software algorithm. Thus, the proposed method is actually equivalent to encrypting a message with a one-time key with a random length equal to the length of the bits of the discrete or block (depending on the selected algorithm), which corresponds to the conditions of Shannon's theorem on the impossibility of decrypting [12,14]. The use of hardware implementation will provide increased encryption speed.

Difference of the proposed algorithm from its analog [12] **is that not the real digital information at the microphone output is encrypting, but its spectral representation as a result of the discrete FFT of an online message** with its encryption based on algorithms for the formant representation of FFT-transformed information.

The set goals and results are achieved through the use of: 1) RSA algorithms in real time (on-line) with significantly shortened crypto key lengths and 2) fast algorithms for fetching from memory, pre-generated, random bit sequences with the declared cryptographic strength of the information security system **to increase the speed of operation, productivity, usability and a significant expansion of application areas** for protected technologies. The method for encrypting binary information is implemented on the basis of combining blocks and devices for converting, encoding and cryptographic processing of information into a single system, communication channels and at the same time, the device itself for cryptographic information processing is made as a channel, and there are at least two of them.

***Abbreviations and symbols used in the text and in Figure 1:*** **SCD** (1) – speech converting devices, **ADC** (2) - analog-to-digital and **DAC** (13) - digital-to-analog converters; **ROM** (4) - read-only memory; **SO** - software; **CD** (4) - computing device and software; **BGP** (7) - block for generating and processing service information; **MC** - microcontroller; $\boldsymbol{k, l}$ - number of bits of crypto-keys $\boldsymbol{e_i, d_i}$ of encrypted and decrypted messages; $\oplus$-logical operation modulo 2 addition; encryption algorithm **RSA** - using large numbers for crypto keys $\boldsymbol{e_i, d_i}$ and for module **N**; modernized encryption algorithm $\boldsymbol{RSAm - ABi}$ - using small

numbers for crypto keys $\boldsymbol{e_i, d_i}$ and for module **N**, but with a high frequency of their change; $\boldsymbol{N = p'q'}$ - the multiplication of small coprime numbers chosen according to Fermat's theorem; $\boldsymbol{A_m(t_i)}$ – amplitude of the current discrete $\boldsymbol{D_i}$ of the message $\boldsymbol{S_0}$; $\boldsymbol{KN}$ – matrix of addresses of parameters of the current crypto-lock: pair of crypto keys $\boldsymbol{e_i, d_i}$ and module $\boldsymbol{N_i}$; $\boldsymbol{PF}$ - matrix of formant parameters: base $\boldsymbol{p_i}$ of formant; core $\boldsymbol{k_i}$ and remainder $\boldsymbol{q_i}$; $\boldsymbol{R}$ – a matrix of random $\boldsymbol{M}$ –bit numbers (random bit sequences), where $\boldsymbol{M}$ is the length of the transmitted message to the open communication channel; phoneme or block phoneme - a set of discrete from several 4, 6 or 8 bytes, considered as a bit integer.

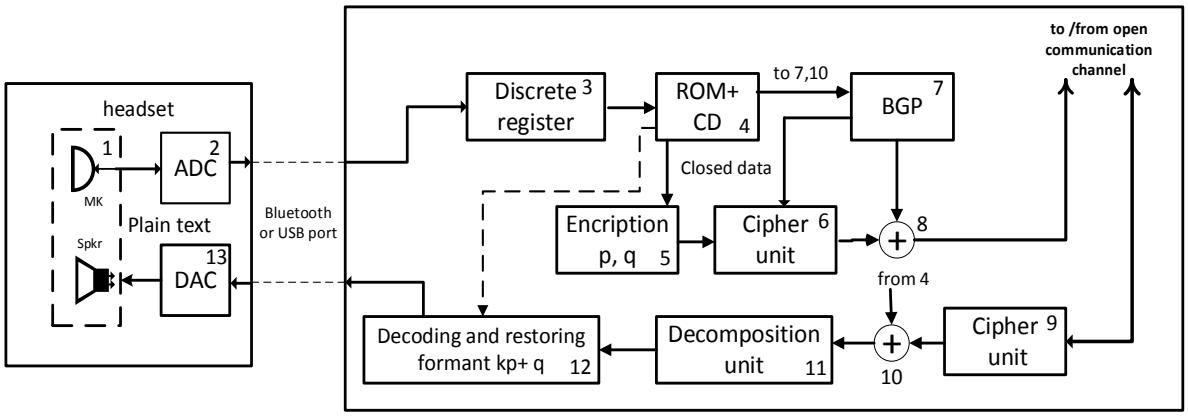


**Figure 1.** Block diagram of the encryption and decryption device.

In the information transmission path Figure 1, after the ADC (2), which converts the analog electrical signal of sound, speech into digital form from the output of the speech converting devices SCD (1), form digital n-bit blocks of the information part and auxiliary components for bitwise encryption of each discrete of the digital block based on the methods of formant analysis [13, 14]. Each such protected information block is transmitted to the communication channel in packet form using the discrete register (3), a computing device (4) and a read-only memory device (ROM) (4), which, after formant converter (5), an cipher unit (6), and a generator of a random M-bit bit sequence for noise immunity of a message from the BGP output (7), summed up modulo 2 in block (8).

In the information receiving path, encrypted coded packets are restored in communication channels using a cipher block (9), a decoder (10), block of decomposition into information and auxiliary parts (11), decryption of information blocks and restoration of the formant of the signal spectrum in block (12) based on formant analysis algorithms using the program for controlling the operation of CD blocks (4) of microcontrollers at the receiving and transmitting sides, which is an informational and technical result, with the restoration of a continuous analog speech signal based on a speech converting devices (1) connected to the output of a digital-to-analog converter DAC (13), which converts a decoded digital signal into an analog one.

The considered method of encrypting information is based on the transmission *not of the signal spectrum (the information itself), but some special indirect information about the signal spectrum, called a formant or image, model, convolution,* etc., the volume of which is significantly less than the original and, therefore, can be transmitted in encrypted form in real time (on-line) with the required level of cryptographic strength based on the "classical" algorithm of the asymmetric RSA cryptosystem.

The proposed method of encrypting information differs from the known, in that it is actually equivalent to practical message encryption with a one-time key with a random length equal to the bit length of a discrete or a block (depending on the chosen algorithm) **using real-time encryption**, which corresponds to the conditions of Shannon's theorem on the impossibility of decryption [12,14].

Indeed, block encryption can be done in two ways:

**Without feedback loops** (FL), when several bits - one discrete or phoneme - a block, for example, from 12 bit - of the original text (digitized speech by a 12-bit ADC) are encrypted sequentially, and each bit of the original block affects each bit of the cipher text. However, there is no mutual influence of the blocks (the previous discrete does not affect the next one and vice versa), that is, two identical blocks of the original text (but not speech) would be represented by the same ciphertext. Therefore, such algorithms can only be used to encrypt a random sequence of bits. Using formants (parameters - base $p_i$**,** core $k_i$ and remainder $q_i$) this is not the case.

**The same sequence of bits will be represented by different cipher text**. In other words, the proposed encryption method will provide statistical independence of open messages and cryptograms. But, as in the case of polyalphabetic substitutions, since the set of used formant bases is not infinite, then after a certain number of blocks they will have to be used again. Note that when randomly using numbers for base of formants, such an incident can occur, but quite rarely. Indeed, 11000 discrete / sec (the sampling of the analog signal is performed at a frequency of 11 kHz) in the presence of 10,000 different variants of the bases of the formant, will give a very small probability of coincidence of 2 encrypted texts even with monotonous sound - an ideal sinusoid:

$$p_{sovp} = \left(\frac{2}{11000}\right) \cdot \left(\frac{1}{10000}\right) = 0{,}18 \cdot 10^{-3} \cdot 10^{-4} = 18 \cdot 10^{-9} \quad (1)$$

Then 3 minutes = 180 seconds of a digitized conversation represent

$(11 \cdot 10^3) \cdot 180 = 198 \cdot 10^4 \approx 2 \cdot 10^6$ discrete, and the probability of coincidence of two identical discrete with their cipher texts will be

$$18 \cdot 10^{-9} \cdot 2 \cdot 10^6 = 36 \cdot 10^{-3}.$$

But even such a relatively low probability of coincidence of two bits on a time interval of 3 minutes does not mean anything, because we are talking about only one discrete, and in order to distinguish a sound (or even an alphabet symbol), you need a well-defined sequence of not two, but sets of samples (from several hundred to thousands!). Then the probability of coincidence of two cipher symbols or, moreover, cipher phonemes, decreases due to the appearance of huge quantities of a combinatorial nature in the denominator of formula (1), since for a text symbol this probability of coincidence of two discrete (phonemes) $p_{sovp} = \mathrm{C}_{10^2}^{10^{-9}} \approx 10^{-80}$, , and for the phoneme of sound, the number of permutations will have to be counted even 10 times more, i.e. for a phoneme, the probability will decrease to the order of

$$\mathrm{C}_{10^3}^{10^{-9}} \approx 10^{-800}.$$

Astronomically small numbers! Therefore, the probability of hacking on the basis of statistical analysis of the text cipher with the proposed encryption method is reduced to almost zero.

As a figurative explanation of the complexity of hacking this cipher by the "brute force" method, we can give an example from the famous TV game "Guess the melody", when a game participant needs to guess the melody by three consecutive sounds or notes. Note that the digital representation of the "task" to the guessing person means (represents) not 3 (three) consecutive correct discrete, but the correct sequence, at least $33 \cdot 10^3$ discrete provided that the sound is sampled at a frequency of 11 kHz!

It is clear that it is impossible to recover the necessary melody, even known in memory, from three discrete in a reasonably short time, even when using a high-speed computing (a quantum computer, for example!).

In another, much simpler the game "Guess the Word", where you need to reconstruct an unknown word of length N letters from 3 ... 4 letters. In this case, the computer finds a solution in a split second. What is the difference? The number of different sorting options and known / unknown " full original"). When recognizing unknown music, the number of options is the same, but the time of hacking is infinite, if the Man himself is not involved or some model of artificial intelligence is not involved in the process of recognizing an unknown melody or speech. But encrypted messages (speech, text, image, video and other media information) are unknown in advance.

**Encryption with FL** is usually organized to increase noise immunity as follows: the previous encrypted block is added modulo 2 with the current block. The initialization value is used as the first block in the FL chain. An error in one bit affects two blocks - the erroneous and the next one.

## Conclusions

In the proposed method for encrypting binary information using RSA_mAB algorithms, the transmitted encrypted FFT packet is additionally encoded with the "xor" cipher before being sent to the communication channel.

Therefore, to break the cipher, an attacker will first have to decode this cipher packet and after decrypt each spectral line (discrete) of the spectrum, which will require additional time and may significantly overlap the guaranteed secrecy period, after which all encryption data will already be deleted from the system

Using a fully hardware implementation, not software, of the microprogram machine would provide a higher encryption speed.

**References**

1. GOST 28147-89. [Information processing systems. Cryptographic protection. Cryptographic transformation algorithm], http://docs.cntd.ru/document/gost-28147-89 [in Russian].
2. Moldovyan A.A., Moldovyan N.A., [Method for block iterative encryption of binary data], https://findpatent.ru/patent/221/2212108.html [in Russian].
3. Guts N.D. i dr., [Iterative Block Cipher Method], https://findpatent.ru/patent/217/2172075.html [in Russian].
4. Klepov A.V., [Method for cryptographic protection of information in information technologies and a device for its implementation], https://findpatent.ru/patent/220/2206182.html [in Russian].
5. Chizhukhin G. N., [Method for encrypting binary information and device for its implementation], https://findpatent.ru/patent/209/2091983.htm [in Russian].
6. Volkov S. S. i dr., [Method for encrypting binary information and device for its implementation], https://findpatent.ru/patent/209/2096918.html [in Russian].
7. Averin S. V. i dr., [System of secret transmission and reception of voice information], https://findpatent.ru/patent/209/2099885.html [in Russian].

8. Lysenko V. V. i dr., [Mobile information security device with an increased level of security], http://poleznayamodel.ru/model/8/83861.html [in Russian].
9. Lysenko V. V. i dr., [Mobile information security device], http://poleznayamodel.ru/model/8/83862.html [in Russian].
10. Fodorov i dr., [Encryption-decryption device], patent RF № 2108002 http://www.findpatent.ru/patent/210/2108002.html [in Russian].
11. Khrenov V. P., [Information security system], patent RU 2 325 6956 http://www.freepatent.ru/images/patents/140/2325695/patent-2325695.pdf [in Russian].
12. Balabanov A. A., Dispositiv şi procedeu de protecţie criptografică a informaţiei binare (variante) [Device and method for cryptographic protection of binary information (variants)], patent RM №4511, 2016.04.20
13. A.A. Balabanov, A.F. Fodorov, I. Kozhukhar. [Possibilities of creating new and modernized algorithms for the RSA system]. Vestnik nauchno-tekhnicheskogo razvitiya, VNTR, №9 (37). Sept. 2010, http://vntr.ru/ftpgetfile.php?id=451 [in Russian].
14. Agafonov A.F., Balabanov A.A., [Comparative analysis and its applications. Modern and classical problems of number theory and cryptography] ,Ed., LAP Lambert Academic Pudlishing, Germany, 201 c., ISBN 978-3-659-92621-1, 2016 [in Russian].

*Journal of Engineering Science* *Vol. XXVIII, no. 1 (2021), pp. 83 - 90*
*Fascicle* *Electronics and Computer Science* *ISSN 2587-3474*
*Topic* *Computers and Information Technology* *eISSN 2587-3482*

**https://doi.org/10.52326/jes.utm.2021.28(1).08**
**UDC 004:530.145**

# QUANTUM COMPUTING

Titu-Marius I. Băjenescu*, ORCID ID: 0000-0002-9371-6766

Swiss Technology Association, Electronics Group Switzerland
*Corresponding author: Titu-Marius I. Băjenescu, *tmbajenesco@gmail.com*

Received: 18. 12. 2020
Accepted: 10. 02. 2021

**Abstract.** The quantum computer, is a "supercomputer" that relies on the phenomena of quantum mechanics to perform operations on data. Object of suppositions, sometimes far-fetched, quantum mechanics gave birth to the quantum computer, a machine capable of processing data tens of millions of times faster than a conventional computer. A quantum computer doesn't use the same memory as a conventional computer. Rather than a sequence of 0 and 1, it works with qubits or quantum bits. The quantum computer is a combination of two major scientific fields: quantum mechanics and computer science. Quantum mechanics, on which this computer is based, governs the movement of bodies in the atomic, molecular and corpuscular domains, is a theory whose logic is totally contrary to intuition and it is essential to use mathematics to fully grasp it. Quantum computing is the sub-domain of computer science that deals with quantum computers using quantum mechanical phenomena, as opposed to those of electricity exclusively, for so-called "classical" computing. The quantum phenomena used are quantum entanglement and superposition. The article examines some aspects related to the development, operation, advantages and difficulties, applications and future of the quantum computer.

**Keywords:** *Quantum theory, quantum information, quantum mechanics, photon teleportation, quantum computer, EPR paradox, qbits.*

## Introduction

It was in the early 1980s that scientists began to realize that the future of the computer was based on quantum theory. Indeed, they became aware that today's computer was approaching its limits because you can't miniaturize to infinity. The hypothesis that emerged from this realization was that the next evolution of the computer would be based on quantum theory. However, this theory is older than that. The physicist Richard Feynman was the first to study the question in the 1960s [1].

The principle of the quantum computer is based on the properties of quantum mechanics. Einstein, himself, challenged quantum mechanics and proposed an experiment, which he called the EPR paradox, to prove that quantum mechanics was inaccurate. However, this experiment could only be carried out in 1981 by Alain Aspect because the technology of the time did not allow its realization. The result of this experiment proved, without any dispute, that quantum mechanics governed the movement of atoms [2, 3].

In 1996, Lov Grover (Lucent Technologies) designed a quantum algorithm that only needs √n queries to an oracle *f* to find an element that satisfies *f* in a non-ordered database of size *n*, where classical computation requires *n* queries to the same oracle [4].

From 1999 to 2002, Isaac Chuang (IBM Research) designed and built a quantum computer which, although limited to 7 bits, was used to show that physics can indeed experimentally implement the new algorithmic principles imagined at the theoretical level by Peter Shor and Lov Grover.

The first computation of a quantum computer took place in 2001 [5]. This first calculation is 15=3*5. This computation may seem insignificant and extremely simple but it is very important because it opens the way to practical applications.

**History of the quantum computer**

In 1993, Charles Bennett (IBM Research), Gilles Brassard (Université de Montréal) and other scientists discovered the premises of the quantum computer because they highlighted a property of quantum information. This property goes against all the rules of classical physics. This team of scientists is setting up a teleportation protocol that uses the properties of the EPR link discovered by Einstein [6]. The EPR link is a kind of bond between two particles. This means that the two particles are linked together and any action on one causes the other to react. So, if the state of one of the two particles changes, the other particle will undergo the same change at the same time. It is thanks to this protocol that Anton Zeilinger (University of Vienna) carried out the first photon teleportation in 1997.

In 1994, Peter Shor, from the AT&T laboratories, had devised an algorithm using this property to factorize very large numbers in "polynomial" time, which means, in mathematical language, that increasing the size of the encryption keys would no longer be an insurmountable obstacle.

**How the quantum computer works**

We have seen that we are only at the beginning of the quantum computer and that this computer is based on the principle of quantum mechanics [7].

Today's computers use bits that have two states that are either 0 or 1. A quantum computer doesn't use the same memory as a conventional computer. Rather than a sequence of 0 and 1, it works with qubits or quantum bits. These qubits will have the state 0, the state 1 but also, and this is what makes them very interesting, they will also have both states at the same time that is to say 0 and 1. Indeed, it is on this principle of superposition, which is that a qubit has both states 0 and 1, that the quantum computer is based. This state of superposition, specific to qbits, gives a quantum computer a computing capacity that is impossible to achieve otherwise [8].

The state of a register of 2 qubits could then be 0, 1, 2 or 3, but also a superposition of any part of these four basic states, or even all four at once. The state of a register of n qubits could be a superimposition of any set of the 2n possible values on n bits, including a superimposition of all these values at the same time, whereas a classic n-bit register can only contain, at each instant, one of these values.

Therefore, since the calculations will transform the state of such registers, any operation performed during a quantum calculation will be able to act simultaneously on 2n different values. This brings a massive parallelism: if a function can be computed with 2n different arguments, all its values will be computed simultaneously. The laws of quantum physics impose that these simultaneous calculations are reversible and deterministic, which

does not reduce what can be calculated, but they do not allow to copy the state of a register into another register [9, 10]. Therefore, in a program, we will not be able to assign the value of one quantum variable to another, nor will we be able to use this value several times. This property forces us to invent a new algorithm and programming languages that respect the laws of quantum mechanics.

Once a computation is completed, the desired result is one of the values superimposed in a register. To extract the result, physicists will have to perform what they call a measurement of this register. According to the laws of quantum physics, this measurement will produce one of the superimposed values in the register, each with a certain probability and, at the same time, it will reduce the superimposition contained in the register to a single value, the one chosen [11]. The measure therefore causes the superimposed states to collapse. The right value will eventually be obtained if the quantum algorithm has been well designed. So, the goal of the quantum algorithm is to bring the probability of obtaining a relevant result as close to 1 as possible, and this by performing as few operations as possible.

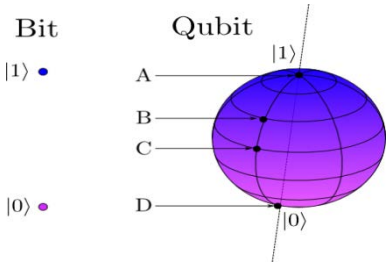


**Figure 1.** Entanglement is an extraordinary resource.

Let's take two objects, A and B, which each have several possible states. While classical physics tells us that the state of the pair A,B is none other than the pair of the state of A and the state of B, in quantum mechanics this assertion is no longer true. Indeed, it may be that the pair A,B has a state, whereas neither A nor B has a state of their own. It is then said that A and B are intertwined. Unparalleled in the classical world, entanglement is an extraordinary resource [12]. For example, if A and B are registers of qubits, and if they have been entangled during a calculation, we can imagine the state of the pair A,B as inseparably linking each of the values superimposed in A to one or more of the values superimposed in B. Thus, if we measure A, its state is reduced to only one of the values it contained, but the state of B is also reduced, at the same time, to the superposition of the values that were linked to the one that remained in A. This is true if A and B are side by side, but remains true if they have been millions of kilometres apart after being entangled. The couple A, B is always the couple A, B no matter how far apart they are.

**Advantage of the quantum computer**

We saw earlier that the quantum computer was the result of the use of qubits.

The main advantage of this computer is the saving of time. Indeed, the fact that qubits can have state 0 and state 1 at the same time saves a considerable amount of time. To illustrate this, let's take a simple example, the opening of a padlock.

To find the right combination of the classical padlock, you would have to try, one by one, each of them until the padlock opens. However, the quantum padlock tries all possible combinations at the same time and can find the right combination much faster than the classic padlock.

**Difficulties of such a computer**

Prototypes are already appearing, with a maximum of 50 qbits, but these are very noisy, i.e. the results they give are still too often erroneous. There are several problems that scientists will have to solve. First of all, there is the problem of reading information. Indeed, we know that quantum mechanics is indeterministic [13]. That is to say, we do not know the

state of the atoms. For example, if we perform a calculation, we do not know the result and reading this result destroys the information. To be clearer, if we perform a complicated calculation, we will only know the final result. Indeed, the intermediate results will be inaccessible, otherwise the information will be destroyed and thus the calculations will stop.

This problem has not yet been solved by scientists. However, we have seen that a team of researchers had carried out the following factorization: 15=3*5. This is due to the fact that there was no intermediate result. Therefore, this problem of loss of information exists only when we need to know intermediate results and does not exist when only the final result interests us [14].

The second problem is the physical realization of a quantum computer. Scientists have several leads. Indeed, qubits can be of different types. They can be photons, therefore light, molecules or atoms. But it is the method of molecules or atoms that is the most promising. Indeed, nuclear magnetic resonance, which creates a magnetic field greater than 2 Tesla, is capable of changing the quantum state of the nuclei of molecules and atoms. However, this method has a constraint: helium and liquid nitrogen must be regularly replaced to ensure superconductivity because the products tend to evaporate.

The main problem facing quantum computing is building computers [15]. Compared to a normal computer, a quantum computer is an extremely complex machine: they operate at a temperature close to absolute zero (-273 ºC), the qubits support are superconducting and the components to be able to read and manipulate the qubits are not simple either.

A priori and with the materials that quantum computers are being built with, it does not seem that miniaturization is too feasible. But there is already research on new materials that could be used to create more accessible quantum computers [16].

**The future of the quantum computer; when is it due?**

Unfortunately, that question cannot be answered precisely. Indeed, it would be risky to give a precise date because we have seen that many obstacles are on the road to this new type of computer. In addition to the technical problems, there is an additional difficulty [17].

Indeed, the arrival of the quantum computer depends largely on the interest it can generate for governments. Because technological advances are very rapid when there is competition. Examples of this phenomenon can be found in history, for example, nuclear fusion to produce industrial energy. For years, experimental reactors lived in a state of general indifference. Then suddenly, following the interest shown by the United States in an atmosphere of competition with Europe and the rest of the world in mastering this energy of the future, the ITER programme came to fruition and became the best example of this phenomenon [18].

In the field of quantum physics, it is the government authorities that fund research. So it is these authorities who are competing and who decide on the interest that such a computer has for their country. However, if one country makes significant funds available to fund research on the quantum computer, the authorities in other countries capable of carrying out such research will, in a way, be obliged to react and thus fund the research.

Google may have achieved quantum supremacy, but some of other projects have the potential to achieve this soon, including those of IBM, IonQ, Rigetti and Harvard University. These groups are using several distinct approaches to building a quantum computer.

Google, IBM and Rigetti are performing quantum calculations using superconducting circuits. IonQ uses trapped ions. The Harvard initiative uses rubidium atoms. Microsoft's approach concerns "topological qubits" [19-23].

It would appear that the United States of America has grasped the interest of developing such a computer. It is said to have encouraged its research laboratories and companies to acquire technological mastery of it and to generalise its use for its own benefit, well ahead of its competitors [24,25]. Today, it is well known that the ability of American science and industry to rely on networks of very large computers is one of the principal means of ensuring their supremacy. Thus, according to all this information, some scientists have ventured to advance a date for the development of the quantum computer. According to them, this computer will be designed short after 2020 [26 - 28].

**Applications**

There are several possible applications for the quantum computer. First of all, there is the scientific field. This computer could be used to make calculations and simulations that take a lot of time to be carried out by conventional computers. This will allow science to advance much faster because scientists will waste less time waiting for calculations or simulations to be done by the computer [29].

The first application is molecular simulation, the ability to describe matter on a very small scale, the atomic scale [30, 31]. This molecular simulation has many applications, such as finding new drugs or more resistant materials. These are often referred to as room temperature superconducting materials, capable of transferring energy without any loss [32, 33]. Molecular simulation is also interested in chemical reactions, which could make it possible, for example, to design new fertilisers.

The other family is optimization problems, which are the domain of operational research. This consists of finding optimal solutions to problems that have a very large number of possibilities. For example, optimising road traffic or finding the optimal load for a ship [34]. The most plausible application is cryptography, the science of encryption. Nowadays, encryption keys are, to be 100% sure of their effectiveness, as long as the message you want to transmit. This is Vernam's one-time pad (also called a "disposable mask"). It has, for example, been used to encrypt the red phone between Washington and Moscow. The major disadvantage of this encryption process was the size of the key, which had to be as long as the message to be sent [35]. Until then, it was transported via the diplomatic pouch, which is not 100% secure.

The quantum computer will solve this problem [36, 37]. Security will then be ensured by the laws governing quantum mechanics and not by mathematical theorems.

In routing the encryption key, the corresponding information will be transmitted through photons, each of which is polarized.

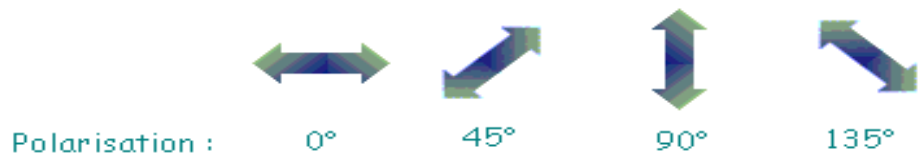


**Figure 2** Polarization of the photons.

Polarization is measured by an angle varying from 0° to 180° and can take four values: 0°, 45°, 90°, and 135°. When the photons are polarized from 0° to 90°, the polarization is called rectilinear polarization. For those polarized from 45° to 135°, one speaks about diagonal polarization:

In order to detect the polarization of photons, it is possible to use a polarizing filter followed by a photon detector [38]. If the filter is oriented at 0°, when a photon polarized at 0° passes through it, it is recorded by the detector. Conversely, if the photon is polarized at 90°, the detector will not record anything. In the last case where a photon is diagonally polarized, it would be recorded every other time. In the same way, if the filter is oriented at 135°, the same phenomenon will occur as for rectilinearly polarized photons, i.e. rectilinearly polarized photons will be detected every other time and the others will be detected or not [38].

Ford optimizes road traffic and fights congestion. Thanks to a quantum-inspired algorithm, the manufacturer is able to assign a given route to each vehicle, for an average journey gain of 8% [39, 40].

OLED display materials developer *OTI Lumionics* is boosting its research into new materials by using quantum inspired technology to simulate a constituent molecule of OLED materials.

Case Western Reserve University (CWRU) is perfecting magnetic resonance imaging (MRI) technology. Using the quantum approach, the university has succeeded in improving image quality by 30% and reducing image acquisition time by a factor of three.

The Canadian company D-Wave has just released its fourth model: the D-Wave 2000Q. As its name suggests, it has twice as many quantum bits, with its 2000 qbits [41]. During tests, the machine was able to achieve calculation times 1,000 to 10,000 times faster than with conventional processors. However, it was necessary to design algorithms specific to this machine to obtain this result.

Application of quantum machine learning can help in improving pattern recognition, which, in turn, will make it easier for scientists to predict extreme weather events and potentially save thousands of lives a year [42]. With quantum computers, meteorologists will also be able to generate and analyse more detailed climate models, which will provide greater insight into climate change and ways to mitigate it.

**Conclusion**

We have seen that it is now 20 years since scientists realized that the conventional computer would soon reach its limits. This is why some of them have seen in quantum mechanics the future of the computer. However, many problems very quickly got in the way of their dream. Indeed, the quantum computer made all scientists dream because it has, in theory, no speed limit. But quantum mechanics is still very poorly mastered, which poses a huge problem when you want to build a machine based on it. Indeed, the reading of quantum information and the physical construction of the computer are still to this day an almost insurmountable obstacle.

However, all the promises made by the quantum computer encourage scientists to continue their research and to multiply experiments. It is the promises made by this exceptional computer that will enable it to see the light of day. Indeed, the considerable benefits derived from this machine have prompted the United States of America to fund research on the quantum computer and thus be able to realize it short after 2020.

This formidable machine will probably never be marketed to the general public. Indeed, although it has many advantages, the problems to develop it are too complicated to realize it in an industrial way. That is why only scientists and companies that need these incredible capabilities, such as the military or video game manufacturers, will be able to use it.

**References**


1. Feynman R. P. (1982), "Simulating Physics with Computers", Int. J. Theor. Phys., No. 6/7, 21 (1982).
2. Nielsen M. E. and Isaac L. Chuang, (2011), "Quantum Computation and Quantum Information", Cambridge U. Press.
3. Press W. H., Saul A., TeukolskyWilliam T. Vetterling, Brian P. Flannery (2007), "Numerical Recipes: The Art of Scientific Computing", 3rd edn. Cambridge University Press.
4. Pacher C., Abidin A., Lörunser T., Peev M., Ursin R., Zeilinger A., Larsson J. (2016), "Quantum Information Processing", 15, 327
5. Greenberger D. M., Horne M.A., Zeilinger A. (2007), 2007 arXiv0712.0921G
6. Shimony A. (2017), in "The Stanford Encyclopedia of Philosophy", ed. by Edward N. Zalta (Fall 2017 Edition), https://plato.stanford.edu/archives/fall2017/entries/bell-theorem/
7. Leibfried D., Blatt R., Monroe C. and Wineland D. (2003), Review of Modern Physics 75, 281
8. Vool U. and Michel Devoret (2017), arXiv:1610.03438v2.
9. Wiliams C. P. (2011), "Explorations in Quantum Computing", Springer.
10. I. A. Boutle, J. E. Eyre, and A. P. Lock (2014), "Seamless Stratocumulus Simulation across the Turbulent Gray Zone", Mon. Wea. Rev., 142 (2014).
11. Castelvecchi D. (2017), "Quantum Computers Ready to Leap out of the Lab", Nature, 541 (2017).
12. Childs A. and van Dam W. (2010), "Quantum Algorithms for Algebraic Problems", Rev. Mod. Phys., 82 (2010).
13. D. Deutsch (1985), "Quantum Theory, the Church-Turing Principle and the Universal Quantum Computer", Proc. Roy. Soc. London, Ser. A, 400 (1985).
14. Dudhia J. (2014), "A History of Mesoscale Model Development", Asia-Pacific J. Atmos. Sci., No. 1, 50 (2014).
15. M. Hawkins (2017), "Complex Supercomputer Upgrade Completed", ECMWF Newsletter, No. 151 (2017).
16. Hong S. Y. and Dudhia J. (2012), "Next-generation Numerical Weather Prediction: Bridging Parameterization, Explicit Clouds, and Large Eddies", Bull. Amer. Meteorol. Soc., 93 (2012).
17. Landauer R. (1961) "Irreversibility and Heat Generation in the Computing Process", IBM J. Res. Dev., 5 (1961).
18. MetOffice Science Strategy (2015): "2016-2021, Delivering Science with Impact", (MetOffice, 2015), http://www.metoffice.gov.uk/research/overview.
19. Montanaro A. (2016), "Quantum Algorithms: An Overview", npj Quantum Information, 2 (2016).
20. National Centers for Environmental Prediction Strategic Plan 2015-2019. Version 4, February 27 (NCEP, 2015), http:www.ncep.noaa.gov/director/strategic_plan/strategic_plan.pdf.
21. Lauritzen P. H., Jablonowski C., Taylor M. A., and Nair R. D. (Eds.) (2011), "Numerical Techniques for Global Atmospheric Models", Lecture Notes in Computational Science and Engineering, 80 (2011).
22. Brunet G., Jones S., and Ruti P. (Eds.), (2015), "Seam less Prediction of the Earth System: From Minutes to Months", WMO, No. 1156 (WMO, 2015).
23. Shin H. H. and S.-Y. Hong, (2013), "Analysis of Resolved and Parameterized Vertical Transports in Convective Boundary Layers at Gray-zone Resolutions", J. Atmos. Sci., 70 (2013).
24. Shor P. W. (1997), "Polynomial-time Algorithms for Prime Factorization and Discrete Logarithms on a Quantum Computer," Siam J. Computing, No. 5, 26 (1997).
25. Simmons A. J. and Hollingsworth A. (2002), "Some Aspects of the Improvement in Skill of Numerical Weather Prediction", Quart. J. Roy. Meteorol. Soc., 128 (2002).
26. Wedi N., Hamrud M., and G. Mozdzynski (2013), "A Fast Spherical Harmonics Transform for Global NWP and Climate Models", Mon. Wea. Rev., 141 (2013).
27. Smith J. and Mosca M. (2012), "Algorithms for Quantum Computers", in Handbook of Natural Computing,Springer, Berlin,
28. Trabesinger A. (2017), "Quantum Computing: Towards Reality", Nature Outline, 543 (2017).
29. Tygert M. (2010), "Fast Algorithms for Spherical Harmonic Expansions", III, J. Comput. Phys., 229 (2010).

30. Walters D., Boutle I., Brooks M., et al. (2017), "The Met Office Unified Model Global Atmosphere 6.0/6.1 and JULES Global Land 6.0/6.1 Configurations", Geosci. Model Dev., 10 (2017).
31. Wedi N., Hamrud M., and Mozdzynski G. (2013), "A Fast Spherical Harmonics Transform for Global NWP and Climate Models", Mon. Wea. Rev., 141 (2013).
32. Williamson D. L. (2017), "The Evolution of Dynamical Cores for Global Atmospheric Models", J. Meteorol. Soc. Japan, 85 (2007).
33. G. Zangl, D. Reinert, P. Tripods, and M. Baldauf (2015), "The ICON (ICOsahedral Non-hydrostatic) Modelling Framework of DWD and MPI-M: Description of the Nonhydrostatic Dynamical Core", Quart. J. Roy. Meteorol. Soc., 141 (2015).
34. Martin F. (2019), "Top 10 Unexpected future applications of quantum computers", https://listverse.com/2019/01/10/top-10-unexpected-future-applications-of-quantum-computers/
35. Zygelman B. (2018), "A first introduction to quantum computing and information", Springer.
36. Magniez F. "Introduction au calcul quantique", http://www.lri.fr/quantum
37. Fujii K. (2015), "Quantum Computation with Topological Codes", Springer Briefs in Mathematical Physics Bernstein D., Buchmann J., Dahmen E. (2008), „Post-Quantum Cryptography", Springer.
38. Buterin V. (2013), "Bitcoin is Not Quantum-Safe, and How We Can Fix it when Needed", Bitcoin Magazine. bitcoinmagazine.com/6021/bitcoin-is-not-quantum-safe-and-how-we-can-fix/
39. Diffie W., Hellman M. (1976) "New Directions in Cryptography". IEEE Transactions on Information Theory, IT-22: 644–54
40. Hagar A. (2011), "Quantum Computing", The Stanford Encyclopedia of Philosophy. plato.stanford. edu/entries/qt-quantcomp/
41. McMahon D. (2008), "Quantum Computing Explained", John Wiley & Sons, Inc., Hoboken, New Jersey.
42. Jan-Markus Schwindt, (2017), "Conceptual Basis of Quantum Mechanics", Springer.

*Journal of Engineering Science* *Vol. XXVIII, no. 1 (2021), pp. 91 - 99*
*Fascicle* *Architecture, Civil and Environmental Engineering* *ISSN 2587-3474*
*Topic* *Architecture, Urbanism and Cadaster* *eISSN 2587-3482*

**https://doi.org/10.52326/jes.utm.2021.28(1).09**
**UDC 725(478-25)**

# STAGES OF FORMATION OF ARCHITECTURE OF CHISINAU ADMINISTRATIVE BUILDINGS

Svetlana Oleinic*, ORCID ID: 0000-0002-0133-0867

Technical University of Moldova, 168 Stefan cel Mare bd., MD-2004 Chisinau, Republic of Moldova
*Corresponding author: Svetlana Oleinic, *svetlana.oleinic@arh.utm.md*

Received: 11. 18. 2020
Accepted: 02. 05. 2020

**Abstract.** This article reveals the stages of formation of the architecture of administrative buildings in the city of Chisinau on the background of historical and economic transformations, that took place in Moldova from the late 19th to the early 21st century. The article reflects the results of analysis, which made it possible to identify nine periods of evolution of the architecture of administrative buildings from the provincial administration buildings to office and business centers. Based on specific examples, the article demonstrates the transformation of compositional techniques not only of this typological group, but also of public buildings in general, as well as stylistic changes in their architecture from eclecticism and neoclassicism, through modernism and postmodernism, to deconstructivism and high-tech.

**Keywords:** *administrative buildings, architectural form, business center, compositional techniques, compositional principles, Moldovan architecture, architectural style.*

## Introduction

In 1812, when, as a result of the Russian-Turkish wars, the territory of Bessarabia joined the Russian Empire, Chisinau, having received the official status of a city, became the center of the Bessarabian region. The construction of the city, which began in 1818 according to Ozmidov's plan, was carried out mainly on the slope above the old quarters with a chaotic layout, receiving the name of the upper city. Here the first straight and wide streets appeared and the construction of such buildings as the Metropolitanate, the Theological seminary, churches, as well as private houses of boyars, officials and merchants began. This was the first stage in the emergence of the architecture. Unfortunately, these structures have not survived without leaving any material documents in the form of drawings, measurements or photographs [1].

## The first steps

The architecture development of administrative buildings in Chisinau goes back to the end of 19-th century with the acquisition of status of a provincial city, which caused an increasing number of administrative buildings. Initially, the pan-European tendency of using

of historical neo-style forms (from Romanesque to Gothic and Baroque) was inherent in the architecture in this type of building.

The eclecticism using decoration and embellishment, fulfilled the basic architectural requirements of society at the end of the 19th century the desire for a monumental and ostentatious parade of public buildings.

The center of Chisinau was built up with administrative buildings of national importance that determined its individuality and have survived to this day: The District Court (1885, arch. Heinrich von Lonsky, Figure 1); The Revision Chamber of the Bessarabian Province (1900, arch. S. Zalessky); The Kishinev City Hall (1902, arch. M. Elladi); The Treasury Chamber (1903, Figure 2); The Provincial government of Bessarabia (1904, arch. V. Ivanitsky); The City Bank (1911, arch. M. Checkerul-Kush); and others [2 - 4].

**Figure 1.** The District Court,1885.

**Figure 2.** The Treasury Chamber, 1903.

In accordance with the urban planning doctrine, buildings were built along the red lines of the central streets, participating in formation of the block's perimeter development. Shape-formation was distinguished by its harmoniousness, strict proportions and careful drawing of details of risalits, porticoes, elegant gables, colonnades and pilasters of classical orders.

The interpretation of the facade surface was gradually changing, which, losing its flat perception, acquired complexity due to the high relief, large details of the decor, removal of the cornice, the identification of the basement, "rustication" of the wall plane, accentuation of window's sill, etc.

The First World War suspended the growth and development of the city, but in the subsequent interwar period, the construction of administrative buildings did not stop, although it slowed down: The Railway Head-office (1930`s, Figure 3.) [5].

**Figure 3.** The Railway Head-office, 1930`s.

**Soviet period of reconstruction and development**

The next wave of construction of administrative buildings covers the period of restoration and reconstruction of the city which was destroyed during the Second World War. Historic buildings were restored with the help of photos and sketches with simplification of the decor, and in the 1950's their number was significantly increased due to new construction. During this period, the concept of ensemble building in the city center dominated by buildings made in the spirit of neoclassicism, with mandatory location along the red lines of the most significant streets [2]. This provided the architectural and planning unity for the constituent parts of the city, formed in different periods. In accordance with the general plan, at the place of destroyed city center was planned a "concentrated" development of administrative buildings: The Ministry of the Interior (1949, arch. N. Gulavsky, V. Verigin, Figure 4.); The Ministry of Transport and Highways (1952, arch. S. Vasiliev, I. Eltman); The Ministry of Food Industry (1953, arch. V. Wojciechowski, P. Borisov); The Ministry of Light Industry (1953, arch. I. Shmurun); The Ministry of Agriculture (1953, arch. T. Smirnova); The Council of Trade Unions (1953, arch. R. Kurtz); The Academy of Sciences (1955, arch. V. Mednek, A. Vedenkin); The Ministry of Finance (1957, arch. V. Wojciechowski); The Ministry of Communications and General Post Office (1961, arch. V. Mednek, Figure 5.), etc [6, 7].

**Figure 4.** The Ministry of the Interior,1949.


**Figure 5.** The General Post Office (1961

Shape-formation relied on giving monumentality to structures using techniques from the arsenal of classicism: symmetrical composition, three-part articulation of the facade, semicircular windows or archivolts on the upper floor, etc. The facades of most buildings were enriched with columns, half columns and pilasters. A tectonic solution of the external walls was widely used, rusting and masonry of the first level with larger size and darker color stones, which increased the structures visual stability. Less attention was paid to the planning decision of the structures, the main principle of which was strict adherence to the symmetry of the whole composition based on the corridor system. Attempts were made to reflect in Moldavian architecture the national characteristics [8]. But this technique did not give the expected result because of the eclecticism and poor theoretical knowledge of the nature of national morphogenesis.

In 1955, a special decree of the Council of Ministers of the USSR "On eliminating excesses in design and construction" was adopted. It criticized this architecture for excessive decoration, pathos and false monumentalism [9]. Deliberate pretentiousness that does not correspond to functional and constructive requirements has thrown back the

development of architecture which does not reflect world trends. After adoption of this resolution, a new stage in development in the architecture of office buildings began on the basis of using of new design techniques which form the rigidly geometric tectonics of modernist structures.

Transformations in construction business allowed replacing of stone wall with lightweight panels and frame without additional decor. As a result, the architectural composition of buildings was changed: The Government House (1964, arch. S. Fridlin, Figure 7.); The Press House (1967, arch. S. Shoikhet, B. Weissbane); The House of Communications (1967, arch. V. Dubok); The Institute of Design Moldhyprostroy (1967, arch. R. Kurtz, R. Bekesevich, Figure 6.); The District Executive Committee (1969, arch. B. Shpak); The Tech-House (1970, arch. V. Zakharov), etc [10]. The architectural solutions for these buildings was a new approach to shaping, based on the simplicity of geometric construction, sharp lines and monochrome colors. Their composition became a reflection of the function of building and its constructive solution, finding its expression in a combination of rectangular prismatic shapes. The facades received a new design through the use of a window opening, which changed the proportions, playing the role of a decorative and constructive elements in the facade [11].

**Figure 6.** The ID Moldhyprostroy, 1967.

**Figure 7.** The Government House, 1964.

With the beginning of the implementation of the new general plan (1969), a period of increasing of artistic expressiveness in architecture began. In 1971, the city received a large financing for construction, which reflected its metropolitan significance. The first attempt was made to complicate the architectural composition and plastic of buildings facades with the help of modern structures, materials and color solutions. During the reconstruction of the city center, high-rise accents were added to the urban planning solution using expressive means of architecture [12]: The State Bank (1973, arch. B. Vaisbein, S. Shoikhet, G. Kalyuzhner); The Ministry of building materials (1974, arch. A. Kolotovkin, T. Lomova); The Central Committee of CPM (1976, arch. A. Cherdantsev); The Kishinev Committee of CPM (1977, arch. G. Solominov, Figure 8.); The House of Trade Unions (1977, arch. V. Kudinov); The Institute of History of CPM (1978, arch, A. Cherdantsev, Figure 9.); etc. The architectural composition of the buildings was unique due to construction of facade tectonics with contrasting combinations of various metric patterns in the wall plane. The idea of contrast continued in application of vertical and horizontal volumes, dark and light tones, variety of finishing materials and textures. In the composition of facades were used: large glazing planes; sun-protection structures from prefabricated modules as an independent facade decorative element [8].

**Figure 8.** The Kishinev Committee of CPM, 1977.

**Figure 9.** The Institute of History of CPM, 1978.

The buildings color was based on a nuanced monochrome or achromatic color combination.

In 1980's, the architecture of administrative buildings was dictated by the reconstruction of the city center using high-rise point buildings [12]. The design of deep-spatial compositions led to the rejection of the frontal perception of buildings, creation of all side views and development of recreation zones around them. The city center was enriched with high-rise administrative buildings - urban accents: The Publishing House (1980, arch. V. Zaharov, L. Hoffman); The Ministry of Agriculture (1980, arch. V. Weissbein, S. Shoihet, A. Chmyhov, Figure 10.); The Ministry of Communications (1983, arch. V. Shalaginov, A. Kireev, N. Dorofeev, S. Muhin); The Supreme Council (1989, arch. Y. Tumanyan, V. Yavorsky, A. Zaltsman, Figure 11.). etc. The construction of buildings using the new monolithic reinforced concrete technology was reflected in their appearance with vertical divisions.

**Figure 10.** The Ministry of Agriculture, 1980.

**Figure 11.** The Supreme Council, 1989.

**Search for "independent" architecture**

The declaration of independence of Republic of Moldova and socio-economic transformations affected the development of Moldavian architecture [13, 14]. Due to the difficulties of financing new construction, more attention was paid to the reconstruction and adaptation of buildings to the new functions. Modernization was carried out both in the internal layout of buildings, and in appearance, which received a modern interpretation. At this stage, a small number of administrative buildings with the tendencies of postmodernism were built: The Moldindconbank (1995, arch. V. Modyrka, Figure 12.); The

Embassy of Russian Federation (1999, arch. G. Zhinkin, Figure 13.); The Petrol-bank (1990's), etc.


**Figure 12**. The Moldindconbank, 1995.

**Figure 13.** The Embassy of RF, 1999.

In search of originality and uniqueness of each object, architects sought to aestheticize the image of administrative buildings with the help of new architectural techniques. At the same time, the construction of small business objects in the city center in the form of an "insert" was rarely associated with the existing buildings in terms of scale, style, and color. The violation of organic perception in the urban environment was exacerbated by the typological mismatch of new office buildings, which looked like rural houses. In addition, the adaptation of residential spaces of the ground floors to offices led to modification of building's facades, which also negatively affected the perception of their integrity and harmony [15].

A new round in development of architecture of administrative buildings can be attributed to the 2000's. This led to appearance of business and office centers that became typological leaders among public buildings, in their style and technical equipment corresponding to the level of development of modern architecture [16]: The Office center ASCOM Group (2013, arch. S. Garkonitsa); The Headquarters Union Fenosa S.A., (2000's, Figure 14.); The Office center Lunedor (2012); Business center PANORAMA (2015, arch. V. Galchinsky, Figure 15). The architectural shaping of business centers, built on the principles of integrity and laconicism, has become more independent from construction structure and functional zoning.

**Figure 14.** The Union Fenosa S.A., 2000's.


**Figure 15.** BC PANORAMA, 2015.

A large number of discussions caused the appearance of the first "A" class business centers, the architecture of which, reflecting the logic of deconstructivism and hi-tech, is the embodiment of stylistic antagonism with the existing urban environment: The BC

Accent Business Park (2007, arch. G. Telpiz, Figure 16.); The BC SKYTOWER (2007, arch. G. Telpis, Figure 17.); The BC Le Roi (2008, arch. G. Telpis, Figure 18.). Thanks to new proportions of volumes, modern finishing materials and a bright colors, business centers have come into conflict with the surrounding buildings and begin to play the dominant role in architectural and urban development [17].

**Figure 16.** The BC Accent Business Park, 2007.

**Figure 17.** The BC SKYTOWER, 2007.

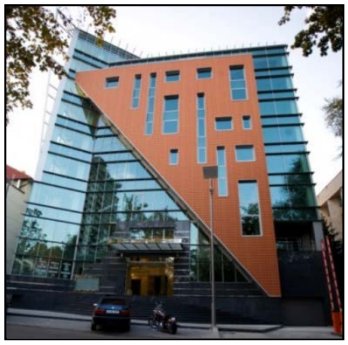

**Figure 18.** The BC Le Roi, 2008.

At the same time, a number of small-rise office buildings appeared, complementing the existing environment and showing a combination of historical and modern compositional techniques: The LUKOIL Office (2002, arch. G. Telpis); The CRIS Registru Office (2000's); The Global Business Center (2011); The Office complex on st. A. Pushkin (2009, arch. D. Kulikov); The INFOTAG News Agency (2000's, arch. G. Zhinkin), etc. [15]. Some buildings, having lost their relevance, after reconstruction received a new function, together with the reorganization of the internal space received an modernized appearance: The BC KENTFORD (1978, arch. A. Shkarupa. reconstruction 2000`s, Figure 19.); The BC JSC IPTEH (1974; reconstruction 2012, Figure 20.); The CB Mobiasbanca - Groupe Société Générale, S.A. (1948, arch. V. Verigin, reconstruction 2002, arch. Telpiz); and etc.

Today, contradictory opinions of architects and urban planners, on the one hand, approve the using of new compositional techniques, laconic shaping, bright colors and changes in the buildings proportions; but on the other hand, they try to preserve the historical environment, human scale and unique flavor of the city [18]. Nevertheless, supporters of both opinions understand that the architectural image of Chisinau, in accordance with the law of continuous development, cannot remain unchanged [19].

**Figure 19.** The BC KENTFORD, 1978.


**Figure 20.** The BC JSC IPTEH,1974.

**Conclusions**

The analysis of development of architecture of Chisinau modern administrative and office buildings from eclecticism and neoclassicism to modernism, postmodernism, deconstructivism and hi-tech - demonstrates the constant search by Moldovan architects for optimal compositional solutions designed in line with world architectural trends, but limited by local conditions and social-economic opportunities.

The process of formation and development of the architecture of Chisinau administrative buildings took place in various historical conditions, predetermined by the course of socio-economic, scientific and technical transformations. The analysis of the evolution of the architecture of this typological group of buildings revealed the following historical stages of development:

I. 1812-1874 (Chisinau received the status of a city and became a center of the Bessarabian region) - the origin of the architecture of administrative buildings;
II. 1874-1914 (Chisinau became the center of the Bessarabian province) - the formation of the architecture of administrative buildings;
III. Interwar period 1918-1941 (period of passive urban construction) - the period of operation of existing administrative buildings;
IV. Post-war period 1945 – 1950`s (period of restoration of the city, destroyed during the war) - reconstruction of ruined administrative buildings, massive construction of public buildings;
V. Late 1950`s -1960`s (period of expansion of urban areas) - the “fight against excesses” and decor in the architecture of administrative buildings, industrialization of construction production;
VI. 1970`s (period of active construction of residential neighborhoods) - the increasing of the architecture artistic expression, reconstruction of the city center and construction of new administrative buildings;
VII. 1980`s (period of city center reconstruction and improvement of residential areas) - the application of various stylistic techniques in the architecture of administrative buildings based on high-rise point construction.
VIII. 1990`s (period of reconstruction of public buildings) – the adaptation of administrative buildings for the new function of business and management.
IX. 2000`s (period of qualitative change and rapid development of architecture) - construction of large business centers and office buildings.

During the compositional analysis of the administrative buildings architecture only the buildings that have survived to this day were considered. Their architecture can have a significant impact and become the starting point for choosing the style, scale, tectonics, compositional techniques and color scheme of future buildings.

**Acknowledgements**

The author would like to thank Professor Tamara Nesterova, Ph.D. academic supervisor, for the guidance and academic support during the past recent years. Her valuable advice was instrumental for completion of the research.

**References**


1. Ciocanu S. *The city of Chisinau: beginnings, urban development, churches (15th-19th centuries*). Chisinau: Ed. Cartdidact, 2017, 280 p. ISBN 978-9975-3180-0-6.
2. Nesterov T., Gangal B., Rîbalco E. *The historical center of Chisinau at the beginning of the XXIst century. The repertoire of architectural monuments*. Chisinau: Edition ARC, 2010. 568 p. ISBN 978-9975-61-599-0.
3. Historical Center of Chisinau - the cultural heritage of the capital. Architectural monuments in the Historic Center of Chisinau. [date of access 15.06.2020]. Available: http://www.monument.sit.md//
4. Register of monuments of the Republic of Moldova protected by the state, approved by Parliament Decision no. 1531-XII of June 22, 1993, In: *Monitorul Oficial al Republicii Moldova* no. 15-17, 02.02.2010. [date of access 02.09.2018]. Available: https://www.legis.md/cautare/getResults?doc_id=7151&lang=ro.
5. Nesterov T. The architecture of the interwar period of Chisinau in search of artistic identity. In: *The Identities of Chisinau. Third edition, B*. Chisinau, Series IDN, C6. Chisinau: Edition ARC, 2016, pp. 137-144.
6. Rusu D., Mitrea V., Nesterov T., Nemtsianu R. R. *Modernist socialist architecture - Romania and the Republic of Moldova 1955 - 1989/91*. Architecture guide. Bucharest: B.A.C.U., 2018. ISBN 978-973-0-27899-6.
7. Register of historical monuments of local category in Chisinau, OBJECT no. 2994, annex no. 1, approved by the Municipal Council 11.12.2014. [date of access 02.09.2018]. Available: https://www.chisinau.md/libview.php?l=ro&idc=403&id=10260.
8. Smirnov V. *Urban planning of Moldova*. Chisinau: Kartya Moldoveneaske, 1975, 147 p.
9. Bognibov E. *Ways of development of architecture of Soviet Moldavia 1940 – middle 1970s.*: Ph.D. thesis. Moscow, 1976.
10. Bognibov E., Dumitrashku P. *Architecture of Chisinau before the 60s. XIX century*. Chisinau: MoldNIITEI, 1997, 44 p.
11. Kolotovkin A., Shoykhet S., Eltman I. *Architecture of Soviet Moldavia*. Moscow: Stroyizdat, 1987, 320 p.
12. Bendersky B. *City and time. Chisinau architecture of the 18th - 20th centuries*. Chisinau, 2004.176 p.
13. Declaration on the sovereignty of the Republic of Moldova, June 23, 1990. [date of access 03.11.2019]. Available at: https://www.gorby.ru/userfiles/moldova.pdf.
14. Declaration of independence of the Republic of Moldova, August 27, 1991. [date of access 3.11.2019]. Available at: http://www.presedinte.md/rus/declaration.
15. Oleinic S. Compositional trends in modern architecture of business buildings in the historic center of Chisinau. In: *ART: Series Visual Arts, Fine Arts, Architecture. New series. vol. I (XXII), nr.1, B*. Chisinau: ASM, IPC, Arts Study Center, 2013, 176 p., pp. 152-160, ISSN 1857-1050.
16. Gelfond A. *Business center as a new type of public building*: Ph.D. thesis. Moscow, 2002. 297 p. RGB OD, 71 02-18 / 3-5.
17. Oleinic S. The compositional aspects of the architecture of business buildings in Chisinau built in the last decade. In: *ART: Series Visual Arts, Fine Arts, Architecture*. Chisinau: ASM, IPC, Arts Study Center, 2012, 174 p., pp. 97-102, ISSN 1857-1042.
18. The Law of the Republic of Moldova "On the Protection of Monuments", June 22, 1993 No. 1530-XII. In: *Monitorul Oficial al Republicii Moldova*, Nr. 15-17, from 02.02.2010, article no: 24.
19. Nesterov T., Oleinic S. Some considerations regarding the critique in architecture. In: *ARTA: Visual Arts Series, Fine Arts, Architecture. New series. vol. XXVI, no. 1, B*. Chisinau: ASM, IPC, Arts Study Center, 2017, 160 p., pp. 140-146, ISSN 2345-1181.

*Journal of Engineering Science* *Vol. XXVIII, no. 1 (2021), pp. 100 - 110*
*Fascicle* *Architecture, Civil and Environmental Engineering* *ISSN 2587-3474*
*Topic* *Civil Engineering and Management* *eISSN 2587-3482*

**https://doi.org/10.52326/jes.utm.2021.28(1).10**
**UDC 656.71(458.2)**

# THE PECULIARITIES AND IMPACTS OF AIRPORTS: THE CASE FOR MALTA INTERNATIONAL AIRPORT

Lino Bianco[1, 2]*, ORCID: 0000-0001-8779-2351

[1]*University of Malta, Msida, MSD 2080, Malta*
[2]*University of Architecture, Civil Engineering and Geodesy, 1 Hristo Smirnenski Blvd., Sofia 1164, Bulgaria*
*Corresponding Author: Lino Bianco, *lino.bianco@um.edu.mt*

Received: 01. 12. 2021
Accepted: 02. 18. 2021

**Abstract.** The small-to-medium sized Malta International Airport (MIA) is the only airport in Malta, especially in terms of its footprint, and is considered one of the world's most scenic landings, according to a 2016 poll. The annual passenger turnover is approximately 16 times the country's population. MIA's unique features include its proximity to the urban conservation area of Luqa, as well as that town's other residential and business facilities, and also to the southern coast of Malta and the unique ecological habitats it supports. Its impacts range from noise to atmosphere pollution and, potentially, pollution of the coastal waters, in the eventuality of an air traffic accident. On the basis of the national strategic vision that Malta evolves into an expanding hub in the centre of the Mediterranean, significant investment is earmarked for MIA, including initiatives impacting security, the environment and energy.

**Keywords:** *airport, planning policy, tourism policy, heritage protection, nature protection, Luqa, Malta.*

## Introduction

For long-haul travel, air transport is preferred as it is usually the fastest mode of travel compared to car, bus and train – even when affected by delays – and the safest. It is vital for the tourism industry [1-2], especially regarding access to remote locations such as islands. Since the mid-1990s, there has been a rapid growth in air transport in all 27 European Union Member States and airports are being transformed into hubs for both international and domestic flights [3]. Mashhoodi and van Timmeren [4] classified European airport regions in five typologies: urban airports, urban periphery airports, agricultural-area airports, natural-area airports and remote airports (Table 1).

Malta International Airport (MIA) (Figure 1) is a small-to-medium sized facility and the only airport in the Maltese archipelago developed largely after the Second World War era. It is neither a major airport nor a large airport region, as defined by Mashhoodi and van Timmeren [4]. The country of Malta is the smallest Member State of the EU, having a total surface area of 316 km², the main inhabited island being Malta itself. Although overwhelmingly referred to by foreigners who have never travelled to Malta as being

located in 'La Valletta', Valletta being the island's capital city, MIA administratively falls within the confines of the town of Luqa. The island of Malta (as opposed to the country) is approximately 246 km$^2$ in area, with a length and width of 27 km and 14.5 km respectively.

*Table 1*

**Typologies of airport regions of Europe (After [4])**

| Airport typology | Characteristics | Example/s |
|---|---|---|
| Urban | Adjacent to high concentrations of urban land use and population | Geneva, Zurich, Graz |
| Urban periphery | Adjacent to urban areas and high concentration of industrial and leisure | Berlin, Bordeaux, Malaga |
| Agricultural-area | Adjacent to agricultural land use | Paris, Barcelona, Amsterdam |
| Natural-area | Close proximity to natural areas and distance from leisure, industry and major road network | Milan |
| Remote | Located at a long distance from all land uses and population centres | London, Nuremberg, Belfast |

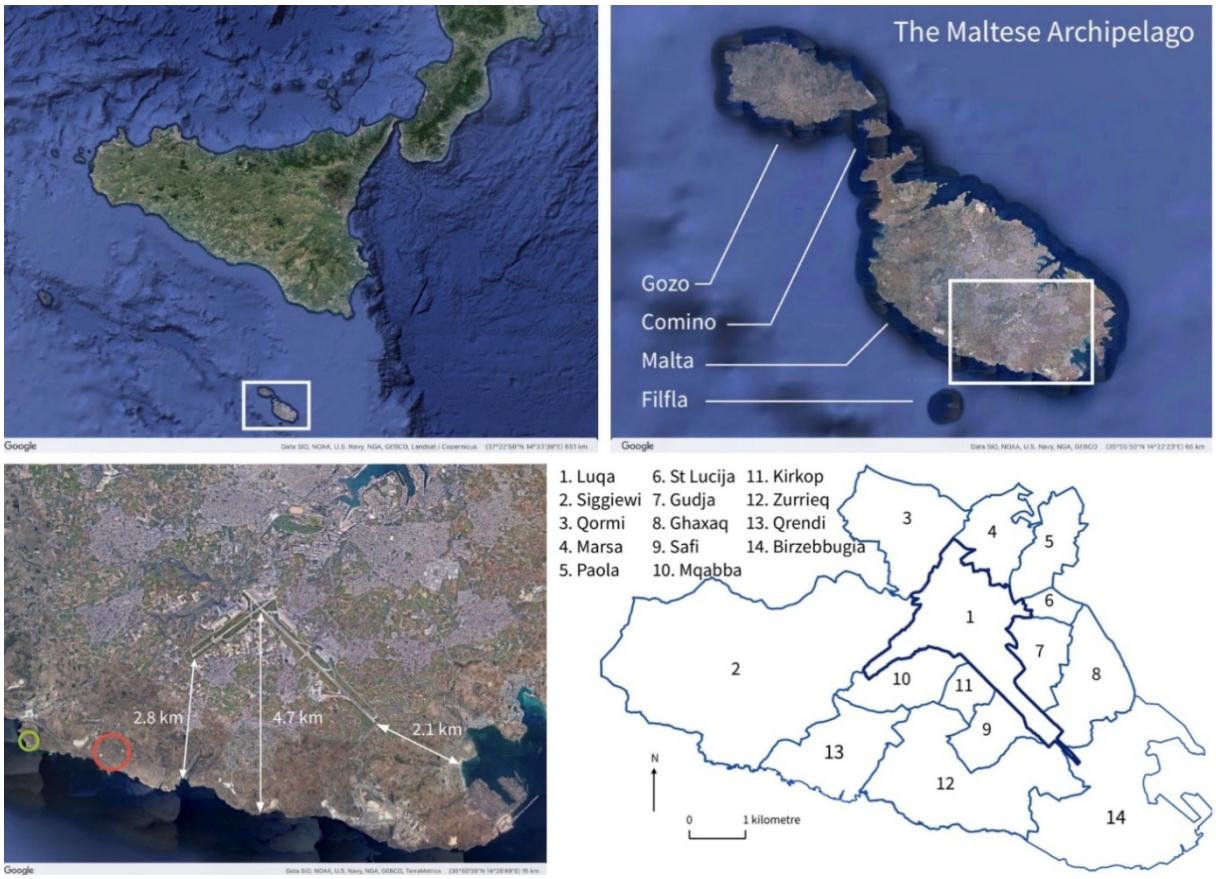


**Figure 1.** Site location (online version is in colour) – outlined in white – of the Maltese archipelago (top, left), Malta and its dependencies (top, right); the location of MIA with distances from the coast (bottom, left) – Ħaġar Qim and Mnajdra Neolithic Temples and Lapsi Reverse Osmosis Plant are circled in red and green respectively (© Google Earth); the administrative boundaries of various Local Councils - including Luqa (bottom, right).

Due to this fairly modest size, virtually all the coastline of the island is potentially exposed to the impacts of MIA (Figure 1, bottom left). Given that Luqa is located in the south of the island, the coast most exposed to risk is along the southern one, which touches the confines of the local councils of Birżebbuġa, Qrendi, Siġġiewi, and Żurrieq (Figure 1, bottom right).

In 2019, 7.3 million passengers used MIA [5]. This figure is nearly 16 times the resident population of the island of Malta which stood at 460,171 at the end of 2018 [6, p. 15]. This represents a 7.4% increase in air passengers over 2018, peaking, with just over 823,000 passenger movements, in August, at the height of the 'festa' or village feast season [5].

This paper addresses the characteristics of MIA and its impacts on the locality of Luqa and the wider region, characterised notably by a coastline of ecological and ornithological importance. These findings are supported by references to policies contained in relevant national development planning documents which aim to improve MIA whilst respecting the natural environs. Furthermore, it highlights current research and national investment to render the airport EU compliant.

**Methodology**

To tackle the themes outlined above, use was made of existing literature on the history of Luqa and its airport, together with a number of official sources, notably:

1. National and local planning policies of the Planning Authority (PA), the national regulator for development planning in Malta, which was renamed Malta Environment and Planning Authority (MEPA) during the years 2002–2016 as when it was merged with the Environment Protection Department;
2. Official statistics issued by the National Statistics Office, Malta;
3. MIA press releases; and
4. Reports of ENGO BirdLife International.

**Luqa and its airport**

Aviation in Malta dates back to the 1920s when the island was a fortress colony of Britain. Given its geographical position at the centre of the Mediterranean, and predicting the future importance of aerial warfare, the British Government developed three main airfields. Ta' Venzja, known as Ta' Qali (or Ta Kali or Takali) by the Royal Air Force, in heartland Malta, was the location of the first civil airfield. It was followed by those at Ħal-Far (used by the Fleet Air Arm) and Luqa. The latter was less damaged than the others by Axis bombardment during Second World War. Unlike Ta' Qali and Ħal-Far, Luqa airport was not prone to flooding.

The first civil terminal was inaugurated in Luqa in 1958. In 1977, a longer runway was constructed to accommodate an anticipated increase in air traffic, while the air terminal was refurbished and extended until it was eventually superseded by the present terminal, which was inaugurated in 1992 (Figure 2). MIA was established as the public limited company solely responsible for operating the air terminal in 1991. Its remit also included the operations and management of air traffic control, an activity hived off at the end of 2001 and transferred to Malta Air Traffic Services, an autonomous government entity [7]. MIA has two main runways with the area control tower located in between. The runways, RWY 14-32 and RWY 06-24, are set perpendicular to one another and international air traffic control operations are managed 24/7.

**Figure 2.** Terminal of MIA (online version is in colour): as at present (left), and as viewed from the side of the runway (right) (© Alessandra Bianco).

Under the terms of the *Local Councils Act* [8], the town of Luqa includes the rapidly expanding hamlet of Ħal-Farruġ, originally a medieval settlement which includes a historic chapel that was partly destroyed to make way for airport extensions. The constituency of Luqa, which measures circa 6.75 km$^2$, is the major inland locality forming part of the *South Malta Local Plan* [9, pp. 99-104]. It is predominantly rural in character (6.25 km$^2$ is countryside). Micallef [10] offers a dated but detailed study of this locality, while more recent but brief descriptions are provided by Fiott [11] and Guillaumier [12]. Luqa's urban core still retains the characteristic vernacular organic street pattern (Figure 3, left) with a baroque-style parish church in the main square (Figure 3, right), which was rebuilt after damage in the Second World War blitz. The urban areas (0.48 km$^2$) are predominantly residential in nature.

**Figure 3.** Luqa (online version is in colour): orthophoto of the urban area (left) (© Planning Authority, Malta), the position of photo and church shown in Figure 3 right, is marked by ▲ and + respectively; the main street, named after the patron saint of the town, leading to the main square (for position of photo see Figure 3 left) (© Alessandra Bianco).

Luqa forms part of the southern harbour region. The latest demographic review, based on the 2011 (November) census, estimates its population on 31 December 2014 at 5,714 [13, p. 14] thus reversing the depopulation trend experienced in the preceding years. A decade earlier, in 2004, it stood at 5,195 [14, p. 15] whilst in 2001 it was 5,456 [15].

Important institutions located within the Luqa Local Council (LLC) area include St Vincent de Paule Residence, the main state home for the elderly in Malta, and the Research and Agricultural Development Centre at Għammieri. Other facilities include The Malta College of Arts, Science and Technology Agribusiness Institute, the main premises of the Water Services Corporation and a medium-sized industrial park.

**The southern coast of Malta**

In the *PrivateFly Best Airport Approaches 2016* poll conducted in early 2016, MIA was listed as one of the world's most scenic landings. The CEO of PrivateFly, Adam Twidell, himself an experienced pilot, commented that: "Flying into Malta is a truly special experience - it's a tiny island landing that packs a big punch. There is so much to take in. Without being hectic, the landscape changes from coast, to farmland, to the historic city of Valletta. It's like flying into a Picasso painting" [16].

The geology and geomorphology along the southern coast of Malta are shown in Figure 4. Lower Coralline Limestone cliffs, formed in the Oligocene, characterise most of this coast. Under the *Structure Plan for the Maltese Islands* [17], the cliffs are scheduled by the PA as Level 2 Areas of Ecological Importance and Areas of High Landscape Value [18]. The geological formations are horizontally bedded. Where the overlying Globigerina Limestone occurs, weathering is more pronounced and exhibits diagnostic weathering features mapping out the varying lithostratigraphic beds.

The Lower Coralline Limestone formation forms an extensive aquifer extending, at sea-level, beneath most of the island. Given the littoral character of the southern coast, no special protective measures to conserve the integrity of this aquifer are necessary as the continuous seawater intrusion reduces the quality of the groundwater along coastal zones. Thus, any potential impact of MIA, if applicable, would be negligible. These areas lie outside the designated water protection areas as established by the Water Services Corporation, the former body protecting the islands' groundwater resources since 1992. In 2000, the Malta Resources Authority became the authority responsible for managing and protecting the islands' aquifers. The sea-cliffs of southern Malta support maritime rupestral vegetation assemblages typical of coastal cliffs. Since they are largely inaccessible, they are still in pristine condition and provide an ecological refuge to many species of flora and fauna, a large number of which are endemic [19] and thus are of significant ecological, biogeographical and conservation value.

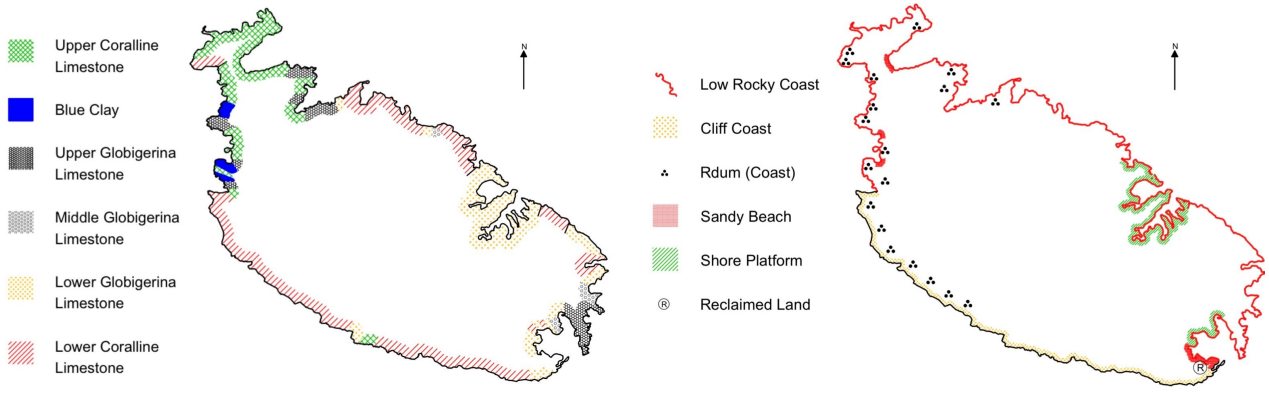


**Figure 4.** Malta: coastal geology (left) and geomorphology (right) (online version is in colour).

There are two species of Procellariidae that nest in the Maltese Islands: Cory's shearwaters (*Calonectris diomedea diomedea* [Scopoli], Maltese Ċiefa) and Levantine shearwaters (*Puffinus puffinus yelkouan* [Acerbi], Maltese Garnija). The southern coast supports the largest concentration of Cory's shearwaters in Malta, with more than 1,000 breeding pairs, along with more than 200 pairs of Levantine shearwaters. The breeding population of Cory's shearwaters in the Maltese Islands is estimated at around 7,000 breeding pairs, distributed along the southern coast of Malta, Gozo, Comino and Filfla. The southern cliffs between Bengħajsa point and Għar Lapsi support the largest concentration on mainland Malta [20]. Back in 1994, due to a large decline in numbers, Cory's shearwaters were designated as Category 2 – vulnerable according to *Species of European Conservation Concern* [21]. Since then, numbers have recovered significantly, and they are currently listed as a species of 'least concern' according to *The IUCN Red List of Threatened Species* [22]. At a more local level, the species was designated as vulnerable with a restricted distribution in the Mediterranean. The Levantine (or Yelkouan) shearwater has a similar national status as Cory's Shearwater. *The IUCN Red List of Threatened Species 2018* [23] has them marked as vulnerable.

Further to pristine, ecologically rich, valleys such as Wied iż-Żurrieq (Figure 5, left), a considerable number of archaeological and historical remains are located along the southern coast of Malta. These reflect how the island's history is intertwined with its natural configuration [19]. Amongst these remains are Ħaġar Qim (Figure 5, right) and Mnajdra Neolithic Temples (Figure 1, bottom left), acknowledged as World Heritage sites by UNESCO [24].

**Strategic planning policies**

The strategy of the PA with regards to Luqa is to protect its rural character whilst making provision for recreational facilities, in particular within the limits of the medieval settlement of Ħal-Farruġ. With respect to the airport, the PA's strategy is for MIA to develop into a regional hub and consolidate various activities within its existing footprint.

Strategic planning policies for the Luqa area are included in the *South Malta Local Plan* [9]. Policy SMLU 07 states that "For the area designated as the Malta International Airport Master Plan Area, as indicated in the Luqa Airport and Environs Policy Map LU 3, a Master Plan is to be submitted to MEPA by the Malta International Airport indicating the various developments and uses proposed for this area which may include facilities relating to airport operations, retail and commercial facilities, entertainment facilities, parking, as well as an element of tourist accommodation".

The *Strategic Environmental Assessment: Environment Report* [25], prepared as part of Strategic Plan for Environment and Development, which replaced the *Structure Plan for the Maltese Islands* [17], makes only passing reference to the airport. It states that there is a regulation governing noise emissions from airports (Paragraph 4.8.2) and declares, in Thematic Objective 12, that (i) the land around the airport must be safeguarded for future expansion of aviation-related activities and (ii) the transport network serving the airport must be satisfactory to accommodate such an expansion.

Given the presence of MIA, non-urban areas, which account for approximately 93% of the territory of the LLC, are taken up by facilities associated with airport operations: namely, runways, passenger terminals, airport administrative blocks, aircraft workshops and ancillary facilities.

**Figure 5.** Wied iż-Żurrieq, one of the pristine, ecologically rich, valleys in Malta (left); dated aerial photo of Ħaġar Qim Neolithic Temples (right) (*Hagar Qim* by peuplier is licensed under CC BY 2.0) [26], (online version is in colour).

Future development planning proposals include a new air approach route for the airport and commercial and recreational facilities. Furthermore, due to the presence of the airport, Luqa is subject to significantly high traffic levels from localities south of the airport as well as from the central and northern parts of the island and from Malta's sister island of Gozo.

Neither general nor specific policies related to tourism in Luqa are contained in the *South Malta Local Plan*, despite the fact that a number of archaeological and historical remains occur within the territory of the Local Council. For example, Roman catacombs that interfered with the various developments and upgrades of airport facilities were destroyed and/or made inaccessible. The plan does identify various archaeologically sensitive areas, some of which occur within the airport area and are included in Maps LU7 and LU8 [27]. These historical remains include chapels and other architectural elements, as well as works of art.

Cultural heritage, both in terms of architecture and folk traditions, has long been noted by the LLC as a source of identity for the locality. Luqa's architectural heritage is important, as are traditional activities such as band clubs and the village 'festa'. The Local Council supports such assets which have expanded over a number of decades because it understands that such traditions and practices should complement and not compete with economic growth. Accordingly, LLC developed a policy whereby tourism is encouraged and sustained. Tourism is not seen by the Local Council as an end in itself but as a means to an end, namely, to sustain and improve on the otherwise healthy socioeconomic fabric of the locality.

While accepting that MIA cannot be separated from Luqa, since the latter encompasses the former while giving it distinctiveness, LLC is aware of the environmental impacts of noise and air pollution from air traffic on the socioeconomic sphere and cultural heritage of the locality. As elsewhere, awareness is growing about environmental and health issues that are taking their toll on the local community. The Local Council's response is to take a proactive stand vis-à-vis present and future airport area planning strategies, to ensure that the environmental conditions and health of the community are improved whilst encouraging the sustainable development of the area's tourism potential as a means of sustaining this identity.

**Unique features and impacts of MIA**

Aircraft activity involves the arrival, parking and disembarkation of passengers, the unloading of baggage and cargo, and maintenance activities. Prior to departure, maintenance and engine testing is carried out, after which the passengers board, baggage is loaded and the plane refuelled. Thus, the main impacts of airport activity go beyond noise, vibration and related issues, to include light, air, soil and water pollution.

The arrival and departure of an aircraft emits noise and has transboundary impacts on air quality due to the generation of air pollution throughout the flight. Once an aircraft lands, it parks, emitting further noise and exhaust gases. Any handling vehicles required for baggage loading, passenger dis/embarkation, cleaning and maintenance works generate exhaust fumes and noise. The road traffic to and from the airport also has an impact on air quality. Runway activity is associated with light pollution, especially in view of Luqa's rural location. The maintenance of airport's external facilities – the two runways, aprons, fuel depots, aircraft maintenance garages and landscaped or turfed areas – also has impacts on the environment, as does the provision of energy for runway lighting and fire drills. The airport terminal is a centre of activity which continuously consumes energy and water, and generates waste.

Noise impacts negatively on both residents and birds, and light pollution may interfere with the night sky, affecting the circadian rhythms of wildlife and potentially deterring shearwaters from reaching their colonies sited along the coastal cliffs [28]. Light pollution also has the effect of attracting moths and insects, thus reducing food sources for bats [29] and other night-time predators that rely on them. Due to the fact that Luqa airport is a protection zone where bird trapping and hunting is not permitted, and because Malta is located on the main migratory route across the Central Mediterranean, birds often seek shelter within the precincts of MIA. This in itself carries its specific risks; for example, flocks of starlings *(Sturnus vulgaris*, Maltese Sturnell) or gulls (*Larus sp*., Maltese Gawwi) often interfere with air navigation and pose a potential hazard to aircraft, especially during take-off.

Located in the town of Siġġiewi, the Lapsi Reverse Osmosis Plant lies along the coast just south of the airport (Figure 1, bottom left). If an air crash occurred at sea in the vicinity of this plant, there is a high probability of sea contamination, which would have a severe negative impact on the production of potable water. This reverse osmosis plant is the second largest desalination plant in the Maltese archipelago, contributing nearly a tenth of the supply of potable water.

**Research and investment**

Local and foreign studies have been undertaken on how to reduce the impact of flights on the environment through improved flight efficiency. A fairly recent one by Micallef et al [30] shows that fuel burn and CO2 emissions by inbound flights can be reduced if other approach routes are exploited for MIA's main runways, a theme which is being considered in contemporary literature relating to flight trajectory optimization (e.g., [31]). This suggestion is in line with MIA's corporate social responsibility agenda. Other considerations include using electric vehicles to tow airplanes onto the runway, instead of them taxiing powered by their own, highly polluting engines. At present, research is being undertaken at the University of Malta for engineless aircraft taxiing through Situation Awareness and Traffic Management for Engineless Taxiing (SAMET) project [32].

A number of measures taken by MIA to improve sustainability, ranging from energy-saving lighting and air conditioning to the installation of more efficient sanitation systems, led to the airport lowering its greenhouse gas emissions by 12% and its total water consumption by 11.6% in 2018 [33]. In early 2020, MIA announced a multi-million euro investment in terminal expansion which, further to the physical increase of its footprint, will include "smart technologies, including a new building management system to allow for energy and water management optimisation, and better insulation [...] which will play an important role in the company's journey towards the achievement of carbon neutrality" [34].

The latest investment by MIA involves upgrading its security and IT infrastructure. A multi-million EU-financed investment is aimed at tightening controls and data sharing at Malta's external borders through the EU Travel Information Authorization System (ETIAS). In a press conference announcing the project, the Home Affairs Minister stated: "Malta's borders are some of the most frequently crossed in the EU, so it is essential that our frontier management systems are up to scratch, both for the sake of our national security as well as the safety of the EU" [35].

**Conclusions**

A small-to-medium–sized facility which dates back to the late 1950s, Luqa airport is neither a major airport nor a large airport region. Located near the southern coast of Malta and in close proximity to the residential areas of the town of Luqa, a number of conclusions can be drawn with regarding MIA.

With respect to the southern coast of Malta:

1. impacts on the aquifer are negligible;
2. the maritime rupestral vegetation assemblages typical of coastal cliffs are not affected;
3. the two species of Procellariidae – Cory's shearwaters and Levantine shearwaters – may be negatively affected; and
4. given that a major reverse osmosis plant is located along this coast, in the case of an air crash at sea, contamination of sea water would have a significant negative effect on national water production.

With respect to the locality of Luqa:

1. aircraft noise impinges negatively on locals and birds;
2. light pollution generated at MIA negatively interacts with circadian rhythms of wildlife and is likely to deter shearwaters from reaching their colonies along the cliffs; and
3. flocks of starlings or gulls, which often interfere with air navigation, pose a potential hazard to aircraft.

In terms of national planning policies, MIA will remain at Luqa for decades to come. Environmental planning research is being undertaken to reduce the impacts of aircraft navigation on the natural and residential environs. Measures to improve sustainability and lower greenhouse gas emissions are being undertaken. Furthermore, significant investment, in part EU-financed, is projected in the immediate future to ensure an EU-compliant strategy for security and IT infrastructure.

MIA is a top contributor to the local economy. It supports not only the physical and economic wellbeing of its employees but also the social and environmental initiatives of surrounding localities. Some initiatives were taken within the local community of Luqa

through the Malta Airport Foundation, which has partnered with NGOs on various marine conservation projects [5].

**Acknowledgments.** This article is based on two presentations by the author, as the environmental planning consultant of Luqa Local Council, at the first town-twinning conference entitled 'Airport Cities in the Union' held on 12-15 October, 2005 in Fiumicino, Italy. Joanne Bianco Muscat, an environment planning consultant, assisted the author in the preparation of the aforementioned presentations. The author would like to express his gratitude to Alessandra Bianco for granting him permission to reproduce Figures 2, 3 right and 5 left.

**References**

1. Barros C.P. Airports and tourism in Mozambique. In: *Tourism Management*, 2014, 41, pp. 76-82.
2. Castillo-Manzano J.I. Determinants of commercial revenues at airports: Lessons learned from Spanish regional airports. In: *Tourism Management*, 2010, 31, pp. 788-796.
3. Merkisz-Guranowska A., Bieńczak M., Kiciński M., Zmuda-Trzebiatowski P. Location of airports – selected quantitative methods. In: *LogForum*, 2016, 12(3), pp. 283-295.
4. Mashhoodi B., van Timmeren A. Airport location in European airport regions: Five typologies based on the regional road network and land use data. In: *Data in Brief*, 2020, 29, 105317.
5. Malta International Airport. *Record 7.3 million passengers passed through Malta International Airport in 2019*. [online]. 08.01.2020. [accessed 28.11.2020]. Available: https://www.maltairport.com/record-7-3-million-passengers-passed-malta-international-airport-2019/
6. National Statistics Office. *Regional Statistics Malta: 2020 Edition*. Valletta, National Statistics Office. [online]. 2020. [accessed 15.11.2020]. Available: https://nso.gov.mt/en/publicatons/Publications_by_Unit/Documents/02_Regional_Statistics_(Gozo_Office)/2020/Regional_Statistics_Malta-2020%20Edition.pdf
7. Cremona J. *The Privatisation of the Malta International Airport and its Financial Implications*. B.Comm. (Hons) Dissertation. Malta: University of Malta, 2011. [accessed 27.11.2020]. Available: https://www.um.edu.mt/library/oar/bitstream/123456789/3467/1/11BACC034.pdf
8. Laws of Malta. *Local Councils Act*, 1993.
9. Malta Environment and Planning Authority. *South Malta Local Plan*. Marsa, 2006, Vol. I.
10. Micallef G. *Ħal Luqa: Niesha u ġrajjietha*. Zabbar, Malta: Veritas Press, 1975.
11. Fiott C. *Town and Villages in Malta and Gozo; Part 2: The South*. Rabat, Malta: Conventual Franciscans, 1996.
12. Guillaumier A. *Bliet u Rhula Maltin*. Vol. 1, Sta Venera, Malta: Klabb Kotba Maltin, 2002.
13. National Statistics Office. *Demographic Review 2014*. Malta: Government Printing Press, 2016.
14. National Statistics Office. *Demographic Review 2004*. Malta: Government Printing Press, 2005.
15. National Statistics Office. *Demographic Review 2001*. Malta: Government Printing Press, 2002.
16. Malta International Airport. *Malta International Airport tops list of world's most scenic airport landings*. [online]. 2016. [accessed 28.11.2020]. Available: https://www.maltairport.com/malta-international-airport-tops-list-worlds-scenic-airport-landings/
17. Planning Services Division. *Structure Plan for the Maltese Islands: Draft Written Statement and Key Diagram*. Malta: Ministry for Development of Infrastructure, 1990.
18. Department of Information. Government Notice GN_400_1996. In: *The Malta Government Gazette*, 25 June 1996, pp. 4116-4120.
19. Planning Authority. *Coastal Strategy Topic Paper - Final draft*. Floriana, 2002. [accessed 15.11.2020]. Available: https://discomap.eea.europa.eu/map/Data/Milieu/OURCOAST_032_303_MT/OURCOAST_032_303_MT_Doc2_MTCoastalStrategy.pdf
20. Borg J. Ornithology. In: Lino Bianco & Associates, ed *Environmental Impact Statement: Tuna Penning Farm off Benghajsa Reef, Malta*. Malta, 2001, pp. 2.88-2.92.
21. Tucker, G.M., Heath, M.F. (ed). *Birds in Europe: Their Conservation Status*. BirdLife Conservation Series No. 3. Cambridge, United Kingdom: BirdLife International, 1994.

22. Birdlife International. *Calonectris diomedea. The IUCN Red List of Threatened Species 2015:* e.T45061132A66727878 [online]. 2015. [accessed 21.12.2020]. Available: https://www.iucnredlist.org/species/45061132/66727878
23. Birdlife Interntional. *Puffinus yelkouan. The IUCN Red List of Threatened Species 2018*: e.T22698230A132637221 [online]. 2018. [accessed 21.12.2020]. Available: https://dx.doi.org/10.2305/IUCN.UK.2018-2.RLTS.T22698230A132637221.en
24. UNESCO. *Megalithic Temples of Malta*. [accessed 15.11.2020]. Available: https://whc.unesco.org/en/list/132/
25. Malta Environment and Planning Authority. *Strategic Environmental Assessment: Environment Report*. Floriana, 2015.
26. PEUPLIER. *Hagar Qim*. [image]. [accessed 12.01.2021]. Available: http://www.flickr.com/photos/peuplier/3019403075/
27. Malta Environment and Planning Authority. *South Malta Local Plan*. Marsa, 2006, Vol. 2.
28. Raine H., Borg J., Raine A.F., Bairner S., Borg Cardona M. *Light Pollution and its Effect on Yelkouan Shearwaters in Malta; Causes and Solutions*. [online]. 2007. [accessed 03.01.2021]. Available: https://www.researchgate.net/publication/242353437_Light_Pollution_and_its_Effect_on_Yelkouan_Shearwaters_in_Malta_Causes_and_Solutions
29. Patriarca E., Debernardi P. *Bats and light pollution*. [online]. 2010. [accessed 03.01.2021]. Available: https://www.researchgate.net/publication/265079641_Bats_and_light_pollution
30. Micallef M., Chircop K., Zammit-Mangion D., Sammut A. Revised approach procedures to support optimal descents into Malta International Airport. In: *CEAS Aeronautical Journal*, 2014, 5(4), pp.461-475.
31. Murrieta-Mendoza A., Ruiz H., Botez R.M. Horizontal flight trajectory optimization considering RTA constraints. In: *MATEC Web of Conferences*, 2020, 314, 02002. https://doi.org/10.1051/matecconf/202031402002
32. University of Malta. Situation Awareness and Traffic Management for Engineless Taxiing (SAMET) project. [accessed 23.12.2020]. Available: (https://www.um.edu.mt/iat/ourresearch/fundedprojects/satmet
33. Malta International Airport. *Solar energy and water-saving systems help Malta International Airport reduce its ecological footprint*. [online] 2019. [accessed 28.11.2020]. Available: https://www.maltairport.com/solar-energy-and-water-saving-systems-help-malta-airport-reduce-its-ecological-footprint/
34. Malta International Airport. *Malta International Airport kicks off the terminal expansion project*. [online]. 29.01.2020. [accessed 28.11.2020]. Available: https://www.maltairport.com/malta-international-airport-kicks-off-terminal-expansion-project/
35. Delia J. €13.6m to be invested in airport security infrastructure: Home Affairs Minister announces EU-financed overhaul. In: *Times of Malta* (28 November). [online]. 2020. [accessed 10.12.2020]. Available: https://timesofmalta.com/articles/view/136m-to-be-invested-in-airport-security-infrastructure.834875

**https://doi.org/10.52326/jes.utm.2021.28(1).11**
**UDC 624.012:620**

# STRESS - STRAIN STATE OF THE LOCAL AREA IN THE BUILDING ELEMENT WITH STRUCTURAL DEFECT

Victor Kolokhov*, ORCID: 0000-0001-8223-1483,
Mykola Savytskyi, ORCID: 0000-0003-4515-2457,
Artem Sopilniak, ORCID: 0000-0002-3067-0529

*Pridneprovsk State Academy of Civil Engineering and Architecture, 24-a Chernyshevsky, 49600, Dnipro, Ukraine*
*Corresponding author: Victor Kolokhov, *kolokhov.viktor@pgasa.dp.ua*

Received: 01. 18. 2021
Accepted: 02. 26. 2021

**Abstract.** Evaluation of the building element technical state relies on verification calculations using estimated construction material properties. Physical and mechanical properties are estimated predominately by using non-destructive test methods. The accuracy of these methods is affected by the level of stress-strain state of the structural element and present structural defects. The variability of the concrete properties over time under constant loads is a determining factor for the durability and reliability of the structural element. The influence of the physical and mechanical characteristics of a construction material on the deformation process of the local area of the structural element adjacent to the structural defect has been investigated. The research has been performed on structural models using software systems "LIRA SAPR" and "SOLIDWORKS". A structural model having dimensions of 100 x 100 x 400 mm was used for the study. Materials of concrete grades C12/15 through C25/30 with corresponding properties have been used. Load parameters for modeling of the deformation process varied from 0.1 to 0.5 of the ultimate loads. Performed calculations made it possible to obtain fields of stress, deformation and displacement under different model parameters and stress levels.

**Keywords:** *stress-strain state, structural defect, non-destructive test methods, software systems "LIRA SAPR", "SOLIDWORKS".*

## Introduction

Ensuring reliability of buildings and structures [1] requires reliable information on their technical state. Technical state evaluation systems are based on determination of physical and mechanical characteristics (PMC) of structural materials. Formal evaluation requirements are governed by state standards [2 - 7], which implement non-destructive methods (NM) of control. The data obtained are subject to statistical processing following prescribed procedures, and the result of the processing is obtained with calculated accuracy. As demonstrated in [8 - 12], and in many other researches, evaluation results are significantly affected by the following: concrete composition; conditions of concrete element structure formation; age of concrete; level of stress-strain state (SSS) in the element and test conditions. The complexity of the direct determination of the PMC of concrete has directed researchers to a different path [13 - 18]. But yet, the variability in the

SSS level of the element leaves the procedure for applying the NM evaluation prone to considerable level of uncertainty. Structural defects and variation in concrete PMC during operation dramatically alter the element's SSS in the area near the defect. Determining the impact these factors have on the SSS of the structural element will improve the accuracy of the determination of the PMC of concrete in elements by means of NM control.

**Purpose of the study**

To obtain fields of stress, deformation and displacement under different model parameters and stress levels on structural models using software systems "LIRA SAPR" and "SOLIDWORKS".

**Materials and Methods of Research**

A model having dimensions of 100 x 100 x 400 mm was used for the study. Concrete grades C12/15 through C25/30 with corresponding properties [2] have been used as a model material. Research has been performed using software systems "LIRA SAPR" and "SOLIDWORKS". Similar structural models have been used for calculations with different software complexes.

Structural defects were modeled by removing successively one to four elements from the design model. That is, a groove with a depth of 0 to 25 mm was formed in the prism. The increment was 5 mm (0 to 0.25h, respectively, in 0.05 h increments). Calculations were made for models with one and two defects in the structure. In the case of a design model with two defects in the structure, the latter were arranged in parallel. During the study, the distance between these grooves varied. The load parameters for modeling the deformation process varied within 0.1 to 0.5 of the ultimate stress.

Figure 1 shows design model used for calculation using software system "LIRA SAPR".

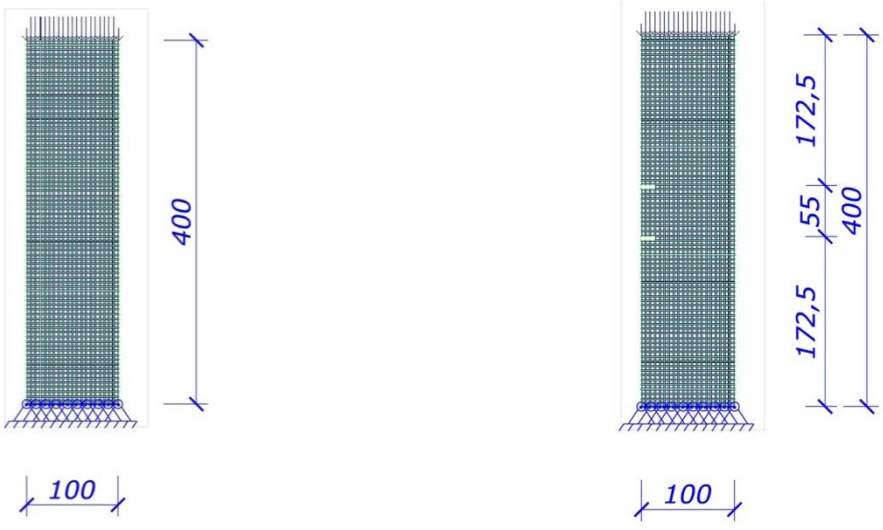


a) b)

**Figure 1.** design model used for calculation using software system "LIRA SAPR": a – without structural defects; b – with structural defects.

**Results and discussions**

Figure 2 - 7 show stress fields $N_x$, $N_y$ i $\tau_{xy}$ (correspondingly) in the area of the building element with structural defect. Separate results are presented for calculations subject to variable loads and variable defect sizes.

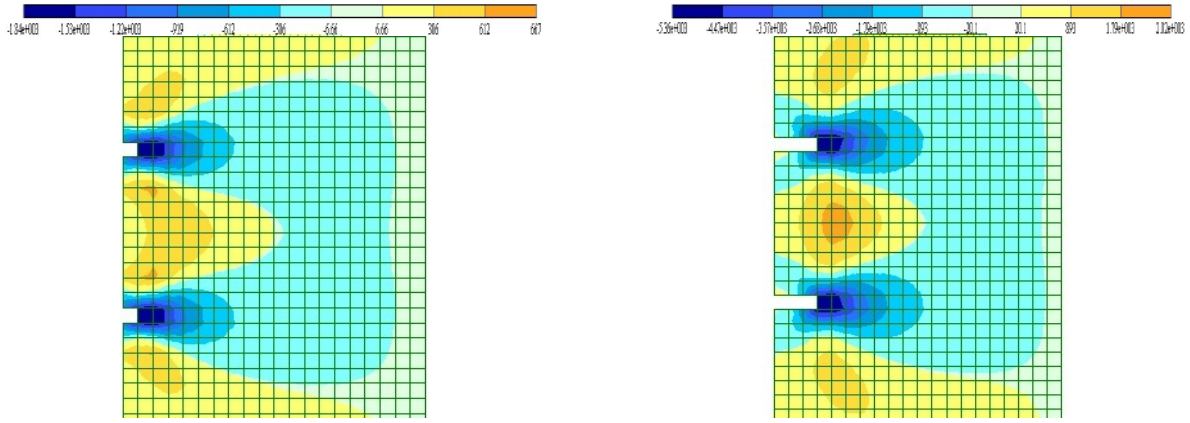

a) b)

**Figure 2.** Stress fields Nx in the area with structural defect: defect depth 5 mm (a) and 15 mm (b) for concrete grade C16/20 under stress in concrete $\sigma = 0{,}4\ f_{cd}$ [kH/m$^2$].

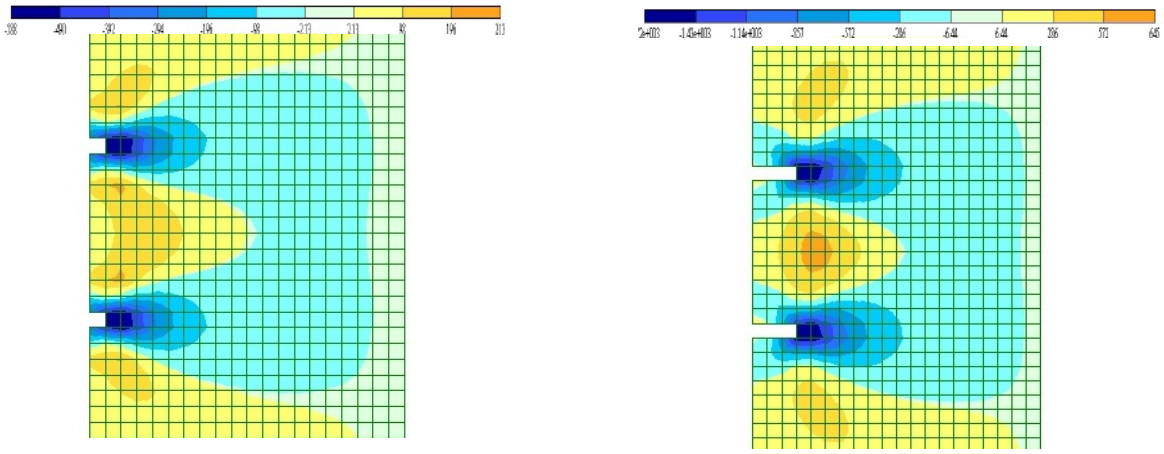

a) b)

**Figure 3.** Stress fields Nx in the area with structural defect: defect depth 5 mm (a) and 15 mm (b) for concrete grade C20/25 under stress in concrete $\sigma = 0{,}1\ f_{cd}$ [kH/m$^2$].

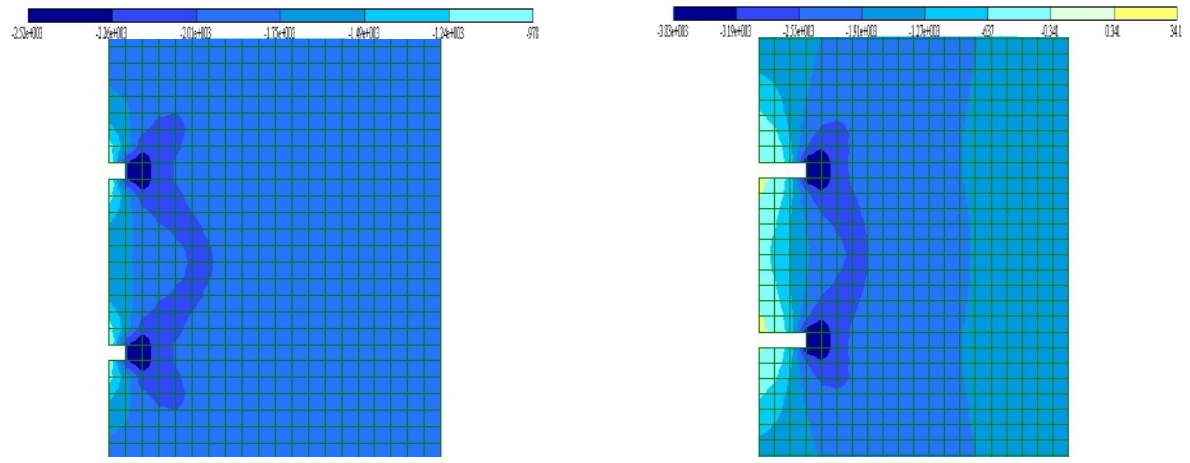

a) b)

**Figure 4.** Stress fields Ny in the area with structural defect: defect depth 5 mm (a) and 15 mm (b) for concrete grade C12/15 under stress in concrete $\sigma = 0{,}1\ f_{cd}$ [kH/m$^2$].

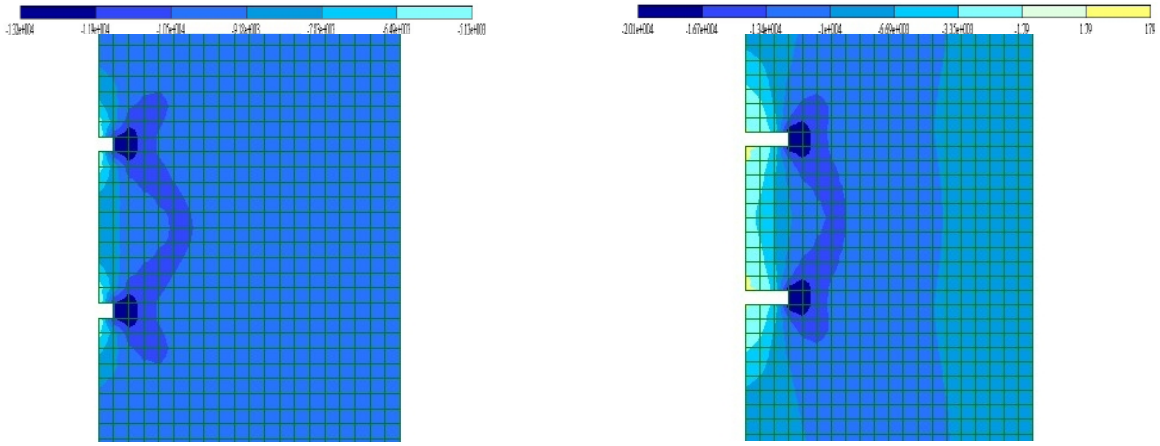

a) b)

**Figure 5.** Stress fields Ny in the area with structural defect: defect depth 5 mm (a) and 15 mm (b) for concrete grade C16/20 under stress in concrete $\sigma = 0{,}4\ f_{cd}$ [kH/m$^2$].

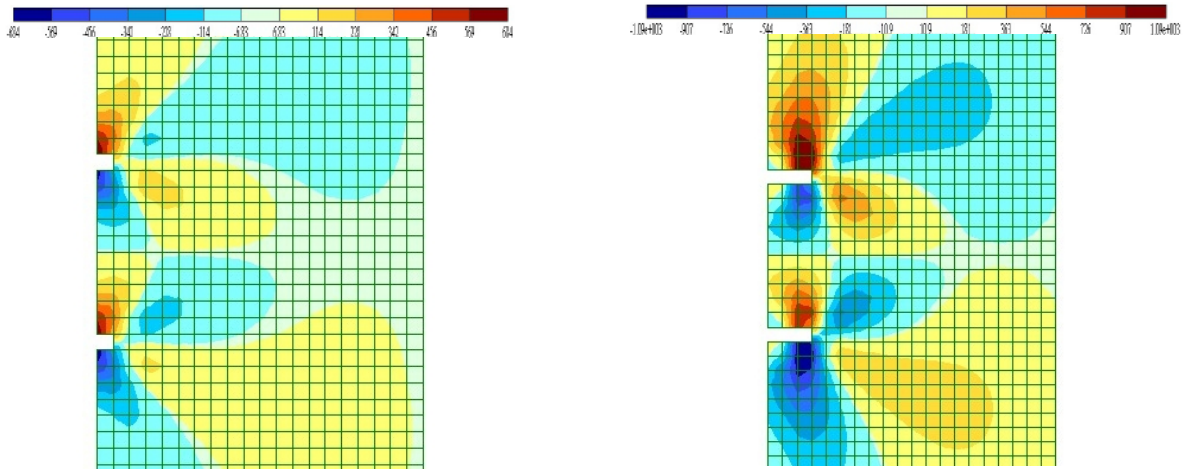

a) b)

**Figure 6.** Stress fields $\tau_{xy}$ in the area with structural defect: defect depth 5 mm (a) and 15 mm (b) for concrete grade C20/25 under stress in concrete $\sigma = 0{,}1\ f_{cd}$ [kH/m$^2$].

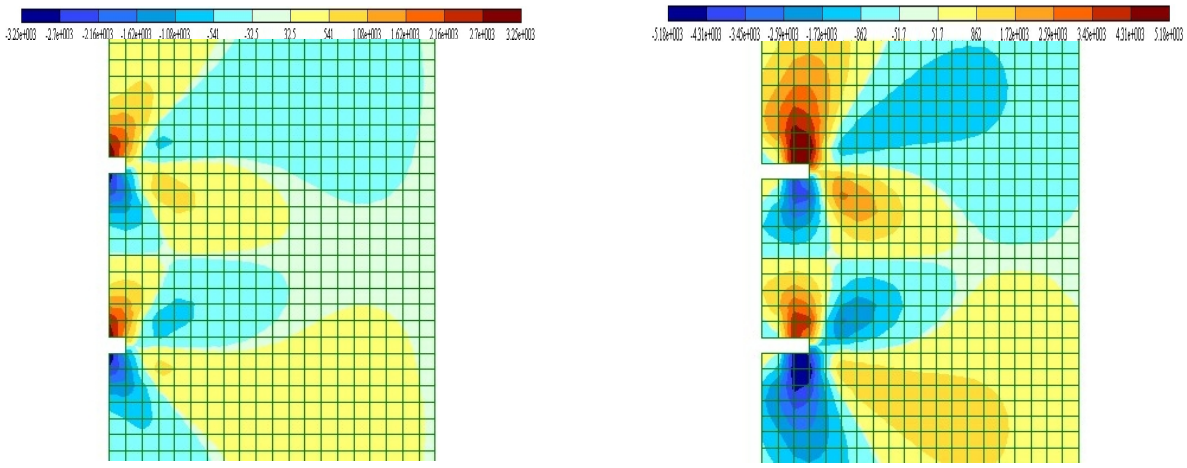

a) b)

**Figure 7.** Stress fields $\tau_{xy}$ in the area with structural defect: defect depth 5 mm (a) and 15 mm (b) for concrete grade C25/30 under stress in concrete $\sigma = 0{,}4\ f_{cd}$ [kH/m$^2$].

It is obvious that stress fields in all cases are similar. Various stress values are due to variability in loads, PMC of concrete and defect sizes.

Availability of design calculations affords their comparison with the results of NM control. Such comparison allows identification of structural defects formed during construction and/or operation periods [19]. Therefore the following procedure is proposed for evaluation of the building element technical state (Figure 8).

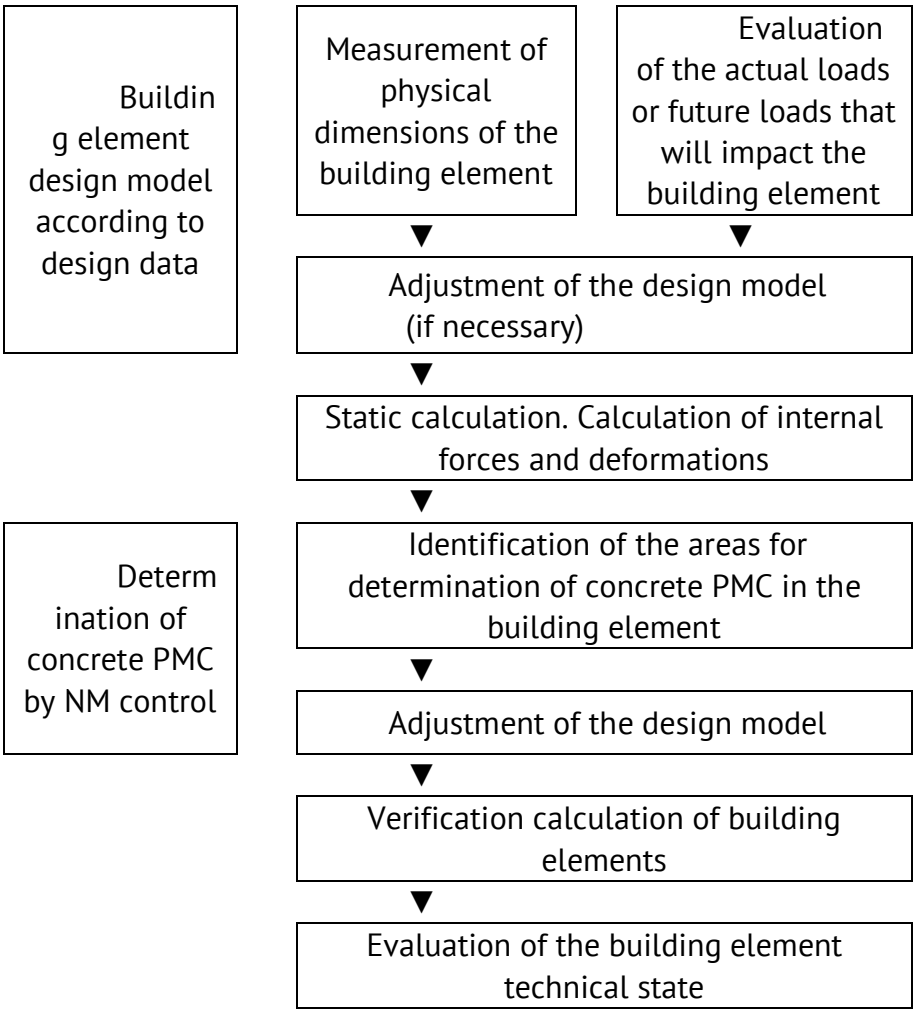


**Figure 8.** Procedure for evaluation of the building element technical state.

**Conclusions**

The results analysis of the conducted research shows that:

1. Different software complexes show essentially similar results.

2. The change in the stress in the area adjacent to structural defects is affected by the size of this area, SSS level in the structural element and the ratio between the sizes of the adjacent elements of the structure.

3. Zero stress areas may appear on the surface of the structural element.

4. It is necessary to take account of the level of SSS while performing evaluation of the PMC of concrete using NM control in the area influenced by present structural defects.

**References**


1. The system to ensure the reliability and safety of construction sites. Loads and Impacts. Design Standards: DBN V.1.2-2: 2006. Kiev: Minstroy of Ukraine, 2006. (State building regulations of Ukraine).
2. Structures of buildings and modules. Concrete and reinforced concrete constructions. Main provisions: DBN V.2.6-98: 2009. Kyiv: Minregionstroy of Ukraine, 2009. (State building codes of Ukraine.).
3. Building materials. Concrete Methods of determination. prism strength, modulus of elasticity and Poisson's coefficient: DSTU B V.2.7-217: 2009. Kyiv: Minregionstroy of Ukraine, 2010. (National Standard of Ukraine).
4. Building materials. Concrete Determination of durability by mechanical methods of non-destructive testing: DSTU B V.2.7-220: 2009. Kyiv: Minregionstroy of Ukraine, 2010. (National Standard of Ukraine).
5. Building materials. Concrete methods for determining the strength of samples taken from constructions: DSTU B V.2.7-223: 2009. Kyiv: Minregionstroy of Ukraine, 2010. (National Standard of Ukraine).
6. Building materials. Concrete rules of strength control: DSTU B V.2.7-224: 2009. Kyiv: Minregionstroy of Ukraine, 2010. (National Standard of Ukraine).
7. Building materials. Concrete Ultrasonic method for determining strength: DSTU B V.2.7-226: 2009. Kyiv: Minregionstroy of Ukraine, 2010. (National Standard of Ukraine).
8. Kolokhov V., Sopilniak, A., Gasii G., Kolokhov O. Structure materialphysic-mechanical characteristics accuracy determination while changing the level of stresses in the structure. International Journal of Engineering &Technology. 2018, vol. 7, no. 4.8, pp. 74–78.
9. Kolokhov V. V., Kozhanov Y. O., Zeziukov D. M., 2019 Influence of stress level in concrete constructions at ultrasound speed [Changing the time of ultrasonic oscillation propagation in concrete for changing conditions of measurement]. Bulletin of PSACEA 1(249-250), pp. 49–57. https://doi.org/10.30838/j.bpsacea.2312.260319.49.405.
10. Kolokhov, V. V., Kolokhov, O. V., 2019 Changing the time of ultrasonic oscillation propagation in concrete for changing conditions of measurement. Bulletin of PSACEA 2(251-252), pp. 92–101. https://doi.org/10.30838/j.bpsacea.2312.280519.95.441.
11. Kolokhov V. V., Kolokhov O. V., 2019 Some aspects of measuring the time of propagation of ultrasonic vibrations in concrete [Changing the time of ultrasonic oscillation propagation in concrete for changing conditions of measurement]. Bulletin of PSACEA 3(253-254), pp. 58–65. https://doi.org/10.30838/j.bpsacea.2312.040719.58.464.
12. Shishkin A., Netesa N., Scherba V., 2017 Effect of the iron-containing filler on the strength of concrete, Eastern-European Jornal of Enterprise Technologies, Vol. 5/6, (89), pp. 11–16. https://doi.org/10.15587/1729-4061.2017.109977.
13. Mori, K., Spagnoli, A., Murakami, Y., Kondo, G., Torigoe, I. A new non-contacting non-destructive testing method for defect detection in concrete", NDT and E International, Vol. 35, no. 6, (2002), pp. 399–406. https://doi.org/10.1016/S0963-8695(02)00009-9.
14. Schabowicz K. Ultrasonic tomography – The latest nondestructive technique for testing concrete members – Description, test methodology, application example. Archives of Civil and Mechanical Engineering, Vol. 14, no. 2, (2014), pp. 295–303. https://doi.org/10.1016/j.acme.2013.10.006.
15. Luong M. P., Nondestructive analysis of micro cracking in concrete, Proceedings of the International Conference on Nondestructive Testing of Concrete in the Infrastructure. Dearborn, (1993), pp. 199-217.
16. Weil G. J., Rowe T. J. 1998 Nondestructive testing and repair of the concrete roof shell at the Seattle Kingdome NDT and E International 31, no. 6, pp. 389–400. https://doi.org/10.1016/S0963-8695(98)00038-3.
17. Lacidogna G., Manuello A., Niccolini, G., Accornero, F., Carpinteri, A. Acoustic emission wireless monitoring of structures. Acoustic emission and related non-destructive evaluation techniques in the fracture mechanics of concrete: fundamentals and applications (Cambridge: Woodhead Publishing Ltd), 2015, pp. 15–40. https://doi.org/10.1016/B978-1-78242-327-0.00002-7.
18. Aggelis D. G., Mpalaskas A. C., Matikas T. E. Acoustic monitoring for the evaluation of concrete structures and materials Acoustic emission and related non-destructive evaluation techniques in the fracture mechanics of concrete: fundamentals and applications (Cambridge: Woodhead Publishing Ltd), 2015, pp. 269–286. https://doi.org/10.1016/B978-1-78242-327-0.00013-1.
19. Kolokhov V. V. Formalization of the procedure for determining the physicomechanical properties of concrete and its hardware. Construction, Materials Science, Engineering. Dnepropetrovsk, PSACEA Vol.69, 2013, pp.231–236.

*Journal of Engineering Science* *Vol. XXVIII, no. 1 (2021), pp. 117 - 123*
*Fascicle* *Architecture, Civil and Environmental Engineering* *ISSN 2587-3474*
*Topic* *Energy Efficiency and New Building Materials* *eISSN 2587-3482*

**https://doi.org/10.52326/jes.utm.2021.28(1).12**
**UDC 691.32:621.311.243**

# ENERGY-SAVING CHAMBER IN PRODUCTION OF BUILDING MATERIALS AND PRODUCTS

Michael Zavoloka[1], ORCID: 0000-0002-2080-1230,
Elena Shinkevich[2], ORCID: 0000-0002-2842-1785,
Varvara Vinnichenko[3], ORCID: 0000-0003-3700-5414,
Alexander Plit[4*], ORCID: 0000-0003-4745-6358

*[1,2,4]Odesa State Academy of Civil Engineering and Architecture, Odessa, Ukraine*
*[3]Kharkiv National University of Civil Engineering and Architecture, Kharkiv, Ukraine*
*Corresponding author: Alexander Plit, *alex89805@gmail.com*

Received: 12. 11. 2020
Accepted: 01. 15. 2020

**Abstract.** This paper presents the results of a study of the compressive strength of concrete in a cyclic solar chamber. The analysis of the existing types of industrial solar chambers is carried out and the main structural elements are considered. The method of calculating the solar chamber for the production of concrete products is presented. Experiments were carried out on heavy concrete compositions using MC-Bauchemie superplasticizers additives: MC-PowerFlow 3100 and MC-PowerFlow 2695. The samples were kept in a cyclical solar chamber. The strength of concrete was determined at different periods of concrete hardening. A comparative analysis of the results of the compressive strength of concrete in a solar and normal hardening chamber is carried out.

**Key words:** *green energy, cyclic solar chamber, heat treatment, superplasticizers, thermophysical processes.*

**Introduction**.

Analysis of literature data showed that the precast concrete industry is a large consumer of thermal energy. The most energy-intensive process in this area is the technological process of heat treatment of products, which consumes more than 70% of the energy. About 90% of the total volume of reinforced concrete products (concrete goods) is treated with steam. Non-renewable natural energy sources are used to generate steam. Taking into account the growing increase in their cost, heat and humidity treatment should be recognized as energy-inefficient. In this regard, the problem of rational use of traditional fuel and energy resources and the inclusion of unconventional energy sources, such as solar and wind energy, deep earth heat and secondary heat of various production processes, is becoming more acute. Currently, there is a tendency to increase the use of renewable energy sources, primarily solar. The use of solar energy finds its application in various areas of production processes, which is especially important for the southern regions of Ukraine [1, 2].

Solar thermal treatment - heating concrete reinforced concrete products by direct influence of solar radiation through translucent or sun receivers. The simplest way to use

solar energy for preheating concrete products is to use helioforms, which consist of two main elements: the mold itself and the lid with a translucent heat-insulating coating or in molds using a moisture-proof sun-perceiving coating in combination with thermos holding. Polymer photovoltaic cells are a promising coating for visible spectrum applications because the absorption spectra of organic semiconductors, including polymers and low molecular weight types, are not continuous as in inorganic semiconductors. As a result, the organic structure is capable of transmitting visible light and absorbing invisible light such as infrared. According to the energy distribution of the solar spectrum, more than half of the sunlight is distributed in the infrared region. Therefore, the theoretical efficiency of polymeric photovoltaic cells with only absorption of infrared radiation can be as high as that of a device with only absorption of visible light. [3 - 5].

The main part of the helioform is solar cells, which are semiconductor photovoltaic cells designed to directly convert solar radiation into electrical energy. They are part of a wider range of photocell devices. Usually solar cells have a large receiving surface area and the most important parameters for them are temperature stability, the coefficient of conversion of light energy into electrical energy, radiation resistance, etc. Most often, solar cells are a structure of semiconductor materials that absorb solar radiation well, metal and dielectric layers ... If the device contains liquid solutions of electrolytes, they are called photo electrochemical converters.

The operation of solid-state solar cells is based on the valve photoelectric effect. Light quanta absorbed by a semiconductor release electrons and holes from intracrystalline bonds and transfer them into a mobile state. After that, oppositely charged free charge carriers are spatially separated and move in opposite directions as a result of diffusion or drift in a force field, which should initially be present in a semiconductor [6].

The most important challenge for solar cells is to improve their efficiency. The efficiency of the photocell increases when concentrated sunlight is used, however, excess heat should be removed from the photocell. To date, scientists from the National Laboratory for the Study of Renewable Energy (USA) have achieved the highest efficiency rate and reached the level of 47% [7], in concentrated sunlight, thus setting a new blight record for solar panels. Among industrial designs, silicon-based cells show the best performance, although low-efficiency cells from cheaper conductors compete economically with mass production of high-efficiency and expensive solar cells. Industrial solar cells work using various solar cells, the main of which are silicon, monocrystalline, polycrystalline, amorphous film, polymer, photosensitized, which differ in efficiency and cost. When developing effective elements, efforts should be directed not only to their efficiency, but also to the compactness of systems. It is worth paying attention to plastic crystals, due to which it is possible to increase the compactness of systems and reduce the cost of their production [8 - 11].

Benefits of solar thermal treatment:

- saving non-renewable fuel and energy resources,
- the use of an environmentally friendly source of thermal energy,
- reducing the cost of concrete products,
- reduction of capital costs for the boiler house, heating main, etc.
- allows you to abandon the traditional heat treatment of precast concrete elements in warm seasons in areas south of 50 ° north latitude.

For heating concrete products, it is necessary to perform a calculation. The calculation method consists of three parts:

- calculation of the thermal balance of the chamber in which heat treatment is carried out. as a result of the calculation, the amount of energy required for heating is determined,

- determine the amount of heat that can be received by the solar collector. Such data for given geographic coordinates are provided by NASA. For the main cities of Ukraine, information is widely distributed on the Internet [12],

- find the area of solar collectors that will provide the required amount of energy. Heat balance equation [13]:

$$Q = Q_1 + Q_2 + Q_3 + Q_4 + Q_5 + Q_6 + Q_7 + Q_8 + Q_9 + Q_{10} + Q_{11} - Q_{12} \quad (1)$$

where $Q_1$ is the heat consumption for heating the components of the raw concrete mix, $Q_2$ is the heat consumption for heating the mixing water, $Q_3$ is the heat consumption for the evaporation of some of the water, $Q_4$ is the heat consumption for heating the reinforcement, $Q_5$ is the heat consumption for heating the molds, $Q_6$ is the heat, which is accumulated by the walls of the chamber, $Q_7$ is the heat consumption for heating the chamber lid, $Q_8$ is the heat consumption for heating the free space in the chamber, $Q_9$ is the heat loss due to heat leakage through the leaks, $Q_{10}$ is the heat loss to the environment by the chamber walls, $Q_{11}$ is the heat loss into the environment by the chamber lid, $Q_{12}$ - heat of exothermic reactions in concrete, Q - amount of energy required for heating, kJ / cycle.

The amount of heat that can be received by the solar collector [14, 15]:

$$Эк = E \cdot S \cdot \eta \quad (2)$$

where $E$ is the average daily level of solar radiation, kWh / m$^2$ / day, $S$ is the working area of the solar collector, m$^2$, $\eta$ is the efficiency of the solar collector.

The area of solar collectors that will provide the required amount of energy, m$^2$.

$$S = Q / E\eta \quad (3)$$

**The experimental procedure was as follows:** a laboratory model of a cyclic solar plant of the "Hot Box" type was installed. The design of the solar plant consisted of a wooden frame, on which a polyethylene film was stretched in two layers, with a gap between the layers of 2 cm. The size was assigned in such a way as to cover all three-piece molds with concrete mixture. The molds with the concrete mixture were placed in a solar plant and kept there until testing. Removal of samples for testing was carried out on 1, 3, 7, 14, 28 days. For the compositions under study, twin control samples were made in parallel, which were stored in a normal hardening chamber with a temperature of 20 ± 3 °C and a humidity of 95 ± 5%. For the manufacture of samples, Portland cement grade 500, quartz sand and polycarboxylate additives from MC-Bauchemie (Germany) were used: a complex additive with a superplasticizer with an accelerated hardening effect MC-PowerFlow 3100 and a superplasticizer MC-PowerFlow 2695. Samples of beams with a size of 40x40x160 mm were made in accordance with the current standard [18]. The tests were carried out on verified equipment. The results were processed in Excel according to calculations in accordance with the current standard, the data are given as the arithmetic mean of all the results of one batch of samples.

**Main material**

The results of tests of the compressive strength at 28 days for samples with the use of MC-PowerFlow 2695 additive showed an average strength of 26.5 MPa, which corresponds to the grade 250. Results of tests of the compressive strength at 28 days when using the complex additive MC-PowerFlow 3100 with acceleration effect of hardening, the corresponding grade of concrete was obtained on the 3rd day, and on the 28th day the average strength was 49.9 MPa, which corresponds to grade 450. For production, the rate of strength gain is one of the most important indicators, because the faster the product gains the stripping strength of 70-80% (for prefabricated reinforced concrete products) the more products the plant can produce. Samples using MC-PowerFlow 2695 additive gained stripping strength (on average 16.3 MPa) after 14 days of storage in a normal hardening chamber, samples using MC-PowerFlow 3100 additive achieved similar strength in 2-3 days, stripping strength (on average 35.4 MPa), the samples reached within 7 days of storage. When using the same formulations, samples with MC-PowerFlow 3100 additive showed accelerated build-up and a significant increase in strength compared to samples in which MC-PowerFlow 2695 additive was used, which, in turn, reduces cement consumption in the production of products. The results of the strength tests are given in table 1 and fig. 1.

*Table 1*

**Concrete test results when stored in a normal hardening chamber**

| Name | W/B | Days | Compressive strength, MPa | Name | W/B | Days | Compressive strength, MPa |
|---|---|---|---|---|---|---|---|
| MC-PowerFlow 3100 | 0,3 | 1 | 12,6 | MC-PowerFlow 2695 | 0,32 | 1 | 1,1 |
| | | 3 | 27,8 | | | 3 | 5,1 |
| | | 7 | 35,4 | | | 7 | 11,8 |
| | | 14 | 41,6 | | | 14 | 16,3 |
| | | 28 | 49,9 | | | 28 | 26,5 |

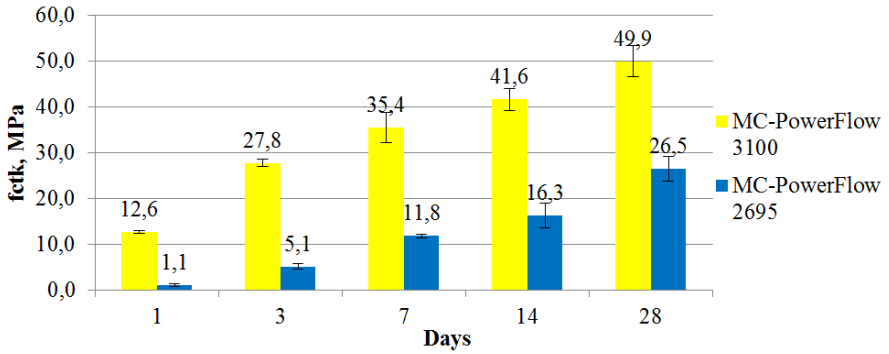


**Figure: 1.** Comparison of the compressive strength of concrete versus its age, using additives of plasticizers, when storing samples in a normal hardening chamber.

When storing samples in a solar chamber, due to heliothermal heating of samples, it was possible to achieve acceleration of concrete strength gain and to achieve tempering strength of 70 - 80% (on average 35.5 MPa) within 3 days for samples using MC-PowerFlow 3100 additive. time, the samples in the manufacture of which the additive MC-PowerFlow 2695 was used gained tempering strength (on average 19.8 MPa) after 7 days of storage.

Comparison of the strength between the samples from the solar and normal hardening chamber was also carried out. Specimens gaining strength in the solar chamber showed an accelerated strength gain under equal hardening conditions. The results are shown in table. 2 and fig. 2 - 4.

*Table 2*

**Concrete test results when stored in a solar chamber**

| Name | W/B | Days | Compressive strength, MPa | Compressive strength gain,% |
|---|---|---|---|---|
| MC-PowerFlow 3100 | 0,3 | 1 | 21,4 | 169,8 |
| | | 3 | 35,5 | 127,7 |
| | | 7 | 43,2 | 122,0 |
| | | 14 | 49,4 | 118,8 |
| | | 28 | 50,7 | 101,6 |
| MC-PowerFlow 2695 | 0,32 | 1 | 3,9 | 354,5 |
| | | 3 | 12,3 | 241,2 |
| | | 7 | 19,8 | 167,8 |
| | | 14 | 26,5 | 162,6 |
| | | 28 | 28,2 | 106,4 |

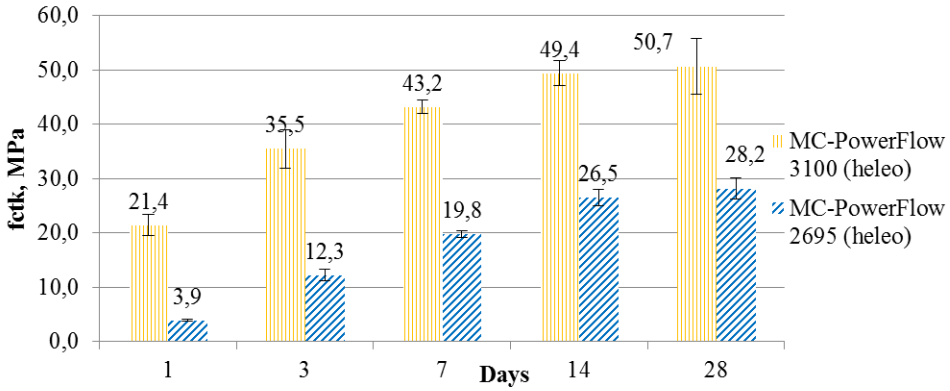


**Figure 2.** Comparison of the compressive strength of concrete versus its age, using additives of plasticizers, when storing samples in a solar chamber.

During the experiments, the strength characteristics of the concrete mixture were established. Heating in the solar chamber greatly accelerated the strength development of the samples with the use of MC-PowerFlow 2695 additive, so the samples kept in the solar chamber on the first day showed strength 254.5% higher than similar samples from the normal hardening chamber. On the 3rd day of storage, the maximum increase was 141.2%, on the 7th day - 67.8%, on the 14th day - 62.2% and on the 28th day - 6.4%. At the same time, samples with MC-PowerFlow 3100 additive showed less speed gain due to the initial accelerating properties of the concrete mix.

The experiments were carried out in the springtime of the year, which is not the hottest, and the solar chamber works entirely on solar energy and is completely dependent on the ambient temperature.

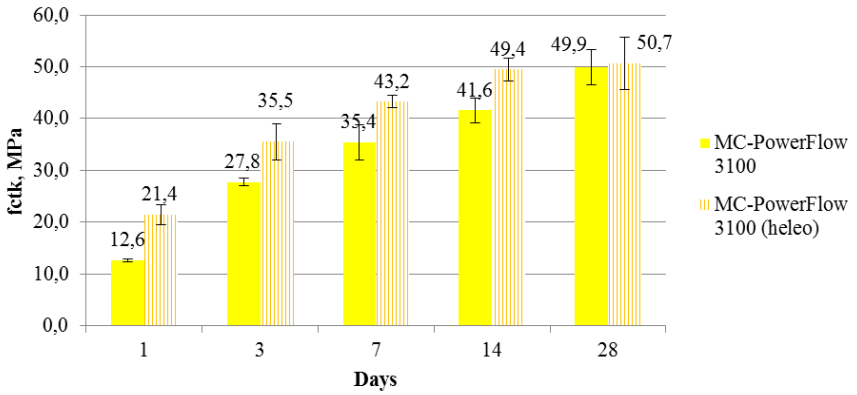


**Figure 3.** Comparison of concrete compressive strength versus its age depending on storage conditions using MC-PowerFlow 3100 additive.

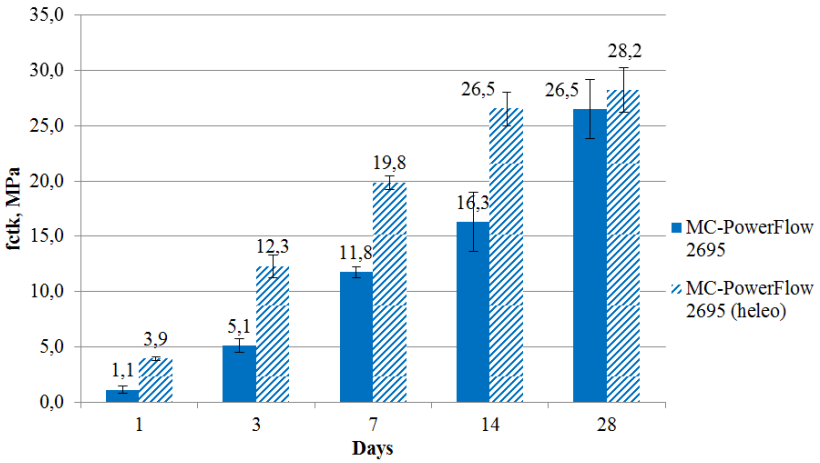


**Figure 4.** Comparison of concrete compressive strength versus its age depending on storage conditions, using MC-PowerFlow 2695 additive.

To determine the efficiency of the solar chamber, thermometers were installed to measure the temperature of the environment, concrete mixture and the temperature inside the solar chamber. In the course of the experiment, the maximum temperature values were revealed: the environment - 38 °C, the solar chamber - 46 °C and the concrete mix 52 °C.

**Main conclusions**

Experiments were carried out on two additives of superplasticizers manufactured by MC-Bauchemie showed that the use of a solar chamber significantly improves the initial set of strength, and helps to gain tempering strength in the shortest possible time, which in turn accelerates construction. Also, on the 3rd day of holding, the samples with the addition of MC-PowerFlow 2695 showed 43% strength, and the samples with the addition of MC-PowerFlow 3100 showed 70% strength. The use of a solar chamber does not increase the maximum strength of concrete, but only contributes to a faster gain in strength, and the combination with additives that accelerate the development of strength reduces the advisability of using a solar chamber. The paper presents a variant of calculating the solar chamber, which can be used to further improve existing and create new efficient solar chambers and is one of the directions for the development of precast concrete production in areas with hot climates.

**Reference**


1. Malyarenco V.A. *Energetika dovkillya. Energosberegennya* - Kharkiv: Rybikon, 2004.
2. Alaa A.F. Husain, Wan Zuha W. Hasan, Suhaidi Shafie, Mohd N. Hamidon, Shyam Sudhir Pandey. A review of transparent solar photovoltaic technologies. In *Renewable and Sustainable Energy Reviews,* October 2018, Volume 94, pp. 779-791; DOI:https://doi.org/10.1016/j.rser.2018.06.031
3. Thibaut Esence, Hadrien Benoit, Damien Poncin, Michael Tessonneaud, Gilles Flamant. A shallow cross-flow fluidized-bed solar reactor for continuous calcination processes. In *Solar Energy,* January 2020, Volume 196, pp. 389-398; DOI:https://doi.org/10.1016/j.solener.2019.12.029
4. Jane M-F Johnson, Don Reicosky, Ray Allmaras, Dave Archer and Wally Wilhelm. A matter of balance: Conservation and renewable energy. In *Journal of Soil and Water Conservation,* July 2006, 61 (4) 120A-125A; https://www.jswconline.org/content/61/4/120A
5. Sheng-Yung Chang, Pei Cheng, Gang Li, Yang Yang. Transparent Polymer Photovoltaics for Solar Energy Harvesting and Beyond. In Joule, 2018, V2, issue 6, pp. 1039-1054 DOI:https://doi.org/10.1016/j.joule.2018.04.005
6. Serdyk V.V. *Fizika colnechnuh elementov*. Odessa: Izdatelstvo "Logos". 1994.
7. John F. Geisz, Ryan M. France, Kevin L. Schulte, Myles A. Steiner, Andrew G. Norman, Harvey L. Guthrey, Matthew R. Young, Tao Song, Thomas Moriarty. Six-junction III–V solar cells with 47.1% conversion efficiency under 143 Suns concentration. In *Nature Energy volume,* 2020, 5, pp. 326 – 335.
8. Angel Serrano, Mikel Durana, Jean-LucDauvergne, Stefania Doppiu, Elena Palomo Del Barrioa. Tailored transition temperature plastic crystals with enhanced thermal energy storage capacity. In *Solar Energy Materials and Solar Cells,* January 2021, Volume 220; DOI:https://doi.org/10.1016/j.solmat.2020.110848
9. Yifeng Zhao, Paul Procel, Can Hana, Luana Mazzarella, Guang tao Yang, Arthur Weeber, Miro Zeman, Olindo Isabella. Design and optimization of hole collectors based on nc-SiOx:H for high-efficiency silicon heterojunction solar cells. In *Solar Energy Materials and Solar Cells*, January 2021, Volume 219; DOI:https://doi.org/10.1016/j.solmat.2020.110779
10. María José Montesa, José Ignacio Linares, Rubén Barbero, Antonio Rovira. Proposal of a new design of source heat exchanger for the technical feasibility of solar thermal plants coupled to supercritical power cycles. In *Solar Energy,* November 2020, Volume 211, pp.1027-1041; DOI:https://doi.org/10.1016/j.solener.2020.10.042
11. Amelia Gulkis. The Energy Pyramid: The best path to lasting energy savings. In *Journal of Soil and Water Conservation,* September 2009, 64 (5) 143A-144A; DOI:https://doi.org/10.2489/jswc.64.5.143A
12. *Karta solnechnoi activnosti v Ukraine*. [online]. [accesat 05.11.2020]. Disponibil: https://www.solar-battery.com.ua/karta-solnechnoy-aktivnosti-v-ukraine/
13. Kucherenko A.A. *Teplovye ustsnovki zavodov sbornogo jelezobetona*. Kuiv: Vyja shkola. Golovnoe izdatelstvo, 1977.
14. Duffie J.A., Beckman W.A. *Solar engineering of thermal process.* – New York: John Wiley and Sons, 1980.
15. K.K. Gopinathan, N.B. Maliehe, M.I. Mpholo. A study on the intercepted insolation as a function of slope and azimuth of the surface. In *Energy*, 2007, 7, pp. 213 – 220.
16. DSTY B V.2.7-214 «Budivelni materialy. Betony. Metody vuznachennya micnosti za kontrolnymy zrazkamy»; DOI:http://online.budstandart.com/ua/catalog/doc-page.html?id_doc=25943

*Journal of Engineering Science* *Vol. XXVIII, no. 1 (2021), pp. 124 - 130*
*Fascicle* *Architecture, Civil and Environmental Engineering* *ISSN 2587-3474*
*Topic* *Environmental Engineering* *eISSN 2587-3482*

**https://doi.org/10.52326/jes.utm.2021.28(1).13**
**UDC 628.335:637.513**

# EFFICIENCY OF COAGULATION-FLOCCULATION PROCESS IN THE TREATMENT OF ABATTOIR EFFLUENT

Ayokunle Familusi[1]*, ORCID ID: 0000-0003-4540-3674,
Adebola Adekunle[1], ORCID ID: 0000-0002-0129-2987,
Adedayo Badejo[1], ORCID ID: 0000-0001-7734-7086,
Olayemi Adeosun[2], ORCID ID: 0000-0003-3158-6799

[1]*Department of Civil Engineering, Federal University of Agriculture, Abeokuta, Nigeria*
[2]*Department of Agricultural and Bio-Systems Engineering, Federal University of Agriculture, Abeokuta, Nigeria*
*Corresponding author: Ayokunle Familusi, *ayomacfamilson@gmail.com*

Received: 01. 12. 2021
Accepted: 02. 19. 2021

**Abstract.** The use of coagulation-flocculation process as means of wastewater treatment is gradually becoming more popular. This research work is to evaluate the efficiency of coagulation-flocculation process in the treatment of abattoir effluent. Samples of abattoir effluent were collected from a slaughterhouse at Ede, Nigeria, and Alum was used in the coagulation-flocculation treatment of the effluent. The physico-chemical and bacteriological analyses of the untreated and treated effluent were carried out and these were used in determining the efficiency of the treatment process. The values obtained (from the physico-chemical and bacteriological analyses) were also compared with the effluent standard of Environmental Protection Agency (EPA). Coagulation-flocculation process is performed efficiently in reducing the contaminant level of Colour, TDS, Turbidity, Conductivity, TSS, Total Hardness, COD, Coliform, metals and other pollutants from the effluent.

**Keywords:** *Abattoir Effluent, Coagulation, Contaminants, Wastewater, Treatment.*

## 1. Introduction

Coagulation is the process by which particles become destabilized and begin to clump together; it is an essential component in water treatment operations [1]. Wastewaters often contain pollutants that are present in colloidal form. In such cases the colloidal suspension may contain organic materials, metal oxides, insoluble toxic compounds, stable emulsions and material producing turbidity. The primary purpose of the coagulation/flocculation process is the removal of turbidity from the water. The chemical and electrical means of water and waste water treatment can be achieved by using coagulation as the most important physico-chemical operation [2].

Management of wastewater from the red meat processing industry is an important issue. Due to the specific characteristics of wastewater, such as irregular discharge and considerable organic and biogenic loading, it can be difficult and costly to treat. The

organic loading rate of wastewater from the red meat processing industry can be several times higher than the average domestic sewage. Also, it is well known that its high content of fat, oil and grease (FOG) is another issue that makes the treatment process much more difficult. A combination of a main and an aid coagulant has shown to be efficient and cost-effective in treating abattoir wastewater. Coagulant aids are capable of reducing the amount of chemicals required and the sludge produced [3].

It is important to note that preliminary settling time, alum dose, rapid and slow mixing times, addition of polyelectrolyte as coagulant aid and particle size distribution were found to be important operational parameters for effective treatment of abattoir wastewater. Alum generally provides good clarification, rapid settling sludge and permits the use of a simple method of recovery that ensures destruction of most sewage solids in the resulting sludge [4]. In the work of [5], after using three common coagulants (Aluminium Sulphate ($Al_2(SO_4)_3.18H_2O$), Poly-Aluminum Chloride (PAC), and Ferrous Sulphate ($FeSO4.7H_2O$)) with the wastewater from a slaughterhouse, it was concluded that coagulation is one of the effective methods to remove organic matter from slaughterhouse wastewater, the results of their work prove that the coagulation method is a fast and an effective method in a partial treatment of slaughterhouse pollution and could be an important step before biological methods. Coagulant like Sodium aluminate ($NaAlO_2$) has been used in wastewater treatment in the phosphorous removal process. While the other aluminium and iron salts act as acids consuming alkalinity, sodium aluminate acts as a base [6]. The electro-coagulation (EC) technology [7, 8] can also be used to treat abattoir wastewater for safe discharge. Under the operating conditions studied, the performance of the process was improved by lowering the initial solution pH and increasing the electrolysis time, current intensity, settling time and operating temperature. The removal efficiency of over 90% was achieved under optimum condition. The findings of their separate study show that electro-coagulation technique using Fe-Fe electrodes and/or Fe-Al electrodes is effective in abattoir wastewater treatment. The aim of this research work is to evaluate the efficiency of coagulation-flocculation process in the treatment of abattoir effluent.

## 2. Materials and methods

### 2.1 Materials and Equipment Required for the Study

The materials and equipment used in carrying out this research work include:

- Aluminium Sulphate (Alum)
- Flocculating Machine
- Jar Test Apparatus
- GPS
- Standard laboratory for physico-chemical and bacteriological analyses.

### 2.2 Methods

**Preparation of alum (coagulant)**

Aluminium Sulphate (alum) purchased from an outlet in Osogbo, Nigeria was used in preparing an alum solution in which 200g of alum was dissolved per 1000ml of distilled water.

**Collection of effluent samples**

Samples of abattoir effluent were taken from an abattoir at Ede, Nigeria (at coordinates $7^0$ 42’ 25” N and $4^0$ 23’ 38” E).

**Jar test on the effluent sample**

10ml of abattoir effluent was put in a cuvette and inserted into a Lovibond comparator, to determine the colour that matches with the wastewater sample. After the determination of initial colour, pH and temperature, 500ml of the wastewater sample was measured in three places (beakers) and the equivalent volume of Alum solution was measured with respect to the colour into each abattoir sample. The beakers were placed into the flocculating machine and the roller was allowed to mix the sample rigorously for five minutes and then the speed was reduced for another 15mins. The samples were left to settle and the abattoir samples were decanted to check for the final colour, pH and temperature.

**Coagulation-Flocculation Process**

A known volume of abattoir effluent was fed into the coagulation/flocculation bucket and the alum dose (determined from jar test) was added to 0.001$m^3$ of the abattoir effluent in the flocculation bucket. The flocculation bucket was placed into the flocculating machine and the roller was allowed to mix the samples rigorously for five minutes; followed by 15 minutes of slow mixing. The sample was left to settle for one hour and later decanted.

**Physico-Chemical and Bacteriological Analyses should be indented**

Three samples each of the untreated and treated (coagulated) abattoir effluent were taken to the laboratory of Osun State Water Corporation, Ede, Nigeria for physico-chemical and bacteriological analyses. The parameters were determined in line with the standard methods of water and wastewater examination as prescribed by American Public Health Association [9].

## 3. Results and discussion

### 3.1 Jar Test

It was revealed from the jar test results that the mean coagulant dosage (Alum) required to treat 500ml of abattoir effluent is 150ml.

### 3.2 Physico-Chemical and Bacteriological Analyses of the Wastewater

The physico-chemical and bacteriological parameters of the untreated and treated wastewater samples are as shown in Table 1.

**pH**

The value for the pH of the abattoir effluent was 5.150±0.044, after coagulation, the value increased to 5.840±0.157. The coagulation brings about slight increase in the pH but the values obtained fall slightly off the limit (6 - 9) promulgated by the effluent standard of [10]. There was an improvement in the value after the treatment because the coagulant is an alkaline substance.

**Turbidity**

The value for the Turbidity of the abattoir effluent was 200.000±1.528 FTU, after coagulation, the value decreased to 180.000±2.291 FTU. The reduction in turbidity level could be traceable to the Silica content of the coagulant.

*Table 1*

**Physico-Chemical and Bacteriological Analyses of the Treated and Untreated Abattoir Effluent**

| | N | Abattoir Effluent | Alum-Coagulated | Efficiency (%) |
|---|---|---|---|---|
| Colour (HU) | 3 | 1500.000±1.732* | 450.000±7.000 | 70.000 |
| Appearance | 3 | | Not Clear | |
| Taste & Odour | 3 | | Objectionable | |
| Turbidity (FTU) | 3 | 200.000 ±1.528 | 180.000±2.291 | 10.000 |
| pH | 3 | 5.150 ±0.044 | 5.840 ±0.157 | -13.398 |
| Conductivity (µS/cm) | 3 | 1005.000±4.583 | 750.000±7.550 | 25.373 |
| Temperature ($^0$C) | 3 | 26.000±0.200 | 25.400±0.500 | 2.308 |
| TSS (mg/l) | 3 | 1.036 ± 0.004 | 1.000±0.020 | 3.475 |
| TDS (mg/l) | 3 | 850.000 ± 4.093 | 346.00±3.606 | 59.294 |
| Dissolved Oxygen (mg/l) | 3 | 0.130 ± 0.013 | 0.820±0.044 | -530.769 |
| Total Alkalinity (mg/l) | 3 | 546.000 ± 3.606 | 428.000 ± 1.323 | 21.612 |
| Total Hardness (mg/l) | 3 | 546.000 ± 2.646 | 428.000±2.180 | 21.612 |
| Calcium Hardness (mg/l) | 3 | 160.000 ± 2.646 | 314.000±2.646 | -96.25 |
| Calcium ions (mg/l) | 3 | 64.000 ± 1.732 | 125.600±0.721 | -96.25 |
| Magnesium Hardness (mg/l) | 3 | 386.000 ± 5.568 | 114.000±2.180 | 70.466 |
| Magnesium ions (mg/l) | 3 | 96.500 ± 1.803 | 28.500±2.291 | 70.466 |
| Chloride ions (mg/l) | 3 | 131.000 ± 1.732 | 85.000±3.123 | 35.115 |
| Iron (mg/l) | 3 | 84.110 ± 0.840 | 4.213±0.015 | 94.991 |
| Silica (mg/l) | 3 | 61.192 ± 0.731 | 21.132±1.253 | 65.466 |
| Nitrate Nitrogen (mg/l) | 3 | 20.146 ± 1.076 | 2.500±0.046 | 87.591 |
| Nitrite Nitrogen (mg/l) | 3 | 7.132 ± 0.020 | 0.725±0.007 | 89.835 |
| Copper (mg/l) | 3 | 18.143 ± 0.061 | 1.046±0.004 | 94.235 |
| Manganese (mg/l) | 3 | 1.389 ± 0.025 | 0.841 ± 0.002 | 39.453 |
| Aluminium (mg/l) | 3 | 2.413 ± 0.011 | 0.928 ± 0.003 | 61.542 |
| Fluoride (mg/l) | 3 | 1.009 ± 0.019 | 0.516 ± 0.004 | 48.860 |
| Sulphide (mg/l) | 3 | 2.316 ± 0.010 | 1.044 ± 0.005 | 54.922 |
| Chromium (mg/l) | 3 | 0.917 ± 0.006 | 0.418±0.003 | 54.417 |
| Sulphate (mg/l) | 3 | 10.000 ± 0.132 | 7.000 ± 0.173 | 30.000 |
| Zinc (mg/l) | 3 | 0.841 ± 0.005 | 0.400 ± 0.017 | 52.438 |
| Carbonate (mg/l) | 3 | 546.000 ± 3.606 | 428.000 ± 1.323 | 21.612 |
| Bicarbonate (mg/l) | 3 | 1907.200 ± 0.755 | 1640.000 ± 1.323 | 14.010 |
| Chlorine (mg/l) | 3 | | NIL | |
| COD (mg/l) | 3 | 460.000 ± 2.291 | 380.000 ± 5.568 | 17.391 |
| BOD (mg/l) | 3 | 0.050 ± 0.002 | 0.150±0.017 | -2.000 |
| Coliform (MPN/100ml) | 3 | 204.000 ± 1.000 | 179.833 ± 0.764 | 12.092 |

*Each value represents the mean value ±standard deviation of three samples

**Temperature**

The value for the temperature of the abattoir effluent was 26.000±0.200$^0$C, after coagulation, the value decreased to 25.400±0.500$^0$C. The values obtained satisfy the limit 35$^0$C promulgated by the effluent standard of [10].

**Colour**

The value for the colour of the abattoir effluent was 1500.000±1.732 HU, after coagulation, the value decreased to 450.000±7.000 HU. The value obtained after the treatment satisfies the limit (550 HU) promulgated by the effluent standard of [10].

**Conductivity**

The value for the Conductivity of the abattoir effluent was 1005.000±4.583 µS/cm, after coagulation, the value decreased to 750.000±7.550 µS/cm respectively. The reduction in the Conductivity level could be traceable to reduction in TDS witnessed during coagulation since Conductivity is a function of TDS in a water/wastewater sample.

**Total Suspended Solids (TSS)**

The value for the TSS of the abattoir effluent was 1.036±0.004 mg/l, after coagulation, the value decreased to 1.000±0.020 mg/l. The values obtained satisfy the limit (30 mg/l) promulgated by the effluent standard of [10].

**Total Dissolved Solids (TDS)**

The value for the TDS of the abattoir effluent was 850.000±4.093 mg/l, after coagulation, the value decreased to 346.000±3.606 mg/l.

**Alkalinity**

The value for the Total Alkalinity of the abattoir effluent was 546.000±3.606 mg/l, after coagulation, the value decreased to 428.000±1.323 mg/l. The higher Alkalinity level of the wastewater after the treatment could be traceable to the carbonates formed in the process.

**Hardness**

The value for the Total Hardness of the abattoir effluent was 546.000±2.646 mg/l, after coagulation, the value decreased to 428.000±2.818 mg/l. The increase in hardness could be traceable to the richer content of Magnesium oxide in the coagulant.

**Silica**

The value for the Silica of the abattoir effluent was 61.192±0.731 mg/l, after coagulation, the value decreased to 21.132±1.253 mg/l.

**Fluoride**

The value for the Fluoride of the abattoir effluent was 1.009±0.019 mg/l, after coagulation, the value decreased to 0.516±0.004 mg/l. The values obtained satisfy the limit (15 mg/l) promulgated by the effluent standards of [10].

**Sulphide**

The value for the Sulphide of the abattoir effluent was 2.316±0.010 mg/l, after coagulation, the value decreased to 1.044±0.005 mg/l. The values obtained satisfy the limit (1.0 mg/l) promulgated by the effluent standards of [10].

**Sulphate**

The value for the Sulphate of the abattoir effluent was 10.000±0.132 mg/l, after coagulation, the value decreased to 7.000±0.173 mg/l.

**Chloride**

The value for the Chloride of the abattoir effluent was 131.000±1.732 mg/l, after coagulation, the value decreased to 85.000±3.123 mg/l.

**Manganese**

The value for the Manganese of the abattoir effluent was 1.389±0.025 mg/l, after coagulation, the value decreased to 0.841±0.002 mg/l. The values obtained satisfy the limit (10 mg/l) promulgated by the effluent standards of [10].

**Zinc**

The value for the Zinc of the abattoir effluent was 0.849±0.005 mg/l, after coagulation, the value decreased to 0.400±0.017 mg/l. The values obtained satisfy the limit 5 mg/l promulgated by the effluent standard of [10].

**Aluminium**

The value for the Aluminium of the abattoir effluent was 2.413±0.011 mg/l, after coagulation, the value decreased to 0.928±0.003 mg/l.

**Chromium**

The value for the Chromium of the abattoir effluent was 0.917±0.006 mg/l, after coagulation, the value decreased to 0.418±0.003 mg/l. The values obtained satisfy the limit 2 mg/l promulgated by the effluent standard of [10].

**Copper**

The value for the Copper of the abattoir effluent was 18.143±0.061 mg/l, after coagulation, the value decreased to 1.046±0.001 mg/l. The value obtained after the treatment satisfies the limit 3 mg/l promulgated by the effluent standard of [10].

**Iron**

The value for the Iron of the abattoir effluent was 84.110±0.840 mg/l, after coagulation, the value decreased to 4.213±0.015 mg/l. The value obtained after the treatment satisfies the limit 5 mg/l promulgated by the effluent standards of [10].

**Nitrate**

The value for the Nitrate of the abattoir effluent was 20.146±1.076 mg/l, after coagulation, the value decreased to 2.500±0.046 mg/l. The values obtained satisfy the limit 50 mg/l promulgated by the effluent standards of [10].

**Dissolved Oxygen (DO)**

The value for the DO of the abattoir effluent was 0.130±0.013 mg/l, after coagulation, the value increased to 0.820±0.044 mg/l.

**Bio-Chemical Oxygen Demand (BOD)**

The value for the BOD of the abattoir effluent was 0.050±0.002 mg/l, after coagulation, the value increased to 0.150±0.017 mg/l. The values obtained satisfy the limit 30 mg/l promulgated by the effluent standard of [10].

**Chemical Oxygen Demand (COD)**

The value for the COD of the abattoir effluent was 460.000±2.291 mg/l, after coagulation, the value decreased to 380.000±5.568 mg/l. The coagulation helps in removing the COD from the wastewater, but the COD value obtained could not satisfy the limit 100 mg/l promulgated by the effluent standard of [10].

**Coliform**

The value for the Coliform of the abattoir effluent was 204.000±1.000 MPN/100ml, after coagulation, the value decreased to 179.833±0.764 MPN/100ml. The presence of Coliform suggests the possible presence of pathogenic micro-organisms in the wastewater sample.

### 3.3 Efficiency of the treatment method

The efficiency (Ƞ) of the coagulation-flocculation process (as shown in Table 1) was determined from eq. 1:

$$Ƞ = \frac{(C1-C2)\ X\ 100}{C1} \quad (1)$$

where Ƞ is the efficiency of the treatment unit,

$C_1$ is the parameter value before treatment, and

$C_2$ is the parameter value after treatment.

## 4. Conclusion

The treatment of abattoir effluent through coagulation-flocculation process has proved to be efficient in reducing the contaminant level of Colour, TDS, Iron, Copper, Aluminium, Chromium, Zinc, Silica, Fluoride, Nitrates, Nitrites, Sulphide and Magnesium Hardness in the effluent as the efficiency values range from 40% to 100%, but the process has a very weak efficiency in removing Turbidity, Conductivity, TSS, Total Alkalinity, Total Hardness, Chloride, Manganese, Sulphate, COD and Coliform from the effluent as the efficiency values range from 0% to 39%.

However, the removal efficiency is of negative value in terms of the DO, BOD and Calcium Hardness of the effluent. In respect of those pollutants for which the coagulation-flocculation process has a very weak or negative efficiency, the efficiency can be improved by combining the coagulation-flocculation process with the filtration process.

**References**


1. *Coagulation*. [online]. 2019. [accesat 13.07.2019]. Disponibil: https://www.oregon.gov/oha/PH/HEALTHYENVIRONMENTS/DRINKINGWATER/OPERATIONS/TREATMENT/Documents/Coagulation.pdf
2. Prakash N. B., Sockan V., Jayakaran P. Waste Water Treatment by Coagulation and Flocculation. In: *International Journal of Engineering Science and Innovative Technology (IJESIT),* 2014, *3* (2), pp. 479-484.
3. Hamawand, I. *Review of wastewater treatment chemicals and organic chemistry alternative for abattoir effluent* [online]. 2015 [accesat 04.11.2020]. Disponibil: https://www.ampc.com.au/uploads/cgblog/id27/Review-of-wastewater-treatment-chemicals-and-organic-chemistry-alternatives-for-abattoir-effluent.pdf
4. Amuda O. S., Alade A. Coagulation/flocculation process in the treatment of abattoir wastewater. In: *Desalination,* 2006, *196*, pp. 22–31.
5. Ha B. M., Huong D. T. G. Coagulation in Treatment of Swine Slaughterhouse Wastewater. In: *GeoScience Engineering,* 2017, *63* (1), pp. 15-21.
6. Engelhardt T. L. *Coagulation, Flocculation and Clarification of Drinking Water*. [online]. 2010 [accesat 05.10.2020]. Disponibil: https://sswm.info/sites/default/files/reference_attachments/ENGELHARDT%202010.%20Coagulation%2C%20flocculation%20and%20clarification.pdf
7. Nwabanne J. T., Obi C. C. Abattoir wastewater treatment by electrocoagulation using iron electrodes. in: *Der chemica sinica, 2017, 8* (2), PP. 254-260.
8. Budiyono, Widiasa, I. N., Johari, S. Study on Treatment of Slaughterhouse Wastewater by Electro-coagulation Technique. In: *International Journal of Science and Engineering, 2010, 1*(1), *pp. 25-28.*
9. APHA. *Standard methods for examination of water and wastewater, 20th ed*. Washington DC, USA: A Publication of American Public Health Association, 1998.
10. *Effluent Standards*. [online]. 2014 [accesat 07.09.2019]. Disponibil: https://www.extwplegs1.fao.org/docs/pdf/tw164144.pdf

*Journal of Engineering Science* *Vol. XXVIII, no. 1 (2021), pp. 131 - 143*
*Fascicle* *Food Engineering* *ISSN 2587-3474*
*Topic* *Food Technologies and Food Processes* *eISSN 2587-3482*

**https://doi.org/10.52326/jes.utm.2021.28(1).14**
**UDC 664.6:633.494**

# JERUSALEM ARTICHOKE (*HELIANTHUS TUBEROSUS*) FLOUR IMPACT ON BREAD QUALITY

Aurica Chirsanova[1], ORCID: 0000 -0002-1172-9900,
Tatiana Capcanari[1], ORCID: 0000-0002-0056-5939,
Ecaterina Gîncu[2], ORCID ID: 0000-0001-6267-2310

[1]*Technical University of Moldova, 168, Stefan cel Mare Bd., Chisinau, Republic of Moldova*
[2] *Academy of Economic Studies of Moldova, 61 Bănulescu-Bodoni Street, Chișinau, Republic of Moldova*
*Corresponding author: Aurica Chirsanova, *aurica.chirsanova@toap.utm.md*

Received: 01. 23. 2021
Accepted: 02. 25. 2021

**Abstract.** Jerusalem artichoke tubers are known for their high content of nutrients, high acidity, pleasant taste and smell and beneficial effects on health. Thus, the capitalization of food products such as bread with Jerusalem artichoke flour, could be an opportunity to diversify the range of new products. The aim of this research was to elucidate the impact of added Jerusalem artichoke flour (in a concentration of 2.5%, 5%, 7.5% and 10%) in wheat flour bread on the sensory and physico-chemical properties of the finished product. Jerusalem artichoke flour has a high dry matter content and a high content of essential amino acids such as histidine, isoleucine, methionine, phenylalanine and valine. In the results we recommend the replacement of wheat flour with 5% Jerusalem artichoke flour, to obtain a product rich in micro and macronutrients with better organoleptic properties and a longer shelf life, which positively influences human health.

**Keywords:** *Jerusalem artichoke, dough fermentation, bread volume, organoleptic properties.*

## Introduction

Jerusalem artichoke (*Helianthus tuberosus*), also called "soil apple", "pork turnip", "guli", "potato of the poor" (from Hungarian), "Jerusalem artichoke" is a plant of the *Asteraceae* family, belonging, like the flower of the sun, the genus Helianthus. It is native to eastern North America, and the name Jerusalem artichoke comes from the Native American tribe "Topinambas" [1].

Jerusalem artichoke (*Helianthus tuberosus*) is a perennial plant which consists of a stem about 1–3 m tall, small yellow flowers, hairy oval shaped leaves and an underground rhizome system which bears small tubers. It is an Angiosperm plant species of the Composite family, which is commonly referred to as the sunflower or daisy family. The stems are stout and ridged which can become woody overtime. Its leaves alternate near the top of the stem, the lower leaves are larger and broader, and can grow up to 30 cm long while the higher ones are smaller and narrower. In terms of flower heads, each is 5–7.5 cm wide and formed by small, yellow, tubular disk flowers in the center and surrounded by

florets, which occur separately or in groups at the end of alar branches and main stems. As for tubers, they are uneven and elongate varying from knobby to round clusters. The colors of tubers range from pale brown to white, red and purple [2].

Over the years, within the Botanical Gardens of the Academy of Sciences of Moldova there was collected a collection of over 60 Jerusalem artichoke taxa with different periods of vegetation, plant habitus, shape and coloration of tubers, which serves as a material for improving the species, being selected perspective forms for the creation of new varieties. Among the perspective varieties in the collection are the Solar variety (harvest up to 44 t / ha) and Amicul II, created by clonal selection from large populations, registered in the catalog of plant varieties of the Republic of Moldova since 2014 [3].

It is known that due to its unique chemical composition, Jerusalem artichoke tubers can be used as a raw material for the industrial manufacture of flour, inulin, syrup and glucose-fructose powder, pectin, alcohol and various finished foods. The use of Jerusalem artichoke in food is quite diverse and includes juices, purees, syrups, fermented beverages, bakery products, etc. [4, 5]. Jerusalem artichoke juices can be natural or mixed with other fruit or vegetable juices, clarified or concentrated [6].

Jerusalem artichoke is a plant with a number of advantageous characteristics over traditionally agricultural crops, including high growth rate, good tolerance to frost, drought and poor soil, strong resistance to pests and plant diseases, with minimal to zero fertilizer requirements. Conventionally, Jerusalem artichoke has been used for food or animal feed, and for the past two decades, alternative uses have been explored especially for the production of functional food ingredients such as inulin, oligofructose and fructose. It is also found that some bioactive ingredients can be extracted from its leaves and stems, which creates an opportunity for applications in the pharmaceutical sector [7, 8].

In recent times, special attention has been paid to fermented beverages. It was demonstrated that inulin hydrolysis to reducing sugars from Jerusalem artichoke juice and its fermentation with homofermentative bacteria Pediococcus acidilactici DQ2 ensures high lactic acid productivity [9, 10, 11].

Several researches have been carried out in the Russian Federation in order to process Jerusalem artichoke in purees [12]. At the same time, several combinations of Jerusalem artichoke purees and pastas, fruits (apples, bananas, pears) and vegetables (carrots, pumpkins, eggplants) with pectin additives, nuts, bran were developed, intended for people suffering from diabetes [13, 14]. Jerusalem artichoke purees can be used as food or as additives in the manufacture of other foodstuffs [15, 16].

Another valuable product is Jerusalem artichoke flour which has a very low fat content, low caloric value and can be used for partial substitution (up to 10%) of wheat flour in the manufacture of bread and pastries but also as a functional agent in other foods [17, 18].

In order to protect the bioactive components (vitamins, phenolic compounds, etc.) from Jerusalem artichoke tubers, they can also be subjected to a convective drying process at 50 ° C. The flour is characterized by the content of inulin-type (51.60 ... 52.24%), fiber (6.85 ... 7.67%), total polyphenols (18.51 ... 44.03 mg GAE / g), protein (8.75 ... 9.01 %), iron (12.45 ... 12.78 mg / 100g), potassium (1905.44 ... 1912.85 mg / 100g), calcium (50.21 ... 51.12 mg / 100g) , magnesium (84.55 ... 86.85 mg / 100 g) and phosphorus content (300.12 ... 316.62 mg / 100 g). At the same time, the flour obtained from Jerusalem artichoke tubers has a high antioxidant potential [19].

The tubers of Jerusalem artichoke are rich in protein (3.2%, dry matter). Jerusalem artichoke proteins contain many amino acids (16), including 10 essential (they are not produced by the human body and come from food): arginine, valine, histidine, isoleucine, leucine, lysine, methionine, threonine, tryptophan, phenylalanine.

According to the Novosibirsk Scientific Research Institute of Clinical Immunology SB RAMS, these protein compounds are very close in structure to proteins of the thymus gland (thymus) – they have practically identical properties to those of thymus, major regulators of maturation and functional activity of cells of the immune system [20].

The Jerusalem artichoke is rich in pectin (approximately 11% of dry matter weight). Pectin's are high molecular weight carbohydrates that make up the cell membrane and intercellular substance. Pectin's have absorbent, astringent and thickening properties. They reduce the level of cholesterol in the body, improve metabolic processes, normalize bowel movements, and improve the peripheral circulation. But the most valuable feature of pectin is its ability to clear up the organisms without leaving any 'garbage' and not breaking of the balance of the internal body environment.

Currently, Jerusalem artichoke flour has been proposed for the manufacture of articles from leavened, sandy, tender, sponge dough and pasta [21, 22]. The administration of Jerusalem artichoke flour improves the porosity of bakery products and their sensory qualities. At the same time, the glycemic index of the finished products decreases, which is important for patients with diabetes and obesity [23, 24]. Noodle dough prepared with the addition of Jerusalem artichoke flour (compared to that of durum wheat flour) has a water-binding capacity and increased elasticity and low adhesiveness [25].

Bread has been considered one of the staple foods for centuries in many countries and is an important part of the diet. For example, the average volume of bakery and flour products consumed in the Republic of Moldova between 2012 and 2017 was 102.6 [26]. Based on the above, the purpose of the research in this article was to present the impact of the addition of Jerusalem artichoke flour obtained from the Solar and Amicu II variety on the quality of bread.

## 2. Materials and methods

Jerusalem artichoke flour used for research was obtained from tubers of the "Amicu II" and "Solar" variety, harvested at the Institute of Phytotechnics in Porumbeni, Chisinau.

The dry matter, ash content and titratable acidity of Jerusalem artichoke flour were determined using the methods described in ISO 6540: 2010 ISO 763: 2003 and ISO 750: 1998 [27, 28].

Flour quality indicators, wet gluten content, acidity were analyzed according to international standard methods.

### 2.1 Jerusalem artichoke flour obtaining

Before use, the tubers were packed and stored in the refrigerator at 4 ° C. Before drying, the tubers were washed and cut into rounds using an electric slicer. The thickness of the obtained washers is 1mm.The initial humidity of the tubers was 75.96% (3.15997kg water / kg dry matter, 315.97% / DM).

### 2.2. Atomic absorption spectroscopy (AAS)

Is a spectroanalytical procedure for the quantitative determination of chemical elements using the absorption of optical radiation by free atoms in the gaseous state.

Atomic absorption spectroscopy is based on absorption of light by free metallic ions For analysis, the samples were mixed with the required solvents. A series of working samples have been prepared from the solution. The atomic absorption spectrometer were adjusted for each of the studied elements. The sample were introduced into an atomizer, after which calibration solutions are added.

**2.3 Dry matter in Jerusalem artichoke flour samples**

For determination of dry matter content the flour samples were dried at a temperature between 130 ± 2 °C, until a constant mass of dry residue was obtained.

**2.4 Insoluble ash in hydrochloric acid**

The determination of the ash content was carried out by calcining the flour sample at a temperature of 550-600 ° C to a constant mass.

**2.5 Titratable acidity**

The acidity index is the amount of NaOH (1N NaOH / 100g of matter) required to neutralize one gram of product in the presence of phenolphthalein as an indicator.

**2.6 Amino acids in Jerusalem artichoke flour**

The amino acid content of Jerusalem artichoke flour was determined using the high performance liquid chromatographic (HPLC) method. In was used the gradient HPLC Agilent 1100 series. The HPLC instrument was equipped with an auto-injector, column compartment, fluorescent detector (G1315B), vacuum degasser and quaternary pump. Separation was performed on the Eclipse XDB C18 column (ID 2.1 × 150 mm, 5 µ particle size) at 40 ° C. Peak monitoring was performed on a fluorescent detector with excitation wavelength λex340 = nm and emission λem = 450nm.

**2.7 The impact of wheat flour substitution with Jerusalem artichoke flour on bread volume**

The specific volume of the breads (cm3 / g) is measured indirectly by moving small spherical solid particles with known specific volume in a container where the final bread is placed.

The measure consists in emptying the container up to half its solid particle content, over which the bread is placed and covered, the sample with the rest of the grains.

After leveling the surface of the measuring vessel, the volume of excess spherical grains corresponds to that of the bread. Thus, the specific volume of bread (Vsp) expressed in cm3 / g represents the ratio between the coefficient of bread volume (V) and its mass (M).

**2.8 Sensory analysis of bread samples**

The sensory evaluation of the obtained products was performed using a 30-point scale method [29]. Bread receiving between 24.1 and 30 points is considered to be of very good quality; between 18.1 and 24.0 points is of good quality; between 12.1 and 18.0 points is a satisfactory quality; between 6.1 and 12.0 is of poor quality; between 0.1 and 6.0 is a very poor quality.

The shape, surface of the crust, color, appearance in section, consistency of the crumb, taste and smell was evaluated by a tasters group. The criteria in Table 1 were used to quantify sensory characteristics.

### 2.9 Statistical analysis

All samples were analyzed in triplicate, and standard deviations are given in order to assess the repeatability of the methods used. Variance analysis of the results was carried out by least square method with application of Microsoft Office Excel program.

## 3. Results and discussions

### 3.1 Jerusalem artichoke flour characteristic

To obtain Jerusalem artichoke flour, the tubers were washed, dried and cut into 1 mm thick slices. The initial humidity of the tubers was 75.96% (3.15997 kg water / kg dry matter, 315.97% / DM).

The characterization of the flour is done using specific values: ash content, moisture, protein content, gluten content, baking power and others. All these features make it possible to understand the use of flour, whether it is intended for the manufacture of bread, biscuits or other products.

The two varieties of Jerusalem artichoke in the studio (Amicul II and Solar) have quite close physico-chemical indices. At the same time, from table 1 we notice that the flour obtained from the Jerusalem artichoke tubers of the Amicul II variety has a higher content of macro and microelements (table 1).

*Table 1*

**Physico-chemical indices of Jerusalem artichoke flour**

| Variety | Humidity% | Ash,% | Acidity degrees |
|---|---|---|---|
| Amicul II | 13,4 | 5,25 | 3,1 |
| Solar | 14,2 | 4,11 | 3,2 |
| | **Macroelements, mg / 100g** | | |
| | **Potassium** | **Calcium** | **Magnesium** |
| Amicul II | 18919±45 | 1014±12 | 294±3 |
| Solar | 10671±23 | 849±6 | 197±1 |
| | **Microelements, mg/100g** | | |
| | **Iron** | **Copper** | **Zinc** |
| Amicul II | 4,2±0,7 | 1,69±0,4 | 5,91±0,5 |
| Solar | 2,99±0,3 | 1,04±0,2 | 0,77±0,3 |

The protein content of Jerusalem artichoke flour and wheat flour was 2.4% and 11.9%, respectively. This content is higher than 7%, which corresponds to the minimum set by the Codex Alimentarius (FAO, 1996).

The content of amino acids in Jerusalem artichoke flour proteins of two varieties is shown in Figure 2, where we see that the dominant amino acids are glutamic acid and aspartic followed by the rest of the amino acids.

The protein content of wheat flour used in this study could compensate deficit of protein in the Jerusalem artichoke mass.

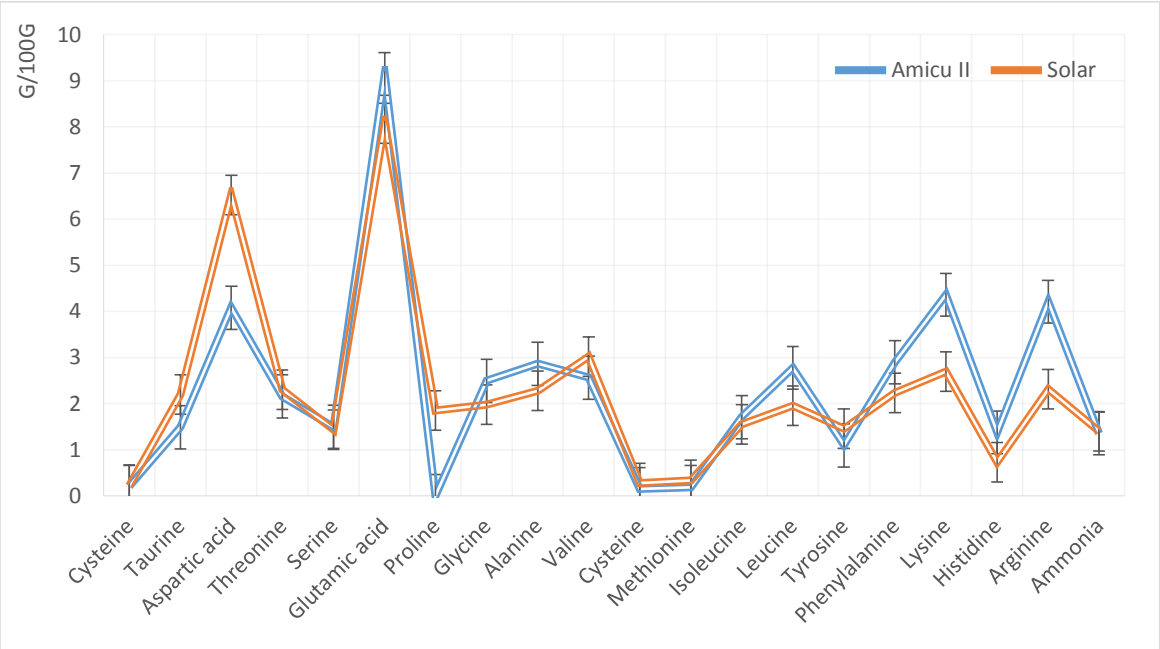


**Figure 2.** The content of amino acids in proteins of Jerusalem artichoke flour.

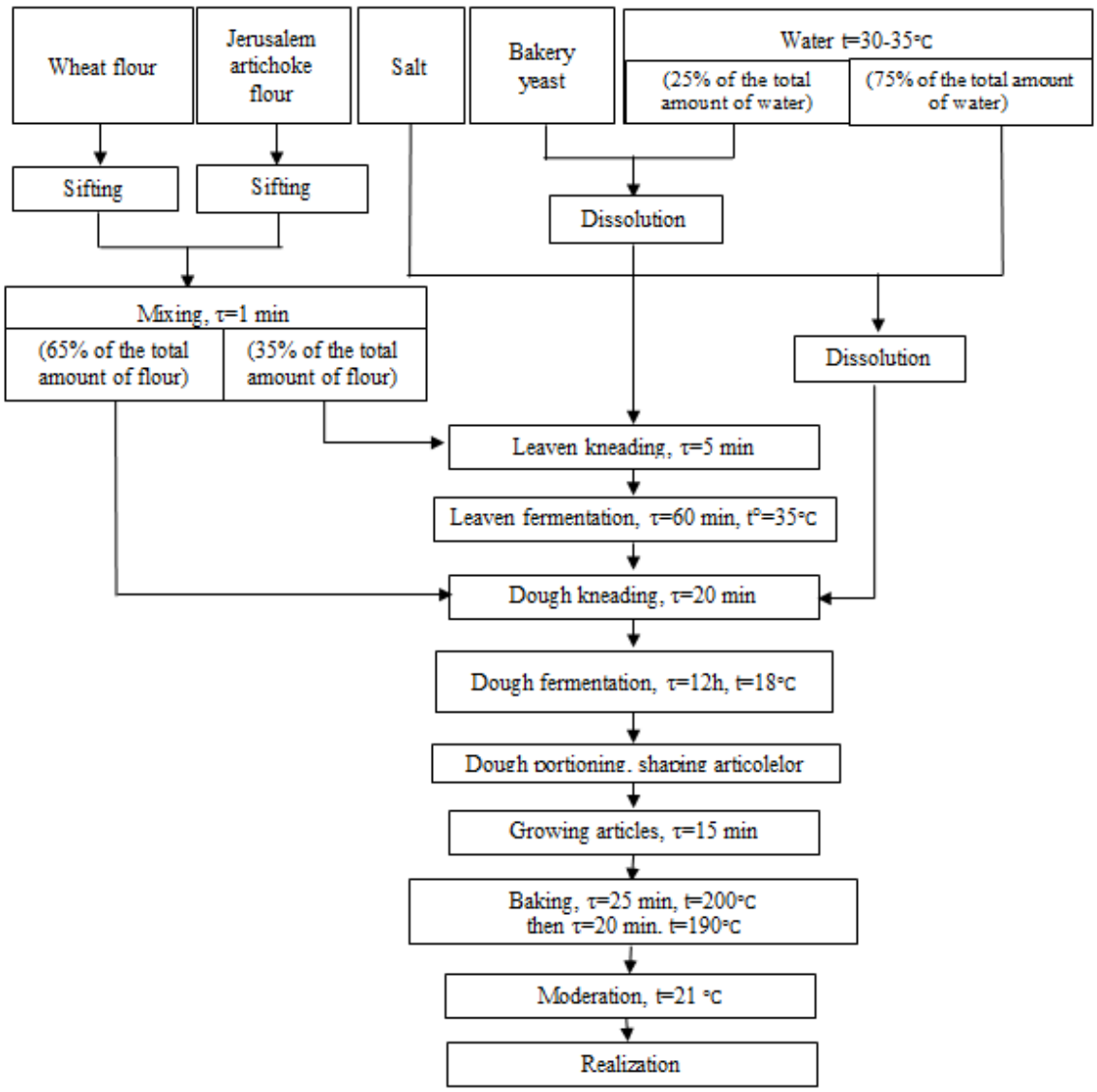


**Figure 3.** General scheme of bread making [developed by the authors].

### 3.2 Bread obtaining

The bread was obtained in the laboratory of culinary technology within the Department of Food and Nutrition, Faculty of Food Technology, Technical University of Moldova, by the indirect method according to the technological scheme presented in Figure 3.

#### 3.3. Titratable acidity during dough kneading and fermentation

During kneading and fermentation, the acidity of the dough increases. This increase is caused by acid reactions. The titratable acidity values of wheat flour and Jerusalem artichoke are shown in Table 2.

*Table 2*

**The evolution of titratable acidity during dough kneading and fermentation**

| Time, minutes | Wheat flour, control sample | Solar 2,5% | Solar 5% | Solar 7,5% | Solar 10% | Amicu II 2,5% | Amicu II 5% | Amicu II 7,5% | Amicu II 10% |
|---|---|---|---|---|---|---|---|---|---|
| **30** | 1,4 | 2,2 | 2,8 | 3,4 | 3,6 | 1,8 | 3,0 | 3,2 | 4,0 |
| **60** | 2,8 | 3,2 | 3,8 | 5,0 | 6,4 | 3,2 | 4,6 | 6,2 | 6,6 |

The increase in dough acidity is due to the formation and accumulation of lactic, acetic, succinic, malic, formic, tartaric, citric and other organic acids. The accumulation of lactic acid and acetic acid is considered to be the result of fermentation caused by lactic acid heterofermentative bacteria. Alcoholic fermentation, caused by yeast cells, leads to the formation of very small amounts of succinic acid in the dough.

#### 3.4 Evolution of the volume of the dough during fermentation

Fermentation is a specific stage of bakery products and has the role of enriching the dough with carbon dioxide. This process is complex and causes a loss of total matter (from 2 to 3%) by converting sugars into alcohol and carbonic acid [30]. Fermentation is generated by the action of yeasts on the sugars present in the dough which transforms them into alcohol and carbon dioxide, with energy production [31, 32].

Replacing wheat flour with Jerusalem artichoke flour slows the growth of the dough. The optimal fermentation period is 80 - 100 minutes with a gas expansion between 125% for the dough with a content of 10% Jerusalem artichoke flour and 154% - for the one containing 5% Jerusalem artichoke flour.

The share of added artichoke flour from Jerusalem in Amicul II and Solar juice in a concentration of 2.5%, 5%, 7.5% and 10% of the volume of dough growth during fermentation is shown in Figure 4a and 4b for each variety. respectively. The doughs obtained by adding artichoke flour from Jerusalem in different concentrations were tested to observe their stability by determining the optimal fermentation time. Tracking the progress of the volume of dough (wheat flour + artichoke flour) in fermentation (temperature 30 ° C) showed that the fermentation rate increased in the first 20-50 minutes, probably due to fermentable carbohydrates that are generally in small quantities in cereal flour (1.0 -1.5%) which are of particular importance in initiating the fermentation process (consumed in the first half hour of the fermentation process).

The dough mixes reached maximum volume values after 80 minutes of fermentation, and the volume of the dough remains relatively stable. During the fermentation process, the dough samples with the addition of Jerusalem artichoke flour in a concentration of 7.5% and 10% contributed to a slow increase in the volume of the dough.

The addition of Jerusalem artichoke flour generally has an effect beneficial on the volume of the dough, which contributed to a good fermentation and stability of the dough. Contribution optimal amount of Jerusalem artichoke flour was 2.5 (Solar variety) and 5% (Amicul II variety).

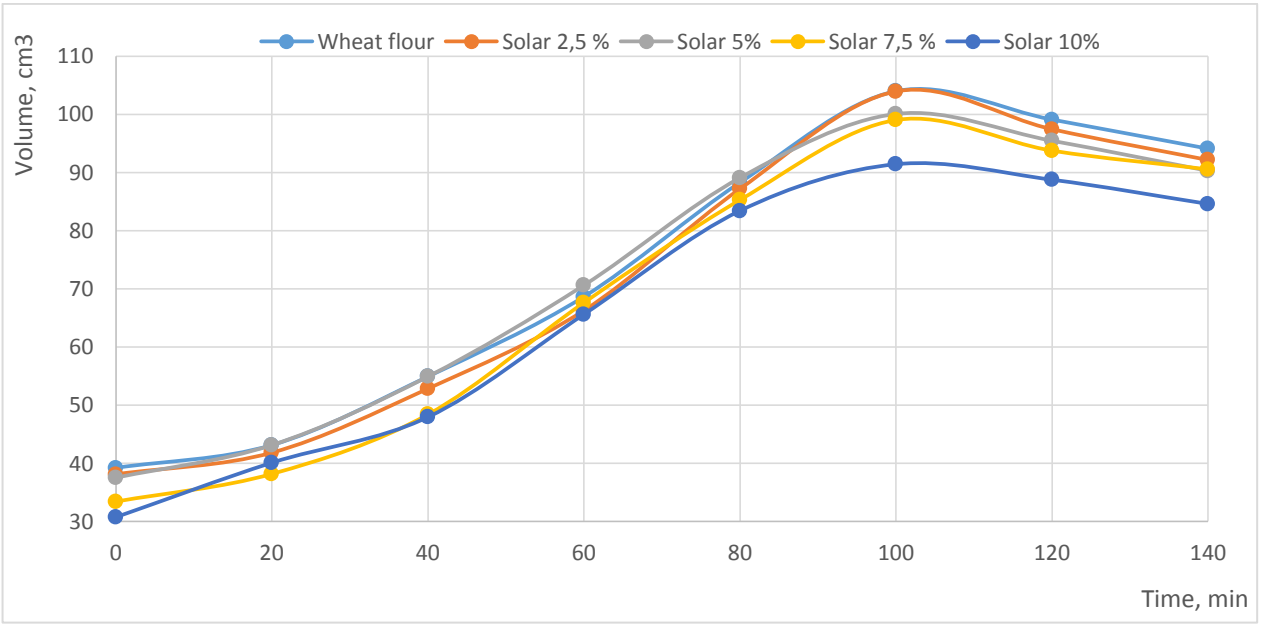


**Figure 4a.** The impact of the addition of Jerusalem artichoke flour on the volume of the dough during fermentation: dough from wheat flour (control sample,) dough from wheat flour-Jerusalem artichoke Solar variety in concentration of 2,5 %, 5%, 7,5% and 10%.

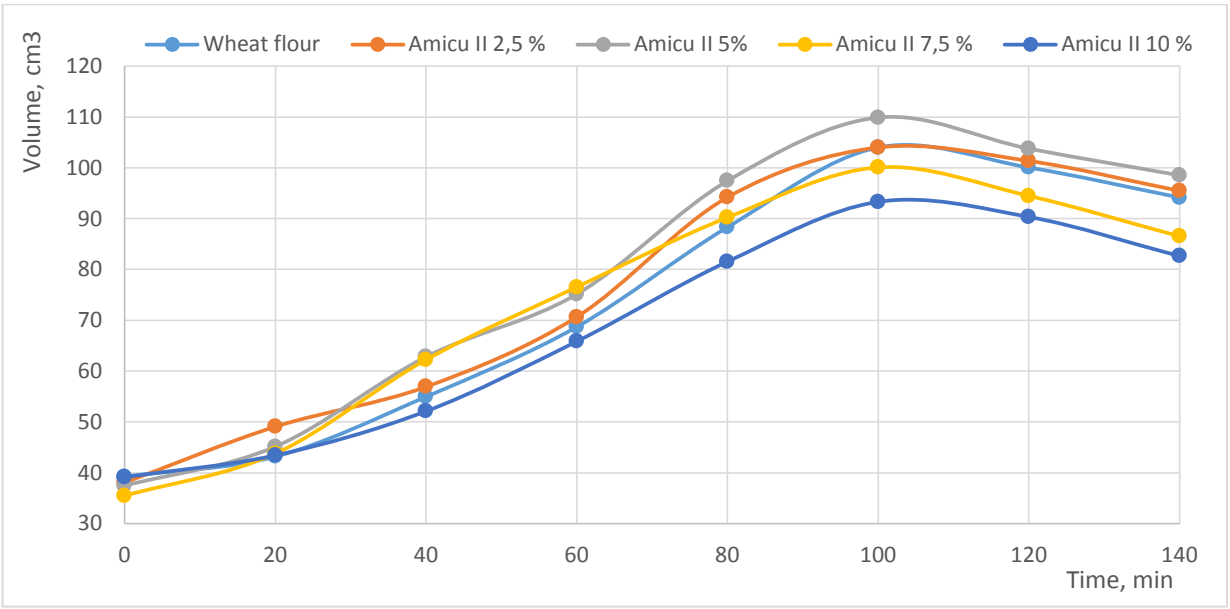


**Figure 4b.** The impact of the addition of Jerusalem artichoke flour on the volume of the dough during fermentation: dough from wheat flour (control sample,) dough from wheat flour-Jerusalem artichoke Amicu II variety in concentration of 2,5 %, 5%, 7,5% and 10%.

### 3.5 The impact of the addition of Jerusalem artichoke flour on the color of the crust

A good quality baking dough must have a certain resistance to mechanical work and be able to properly retain a maximum of gas during fermentation and baking, so as to have adequate rheological properties (hardness, extensibility, elasticity, strength). The rheological properties of the dough, with the addition of Jerusalem artichoke flour, depend on the quantity and quality of proteins present.

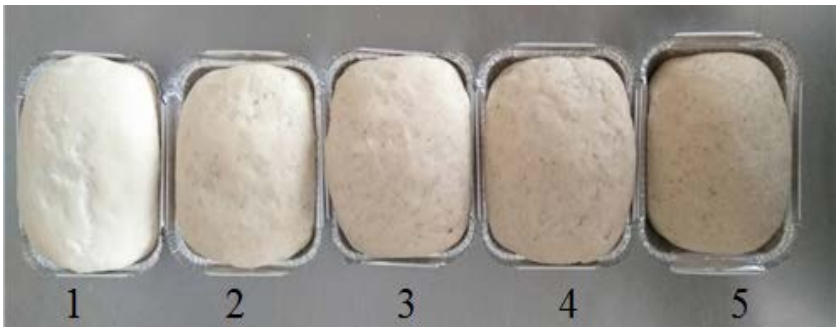


**Figure 5.** The impact of addition, in different concentrations, of Jerusalem artichoke flour on the quality of the bread (degree of replacement of wheat flour with that of Jerusalem artichoke, %): 1 – control sample, 0%; 2 – 2,5 % 3-5,0 % ; 4-7,5% ; 5-10,0%.

### 3.6 The impact of wheat flour substitution with Jerusalem artichoke flour on bread volume

Replacing wheat flour with Jerusalem artichoke flour up to 10% the color of the bread crust becomes darker. Several authors have attributed the coloring of the bread crust to Maillard reactions involving simple sugars and amino acids in the composition of Jerusalem artichoke.

The low content of simple sugars and the low fermentation power lead to the bread with the light color of the crust. While the bread with darker shades is due to the presence of excess of simple sugars obtained by changing the starch.


**Figure 6.** The impact of addition, in different concentrations, of Jerusalem artichoke flour on the color of the crust (degree of replacement of wheat flour with that of Jerusalem artichoke, %): 1 – control sample, 0%; 2 – 2,5 % 3-5,0 %; 4-7,5%; 5-10,0%.

The substitution of wheat flour with Jerusalem artichoke flour (up to 10%) also leads to a change in the color of the bread crumbs, from yellowish white to gray.

Also, the texture of the core becomes less aerated and the alveoli they grow irregularly, they are more compact, so we can say that increasing the concentration of Jerusalem artichoke flour will lead to poor bread quality.

### 3.7 Influence of Jerusalem artichoke flour addition on bread acidity compared to dough acidity

The acidity of bread is caused by the acidic substances in the flour with which the dough was prepared and by the acids that appear in the dough, as a result of the activity of yeasts and bacteria: carbon dioxide, lactic acid, succinic, malic and volatile acids - acetic and formic.

Under the action of the formed acids, the processes of hydration and peptization of amino acids intensify, the formation of the specific taste and aroma of the bread takes place.

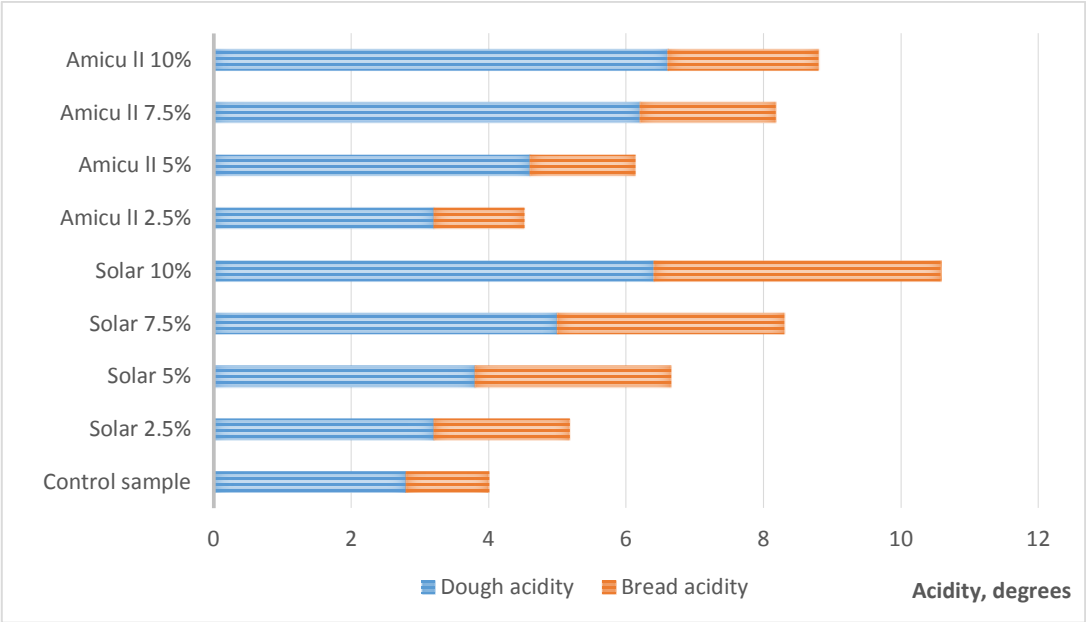


Figure 7. The influence of Jerusalem artichoke flour addition on the change in the acidity of bread compared to the acidity of the dough.

Due to the appearance of these acids there is an increase in the acidity of the dough during fermentation. About 60% of the acidity of the dough is due to lactic acid. The initial and final acidity of the dough is influenced by the degree of extraction of the flour, its consistency, the temperature and the duration of the leavening.

The final acidity of semi-finished products is an index of their maturity, being an important and controllable parameter, which directly influences their finite properties [21].

### 3.8 Sensory analysis

Organoleptic analysis of bread quality included assessment of the appearance of bread, symmetry of shape, volume, color and structure of the crust, color, elasticity and porosity of the core, taste, smell, signs of microbial spoilage and the presence of foreign bodies.

*Table 4*

**Appreciation of the external appearance of the bread**

| Sen sory feature | 0% | 2,5 % | 5 % | 7,5 % | 10 % |
|---|---|---|---|---|---|
| The shape and volume of the product | 4,0 | 4,0 | 4,0 | 4,5 | 3,0 |

*Continuation Table 4*

| | | | | | |
|---|---|---|---|---|---|
| The color and appearance of the crust | **4,0** | **4,0** | **4,0** | **3,5** | **2,0** |
| Degree of baking. the condition and appearance of the core | 6,0 | 6,0 | 6,0 | 5,0 | 4,0 |
| Core porosity and pore structure | 6,0 | 5,0 | 5,0 | 5,5 | 4,0 |
| Flavor | 4,0 | 3,0 | 4,0 | 3,5 | 2,0 |
| Taste | 5,0 | 5,0 | 6,0 | 5,5 | 3,0 |
| Total | 29,0 | 27,0 | 29,0 | 27,5 | 18,0 |

**Figure 8.** Organoleptic evaluation of bread quality with the addition of Jerusalem artichoke flour.

The results of the sensory evaluation showed very good qualities for the products made with the addition of Jerusalem artichoke flour of 5%. Samples of mixed flour bread with a Jerusalem artichoke flour content over 7.5 and even 10% had lower organoleptic indices, including lower shape and volume, cracked surface, pronounced flavor.

**Conclusions**

The use of Jerusalem artichoke flour in the manufacture of bread leads to improved chemical properties and quality of bread. These benefits were more significant at the 5% concentration of Jerusalem artichoke flour in bread. These changes are due to the high content of essential amino acids in Jerusalem artichoke tubers, such as histidine, isoleucine, methionine, phenylalanine and valine.

The organoleptic characteristics of the bread were improved by substituting wheat flour with Jerusalem artichoke flour up to 5%. Thus, the color of the bread crust becomes darker due to Maillard reactions involving simple sugars and amino acids in the composition of Jerusalem artichoke.

As the concentration of Jerusalem artichoke flour increases, the gluten concentration decreases, which leads to a decrease in the elasticity, porosity and texture of the dough.

The substitution of wheat flour with Jerusalem artichoke flour (10%) also leads to changes in the color and texture of the bread core, giving a poor quality of the bread.

As a result of this study, we recommend adding 5% Jerusalem artichoke flour to wheat bread to obtain a product rich in micro and macronutrients with better organoleptic properties and a longer shelf life, which positively influences human health.

The use of Jerusalem artichoke flour in bakery products represents an alternative direction in food development.

**Acknowledgements:** The research was funded by State Project 20.80009.5107.09 "*Improving of food quality and safety through biotechnology and food engineering",* running at Technical University of Moldova.

**References**

1. Marian G., Muntean A., Gudîma A., Tiţei V., Pavlenco A. Analiza comparativă a biomasei obţinute din culturi energetice. În: *Ştiinţa agricolă*, 2014, 2. pp. 70-74.
2. Fellin W. Analyzying Uncertainty in Engineering; Berlin. Germany: Springer, 2005, pp.251.
3. Titei V., Teleuta A. Specii perene şi soiuri de plante pentru fondarea plantatiilor energetice în Republica Moldova. In :*Întellectuss*, 2014, 4. pp.86-92.
4. Baltacioğlu C., Esin A. Chips Production from Jerusalem Artichoke (Helianthus tuberosus L.) In: *Food and Nutrition Sciences*, 2012, 3, pp.1321-1328.
5. Gedrovica I., Karklina D. Influence of Jerusalem Artichoke Powder on the Nutritional Value of Pastry Products. In: *World Academy of Science. Engineering and Technology International Journal of Biological. Biomolecular. Agricultural. Food and Biotechnological Engineering*, 2012, 6(7).
6. Nikitin P. V., Novikova I. L. A method for the production of un-clarified and clarified concentrated jerusalem artichoke juice: *Russian Federation Patent 2444914,* 2006.
7. Radovanovic A., Milovanovic O., Kipic M., Ninkovic M., Cupara S. Characterization of Bread Enriched with Jerusalem Artichoke Powder Content. In: *Journal of Food and Nutrition Research,* 2014, 2(12), pp.895-898.
8. Sumera Z., Narjis N., Saliha N., Mateen A. and Abdul M. K. Analysis of Selected Amino Acids in Different Varieties of Wheat Available in Punjab. Pakistan. In: *Hindawi Publishing Corporation Chromatography Research International,* 2014, pp.1-6.
9. Dao T.H., Zhang J., Bao J. Characterization of inulin hydrolyzing enzyme(s) in commercial glucoamylases and its application in lactic acid production from Jerusalem artichoke tubers (Jat). In: *Bioresour. Technol,* 2013, 148, pp.157–162.
10. Cheng X., Dong Y., Su P., Xiao X. Improvement of the fermentative activity of lactic acid bacteria starter culture by the addition of Mn. In: Appl Biochem Biotechnol, 2014, 174(5), pp.1752–1760.
11. Choi HY., Ryu HK., Park KM., Lee EG., Lee H., Kim SW. Choi ES. Direct lactic acid fermentation of Jerusalem artichoke tuber extract using Lactobacillus paracasei without acidic or enzymatic inulin hydrolysis. In: *Bioresour Technol*, 2012, 114, pp.745–747.
12. Safronova T. N. A new type of jerusalem artichoke processing product. In: *Journal of the Krasnoyarsk State Agrarian University*, 2010, 9, pp. 168-174.
13. Kupin G. A., Naimushina E. G., Zaiko G. M. Fruit and vegetable puree for diabetic patients: *Russian Federation Patent 2202231,* 2003.
14. Artyukh L. I., Shazzo R. I., Pavlova G. N., Erashova L. D., Alyokhina L. A., Ermolenko R. S. A method for the production of puree-like products based on jerusalem artichoke for dietary nutrition: *Russian Patent 2362324*, 2009.
15. Amirkhanov K. Zh. Complex use of meat and vegetable raw materials in the production of molded meat products. In: *Journal of the Altai State Agrarian Universit,* 2009, 11, pp. 76-80.
16. Ustinova A.V. Jerusalem artichoke and its processed products in functional meat products. In: *Meat industry*, 2012, 2, pp.19-21.
17. Takeuchi J., Nagashima T. Preparation of dried chips from Jerusalem artichoke (Helianthus tuberosus L.) tubers and analyşis of their functional properties. In: *Food Chemistry,* 2011, 126, pp.922-926.

18. Vinnitskaya V. F. Development of technology for processing jerusalem artichoke for the production of functional bread products. In: *Journal of the Michurinsk State Agrarian University*, 2013, 2, pp. 59-63.
19. Catană L., Catană M., Iorga E. Valorification of jerusalem artichoke tubers (Helianthus tuberosus) for achieving of functional ingredient with high nutritional value. In:*"Agriculture for life. Life for agriculture" conference proceeding*, 2018, 102478, PP.276-283.
20. Kuznetsova L. I. *Scientific basis of bread technologies using rye flour on sourdough with improved biotechnological properties:* Ph.D. Thesis. Moscow(Russia): State Research Institute of the Baking Industry of the Russian Agricultural Academy, St. Petersburg 2010.
21. Mezenova O. YA. Modeling the recipe of diabetic shortbread cookies with the addition of stevia and jerusalem artichoke. In: *Journal of the International Academy of Cold,* 2013, 4, pp. 23-26..
22. Tertychnaya T. N. Increasing the nutritional value of cupcakes through the use of promising plant additives. In: *Journal of the Voronezh State Agrarian University*, 2013, 1, pp. 291-297.
23. Dajdaleva M. I. Development of technologies and recipes for diabetic sugary confectionery products using products of processing of Jerusalem artichoke tubers. In: *Food technology*, 2011, 2-3, pp.66-68.
24. Kazakova O. N. Optimization of the recipe of shortbread cookies for diabetics with vegetable additives. In: *Food technolog,* 2012, 1, pp.53-56.
25. Umirzakova S. H. Jerusalem artichoke in the production of galette. In: *Journal of the Almaty Technological University*, 2012, 4. pp. 69-73.
26. Anuarul statistic al Republicii Moldova (Statistical Yearbook of the Republic of Moldova) (In Romanian). National Bureau of Statistics of the Republic of Moldova: Chisinau. Republic of Moldova, 2018, pp. 249.
27. ISO 763:2003 Fruit and vegetable products - Determination of ash insoluble in hydrochloric acid
28. ISO 6540:2010 MAIZE - Determination of moisture content (on milled grains and on whole grains)
29. Lawless H.T., Heymann H. Sensory Evaluation of Food. Principles and Practices; ed.*Springer*, Berlin. Germany, 2010, pp.596.
30. Chandrasekhar U. Determination of Moisture in Dehydrated Vegetables. In:*ISI Handbook of Food Analysis* (Part VIII); Indian Standards Institution: New Delhi. India. 1984, pp. 12.
31. Scafetta N. An Entropic Approach to the Analysis of Time Series. Ph.D. Thesis. University of North Texas. Denton. TX. (USA), 2001.
32. Siminiuc R., Țurcanu D. Impact of artisanal technologies on the quality indices of the sweet bread . In: *Food Systems*, 3(3), 2020.